UNIVERSITY OF SOUTHAMPTON

FACULTY OF ENGINEERING AND PHYSICAL SCIENCES

Aerodynamics and Flight Mechanics

Experimental investigation of secondary flows in turbulent boundary layers

by

Takfarinas Medjnoun

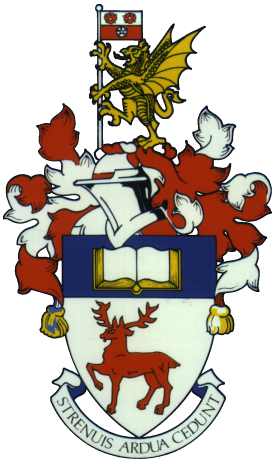

Thesis for the degree of Doctor of Philosophy

July 2020

ABSTRACT

Wall-bounded flows developing over spanwise heterogeneous surfaces exhibit time-averaged streamwise vortices when the spanwise characteristic length scale of the surface (S) is comparable to the dominant length scale of flow (δ) (Barros and Christensen, 2014). In this work, we experimentally examine a turbulent boundary layer developing over such surfaces, with particular attention to the large-scale secondary motions and their impact of the primary flow. We specifically examine three pivotal questions. (i) Can inner- and outer-layer similarity be possible in the presence of secondary flows? (ii) Are there other relevant length scales that carry the heterogeneity information? (iii) What are the effects of a heterogeneous to homogeneous step-change on the turbulent boundary layer secondary flows? A series of measurement campaigns were conducted over various surface conditions. The heterogeneity consists of smooth streamwise-aligned ridges of different spacings, shapes and widths and a step-change all with $S/\delta \approx \mathcal{O}(1)$. Oil-film interferometry, hot-wire anemometry along with stereoscopic-PIV are used to determine the flow properties. The skin-friction coefficients revealed that the drag of a heterogeneous surface can increase up to 35% compared to a smooth-wall. Lack of collapse in the outer region is shown for the mean, variance and also extends to the spectra across all scales in the near-wall region with a gradual collapse at small wavelengths for increasing S. Swirling strength maps revealed remarkable changes in the secondary motions for different ridge shapes. For wide ridges, tertiary structures can form appearing to compete with the secondary ones. An imbalance in favour of the former structures occurs over a certain width, causing a swap in the locations of the low- and high-momentum pathways. Furthermore, the results indicate that the spanwise spacing alone is insufficient to characterise the surface heterogeneity. A new parameter (ξ) based on the ratio of perimeters over and below the mean surface height is shown to adequately capture the variations in the flow properties. Finally when subjected to a step-change, the upstream secondary motions are shown to persist downstream. The velocity profiles in defect form and diagnostic plot showed that self-similarity is maintained hinting that the flow has built a pseudo-state of equilibrium in the presence of these secondary motions. These observations indicate that secondary flows posses a mechanism through which they are capable to self-sustain for long distances. Consequently, this means that both the growth rates of the internal layer as well as the turbulent boundary layer will depend on the evolution process of these large-scale features.

Contents

List of Figures

List of Tables

Declaration of Authorship

I, Takfarinas Medjnoun, declare that the thesis entitled *Experimental investigation of secondary flows in turbulent boundary layers* and the work presented in the thesis are both my own, and have been generated by me as the result of my own original research. I confirm that:

- this work was done wholly or mainly while in candidature for a research degree at this university;
- where any part of this thesis has previously been submitted for a degree or any other qualification at this university or any other institution, this has been clearly stated;
- where I have consulted the published work of others, this is always clearly attributed;
- where I have quoted from the work of others, the source is always given. With the exception of such quotations, this thesis is entirely my own work;
- I have acknowledged all main sources of help;
- where the thesis is based on work done by myself jointly with others, I have made clear exactly what was done by others and what I have contributed myself;
- parts of this work have been published as;

  Medjnoun, T., Vanderwel, C., and Ganapathisubramani, B. (2018). Characteristics of turbulent boundary layers over smooth surfaces with spanwise heterogeneities. *Journal of Fluid Mechanics*, 838, 516-543. doi:10.1017/jfm.2017.849

  Medjnoun, T., Vanderwel, C., and Ganapathisubramani, B. (2020). Effects of heterogeneous surface geometry on secondary flows in turbulent boundary layers. *Journal of Fluid Mechanics*, 886, A31. doi:10.1017/jfm.2019.1014

Signed:.....

Date:.....

Acknowledgements

First and foremost, I would like to express my acknowledgement to Prof. Bharathram Ganapathisubramani for offering such an opportunity to do this PhD under his supervision. Bharath's guidance throughout this journey has been paramount to the success of this project, and for also making me part of his outstanding group, I will always be thankful. I also extend my gratitude to my co-supervisor Dr. Christina Vanderwel, for the encouragement and enthusiasm she exercised, bringing additional scientific support to this work.

I also would like to express my gratitude to both Prof. Vladimir Nikora and Dr. Roeland de Kat for examining this modest contribution. I am very grateful for all the suggestions and recommendations they provided.

I am also very thankful to all the people that I had the chance to work with and learn from throughout these years. I would like to especially mention Dr. Davide Lasagna, Dr. Ivo Peters and Dr. Jason R. Heart for being role models, inspiring the next generation of researchers. Also, thanks to all my former and current colleagues from Bgroup.

I am very grateful to the different sponsors that contributed through their funding to the completion of this project: European Research Council (ERC grant agreement no. 277472), the Engineering and Physical Sciences Research Council of the United Kingdom (EPSRC grant ref. no. EP/L006383/1 and EP/P021476/1). Also, the Faculty of Engineering and Physical Sciences at the University of Southampton. I am also thankful to every person who directly or indirectly had an input into this work, such as the technicians (especially Chris Malcolm), ISolutions and the admin staff of the UoS. They continuously provide great support and offer the best conditions and commodities for success, making it a world-class place for scientific research.

To both, my family and family in-law, I would like to say thank you very much for your amazing help and continuous support throughout this period of life, which have been of great comfort to overcome challenges. Finally, to the person who always provided me with unconditional support, stood by my side since the day we met and without whom this work could have not been accomplished. Words cannot express how deeply grateful I am, to have her love and affection, my wife, whom I love the most. Thank you Fatma Berdous!

In loving memory of my late grandmother, Chavha Merfed ...

"Then you will know the truth, and the truth will set you free."

– John 8:32

Nomenclature

Roman Symbols

Δf	Fringe spacing of the inteferogram
ΔP	Pressure difference from the Pitot-static tube
ΔU^+	Roughness function
$\mathcal{H}$	Heterogeneity parameter
$\mathcal{P}$	Propability density function
$\tilde{k}$	Turbulent kinetic energy deficit
$\tilde{u}, \tilde{v}, \tilde{w}$	Streamwise, wall-normal and spanwise dispersive velocity fluctuation
A, B	King's law coefficients
a_w	Over heat ratio
B	Smooth wall intercept
C_f	Skin-friction coefficient
d	Zero-plane displacement
E	Voltage from the HWA
F_a	Acquisition frequency
F_c	Cut-off frequency
H	Shape factor
h	Roughness height/Oil-film height
h_s	Equivalent sand grain roughness height
I	Intensity of the light wave
K	Acceleration parameter

k	Wavenumber of velocity fluctuations
L	Streamwise reference lengthscale
l	PIV spatial filter/TNTI arc-length/Coherent structure lengthscale
N	Number of samples
n	Refractive index, power of King's law
P	Mean static pressure
R_a	Resistance measured at ambiant temperature
R_w	Resistance measured at the wire temperature
Re	Reynolds number
S	Spanwise characteristic lengthscale
T	Temperature/Duration of measurement/Tortuosity
t	time variable
U, V, W	Mean streamwise, wall-normal and spanwise velocity
u, v, w	Streamwise, wall-normal and spanwise turbulent velocity fluctuation
U_τ	Friction velocity
W	Width of the roughness element
w	Cole's wake function
x, y, z	Streamwise, wall normal and spanwise directions
y_0	Roughness lengthscale
Y_i	Mean intermittency height

Greek Symbols

β	Rough-to-smooth skin friction ratio
δ	Boundary layer thickness
δ^*	Displacement thickness
ϵ_x	Uncertainty of the quantity x
Γ	Peak-to-valley skin friction ratio/Streamwise circulation
γ	TNTI Intermittency

κ	Von-Karman coefficient
λ	Light wavelength/Wavelength of velocity fluctuations
λ_{ci}	Swirling strength
μ	Air/oil fluid dynamics viscosity
ν	Air/oil fluid kinematics viscosity
Φ	Phase difference between two interfering light waves/Energy spectral density
ϕ	Light wave/Coherent structure inclination angle
Π	Cole's wake parameter
Ψ	Modified log-law
ρ	Air/oil fluid density
σ_x	Standard deviation of the quantity x
τ	Eddy turn-over time/Stress tensor
τ_w	Wall shear stress
θ	Momentum thickness/OFI camera angle
Ξ	Indicator function
ξ	Voltage linearisation factor/Spanwise roughness parameter

Superscripts

$\cdot^+$	Inner-normalisation using U_τ and ν

Subscripts

$\cdot_\infty$	Freestream condition
$\cdot_a$	Atmospheric condition/Air
$\cdot_o$	Oil
$\cdot_{ref}$	Reference
$\cdot_{th}$	Threshold
$\cdot_x$	Streamwise component

Abbreviations

HMP	High-momentum pathway

HWA Hot-wire anemometry

LMP Low-momentum pathway

OFI Oil-film interferometry

PIV Particle image velocimetry

TBL Turbulent boundary layer

TKE Turbulent kinetic energy

TNTI Turbulent non-turbulent interface

VLSM Very-large-scale-motions

1. Introduction

1.1 Motivation

Fluid mechanics has garnered interest for many centuries as shown from the early principles of Archimedes to the fundamental works of Bernoulli, passing by artists as well as scientists, such as Leonardo da Vinci and Hokusai who highlighted through their paintings the presence of vortical patterns in river flows. A major breakthrough in fluid mechanics came from Osborne Reynolds, who provided a universal scaling parameter that allows the prediction of the condition at which flows transition from laminar to turbulence (Reynolds, 1895). Equations of viscous flows have since been established for almost two centuries by Navier (1823) and Stokes (1845), which were later on labelled the Navier-Stokes equations. In 1904, Prandtl delivered a ground-breaking paper where he describes the concept of a boundary layer and its importance for drag, setting the basis of a new research framework for turbulent flows in general and boundary layers in particular (Prandtl, 1904). Since then, outstanding advancements in its flow physics have been made, thanks to the computational and experimental resources, but also due to the environmental requirements, leading the applications of fluid mechanics to a wider range.

One of the turbulent boundary layer ranges are flows that develop over rough walls. This type of flows is of great importance because of its multi-scale presence in the natural and industrial environments. Such examples date back to the early work of Hagen (1854) and Darcy (1857) in pipes. These were followed by the work of Nikuradse (1933) and Colebrook et al. (1939), which allowed the first drag prediction tool, widely popular among the engineering community developed by Moody (1944) and known as the Moody-diagram. Rough-wall flows can also be encountered in engineering applications such as marine transportation (Schultz, 2007; Monty et al., 2016), turbomachinary and heat exchangers (Bons et al., 2001, 2008; Bons, 2010; Bai et al., 2014; Chow and Maheikey, 1992). Their presence is ubiquitous in natural landscapes such as in atmospheric boundary layers and urban flows (Thom, 1971; Theurer et al., 1992; Garratt, 1994), as well as in hydrology (Nikora and Goring, 2000; Nikora et al., 2004). In the recent years, the effects of roughness have also been explored in biological aerodynamics such

as in bird flights and fish swimming (Dean and Bhushan, 2010; Lentink and de Kat, 2014; Van Bokhorst et al., 2015), where in all the above-mentioned examples roughness plays a fundamental role influencing the overall drag, turbulent mixing and transport properties.

A more specific class of rough walls flows is heterogeneous roughness (more specifically the spanwise heterogeneity), which started earning more attention in the last decade due to its occurrence in various environmental and engineering processes. Their examples span flows in rivers, wind farms, bio-fouled turbine blades, herringbone riblets, super-hydrophobic surfaces among others (Nezu et al. 1993; Nugroho et al. 2013; Barros and Christensen 2014; Benschop and Breugem 2017; Vanderwel et al. 2017). These surfaces are shown to feature a common length scale represented by their spanwise characteristic wavelength. If the latter is comparable to dominant length scale of the flow, large-scale secondary motions occur (Vanderwel and Ganapathisubramani 2015; Yang and Anderson 2017; Chung et al. 2018; Chan et al. 2018).

Following the previous studies mentioned above, these spanwise heterogeneous surfaces can be classified into two categories. Topographically-driven heterogeneity such as alternating elevated and recessed regions, and wall-drag-driven heterogeneity such as alternating high- and low-shear stress regions. Irrespective of which type of heterogeneity, similar features can be observed over all heterogeneous surfaces. The secondary motions entail a highly three-dimensional flow, with high- and low-momentum pathways (HMPs and LMPs) alternating in the spanwise direction (Mejia-Alvarez and Christensen, 2013). The upwash regions (LMPs) are accompanied by a strong Reynolds shear stress and turbulent activity which are inhomogeneous in the cross-plane. Regardless of the boundary condition, these secondary flows are shown to be a consequence of an imbalance between turbulence production and dissipation, itself driven and sustained through turbulence-anisotropy (Hinze 1973; Anderson et al. 2015; Hwang and Lee 2018). In spite of their large effect on the primary flow, the secondary motions are shown to be relatively weak in comparison to the latter. In fact, the secondary flows were explained to be simply the result of superimposition of stronger instantaneous vortices, which occur only in a small fraction of the total time, and are unevenly distributed in the cross-plane (Kevin et al. 2017; Vanderwel et al. 2019).

Despite the commonalities between these numerous heterogeneous surfaces, several aspects still remain ambiguous. In the case of wall-drag heterogeneity, the upwash and downwash motions systematically occurred above the low and high drag respectively (Hinze 1973; McLelland et al. 1999; Wang and Cheng 2005; Willingham et al. 2014; Türk et al. 2014; Stroh et al. 2016; Chung et al. 2018). For the topographical heterogeneities, several studies reported the upwash and downwash motions occurrence above elevated and recessed regions respectively (Nezu and Nakagawa 1984; Wang and Cheng 2006; Vanderwel and Ganapathisubramani 2015; Medjnoun et al. 2018; Hwang and Lee 2018). In contrast, the opposite behaviour was shown in other experimental and numerical

investigations (Mejia-Alvarez and Christensen 2013; Barros and Christensen 2014; Yang and Anderson 2017; Awasthi and Anderson 2018).

The validity of outer-layer similarity hypothesis (Townsend, 1976) has also been discussed. Earlier to the study of Barros and Christensen (2014) which highlighted secondary motions in a highly irregular surface roughness, Wu and Christensen (2007, 2010) reported statistical as well as structural similarity in the outer layer. They further investigated the inner-outer interactions over the same surface, and reported the amplitude and frequency modulations to be similar to that of a smooth wall at both the downwash and upwash regions, reinforcing the argument of existence of similarity. Other studies on the other hand reported the absence of outer-layer similarity in the mean flow as well as in the turbulence and spectra, owing to roughness effects which extended farther into the outer layer (Yang and Anderson 2017; Awasthi and Anderson 2018; Chan et al. 2018; Chung et al. 2018).

Furthermore, in order to identify the surface properties that characterise best the heterogeneity, many researchers performed parametric studies. Despite the fact that the spanwise spacing is shown to be the relevant scaling parameter of the heterogeneity (Vanderwel and Ganapathisubramani 2015; Yang and Anderson 2017; Anderson et al. 2018; Chung et al. 2018; Chan et al. 2018), other studies showed that other surface features exhibited a potential to influence the secondary flows, such as the high roughness width (Willingham et al. 2014; Türk et al. 2014; Stroh et al. 2016), or the ridge shape and width (Goldstein and Tuan 1998; Wang and Cheng 2006; Hwang and Lee 2018).

Additionally, the development of these secondary flows past a heterogeneous to homogeneous step-change remains to date unexplored. In fact, to the author's knowledge, all of the existing literature on step-changes exclusively consider flows growing over homogeneous surfaces undergoing either rough-to-smooth or smooth-to-rough changes (Antonia, 1972; Garratt, 1990; Hanson and Ganapathisubramani, 2016). These studies have shown that when a turbulent boundary layer experiences roughness discontinuities, a new internal layer begins growing further downstream. While above the new layer, the mean and turbulent flow remain characteristic of the upstream boundary condition, an equilibrium layer grows which adjusts to the new surface condition.

Further to these motivations, this study intends to document the characteristics of turbulent boundary layers in the presence of surface heterogeneity and secondary flows. This would ultimately result in a broader picture towards the general understanding of three-dimensional turbulent boundary layers and aid those who seek developing predictive tools that account for such features, be it for flow control strategies or simply practical applications such as in atmospheric boundary layers fluvial processes.

1.2 Objectives and approach

The overarching aim of this work is to document the characteristics of these three-dimensional flows and identify an additional surface parameter relevant for the scaling of the secondary flows. This study explores the applicability of the classical scaling laws. It also examines the link between the surface heterogeneity and various other flow quantities, such as drag, momentum transport due to turbulent and dispersive stresses, structural similarity as well as the outer-layer intermittency. The main questions that this study tries to address are:

- Can inner- and outer-layer similarity hypotheses still hold in the presence of secondary flows?
- Are there other relevant length scales that carry the heterogeneity information, and how to predict the location of the upwash and downwash motions for the topographical heterogeneous surfaces?
- And finally, to what extent can the secondary flow persist past a heterogeneous-to-homogeneous step-change?

We are going to address these three questions experimentally and independently (each with its own measurement campaign), where we investigate the flow over smooth ridge-type heterogeneous surfaces. We specifically assess the effect of spanwise spacing, shape and width of the ridges, while a single case of a step-change will be discussed. Oil-film interferometry (OFI) in conjunction with hot-wire anemometry (HWA) as well as stereoscopic particle image velocimetry (SPIV) will provide the relevant quantities to enable us assess the impact of these surfaces on the turbulent boundary layer flow.

1.3 Outline and contributions

Chapter 1 introduces the main motivations and objectives to undertake the current work highlighting the main addressed questions. Chapter 2 provides the fundamental concepts for both smooth- and rough-wall bounded turbulence, with a survey of the literature on the current state of the art and research on secondary flows in wall-turbulence. Chapter 3 presents a detailed description of the experimental setup and the instrumentations used throughout the study. Chapter 4 discusses the results from the first measurement campaign with an emphasis of the examination of the local outer-layer similarity. Parts of these results are published in the paper *Characteristics of turbulent boundary layers over smooth surfaces with spanwise heterogeneities* of the *Journal of Fluid Mechanics* (Medjnoun et al., 2018). Chapter 5 analyses the results from the

second measurement campaign which investigates the effects of heterogeneous surface geometry on secondary flows in turbulent boundary layers. This work has been published in the paper *Effects of heterogeneous surface geometry on secondary flows in turbulent boundary layers* of the *Journal of Fluid Mechanics* (Medjnoun et al., 2020). Chapter 6 presents the results from the third measurement campaign and explores the effects of the heterogeneous to homogeneous step-change on the secondary flows. This work is currently being further analysed and will similarly be submitted for publication. The last chapter 7 discusses the main findings providing our conclusions on this work with some comments and recommendations for future work.

This work contributed its results in the following as:

Journal articles

Paper 1

Medjnoun, T., Vanderwel, C. and Ganapathisubramani, B. (2018). Characteristics of turbulent boundary layers over smooth surfaces with spanwise heterogeneities. *J. Fluid Mech.*, **838**:516–543. doi:10.1017/jfm.2017.849.

Paper 2

Medjnoun, T., Vanderwel, C. and Ganapathisubramani, B. (2020). Effects of heterogeneous surface geometry on secondary flows in turbulent boundary layers. *J. Fluid Mech.*, **886**:A31. doi:10.1017/jfm.2019.1014.

Paper 3

Medjnoun, T. and Ganapathisubramani, B. (2020). Development of turbulent boundary layer secondary flows past a heterogeneous to homogeneous step-change. *J. Fluid Mech.*, *(In preparation)*.

Conferences

ETC 2017

Medjnoun, T., Vanderwel, C. and Ganapathisubramani, B. (2017). Effect of roughness type on the secondary flows in turbulent boundary layers over heterogeneous surfaces. 16^{th} *European Turbulent Conference*, **Stockholm, Sweden**.

APS DFD 2017

Medjnoun, T., Vanderwel, C. and Ganapathisubramani, B. (2017). Characteristics of turbulent boundary layers over smooth surfaces with spanwise heterogeneities. 70^{th} *Annual Meeting of the APS Division of Fluid Dynamics*, **Denver, USA**.

APS DFD 2018

Medjnoun, T., Vanderwel, C. and Ganapathisubramani, B. (2018). Influence of surface geometry on secondary flows in turbulent boundary layers. 71^{th} *Annual Meeting of the APS Division of Fluid Dynamics*, **Atlanta, USA**.

TSFP 2019

Medjnoun, T., Vanderwel, C. and Ganapathisubramani, B. (2018). Turbulent flow past a step-change in wall topography: Evolution of secondary flows. 11^{th} *International Symposium on Turbulence and Shear Flow Phenomena*, **Southampton, UK**.

2. Background

2.1 Smooth-wall turbulent boundary layers

Numerous works have reviewed the boundary layer theory and its wide range of application in many problems; Tennekes and Lumley (1972) and Pope (2000) remain among the most classical references. As mentioned in the previous section 1.1, the concept of a boundary layer was first introduced by Prandtl (1904) which states that the flow can globally be divided into two regions. A region where the flow very far from the wall is irrotational with the free stream velocity unvarying in the wall-normal direction. Additionally, a region where the axial velocity gradually decreases down to the wall, in order to satisfy the no-slip condition imposed by the latter. This velocity variation happens within a thin layer called a *boundary layer*, where the effects of viscosity are not negligible in comparison with inertial forces, leading to the production of vorticity and turbulence. Outside this boundary layer, the flow is vorticity free.

Smooth-wall turbulence is present in a variety of applications. In both research and engineering problems, smooth walls represent a very good simplification in order to come up with theories and to extract elementary models that could provide physical insights. In engineering; automotive, aircraft and aerospace industry, almost all of their models assume smooth walls, and it is still a fairly good approximation for predicting the flow around these objects. In a frame of reference described by the Cartesian coordinates system x, y and z where respectively describing the streamwise, wall-normal and spanwise directions, and their corresponding time-averaged velocities U, V and W, the weakly growing boundary layer hypothesis assumes:

- Plane flow ($W = 0$, $\frac{\partial \langle \rangle}{\partial z} = 0$),
- Incompressible and stationary (ρ is constant, $\frac{\partial \langle \rangle}{\partial t} = 0$),
- Thin shear layer ($\delta(x) \ll L(x)$, with $\delta(x)$ and $L(x)$ being the wall-normal and streamwise reference length scales respectively),

Based on these hypotheses, the streamwise momentum equation reduces to

$$U\frac{\partial U}{\partial x}+V\frac{\partial U}{\partial y}=\nu\frac{\partial^2 U}{\partial y^2}-\frac{\partial\overline{(uv)}}{\partial y}-\frac{1}{\rho}\frac{dP_\infty}{dx}=\frac{1}{\rho}\frac{\partial\tau}{\partial y}+U_\infty\frac{dU_\infty}{dx}, \tag{2.1}$$

where $U_\infty\frac{dU_\infty}{dx}$ is the streamwise convective term due coming from the pressure gradient $\frac{\partial P_\infty}{\partial x}$ while $\tau(x,y)$ is the *total shear stress* defined by

$$\tau=\rho\nu\frac{\partial U}{\partial y}-\rho\overline{(uv)}. \tag{2.2}$$

On the other hand, the total shear stress applied at the wall due the no-slip condition reduces to the mean velocity gradient at the wall:

$$\tau_w=\rho\nu\frac{\partial U}{\partial y}. \tag{2.3}$$

The *skin-friction velocity* can then be defined as

$$U_\tau=\sqrt{\tau_w/\rho}, \tag{2.4}$$

and the skin-friction coefficient is expressed by

$$C_f=\frac{\tau_w}{\frac{1}{2}\rho U_\infty^2}. \tag{2.5}$$

The largest length scale of the flow in defined as $\delta(x)$, yet it has no unique definition. The most common definition is the distance from the wall at which the velocity reaches 99% of the free stream velocity U_∞. Another estimate of δ is commonly used for flows developing over rough surfaces, proposed by Perry and Li (1990) and is expressed by

$$\delta=\frac{\delta^* U_\infty}{C_1 U_\tau}, \tag{2.6}$$

with C_1 given by the integral of the mean velocity deficit as

$$C_1=\int_0^1 g d\eta, \tag{2.7}$$

where $g(\eta)$ is given by

$$g(\eta)=\frac{U_\infty-U}{U_\tau}, \tag{2.8}$$

with $\eta=y/\delta$, and $\delta^*(x)$ representing the displacement thickness expressed as,

$$\delta^*(x)=\int_0^\infty\left(1-\frac{U}{U_\infty}\right)dy. \tag{2.9}$$

An additional integral-based quantity also used is the momentum thickness defined as

$$\theta(x) = \int_0^\infty \frac{U}{U_\infty}\left(1 - \frac{U}{U_\infty}\right) dy. \tag{2.10}$$

Following the definition of Schlichting (1979), δ^* relates to the *mass flux deficit* and represents the equivalent distance by which a surface would have to be raised to the reference plane in an inviscid flow of velocity U_∞ to give the same flow rate as occurs between the surface and the reference plane in a real fluid. Similarly, the momentum thickness θ is associated with the *momentum flux deficit* and represents the equivalent distance by which a surface would have to be elevated towards the reference plane in an inviscid fluid of velocity U_∞ to give the same total momentum as exists between the surface and the reference plane in a real fluid.

Following Prandtl's idea, the flow is divided into two regions, where the flow behaves as laminar and the inviscid flow equations can be used to predict the flow (far enough from the wall), and the boundary layer itself which can be broken into two main parts. The inner layer and the outer layer, each with its own characteristics and scaling laws, where U is scaled with the friction velocity U_τ, and y is scaled with both the kinematic viscosity ν and U_τ. Application of non-dimensional analysis to the streamwise momentum equations leads to Prandtl′s law of the wall (Prandtl, 1925)

$$\frac{U}{U_\tau} = f\left(\frac{yU_\tau}{\nu}\right), \tag{2.11}$$

where f is a universal function that scales the very near-wall region independently of the large-scale characteristics of the flow. Whereas beyond a certain distance from the wall, the scaling is no longer applicable, and the mean streamwise velocity scales with the largest scales instead, which is defined by the velocity defect law, expressed by

$$\frac{U_\infty - U}{U_\tau} = g\left(\frac{y}{\delta}\right). \tag{2.12}$$

Following these universal scaling functions on the velocity distribution, Millikan (1938) derived a logarithmic law for the mean velocity in the overlap region of the scaling laws for the inner and outer layers in the limits of $\frac{yU_\tau}{\nu} \to \infty$ and $\frac{y}{\delta} \to 0$ as

$$\frac{U}{U_\tau} = \frac{1}{\kappa}\ln\left(\frac{yU_\tau}{\nu}\right) + B. \tag{2.13}$$

Earlier to Millikan (1938), Von Kármán (1930) investigated experimentally a turbulent pipe flow and examined the mean velocity distribution along the pipe radius. He reported the existence of a region where the velocity profiles scale logarithmically. Von Kármán (1930) provided the first fitting constants of the so-called log-law, κ and B denoting the slope and the intercept respectively. However, these "constants" have been examined

at high Reynolds number canonical smooth-wall flows and were shown to vary, with κ being 0.37, 0.39 and 0.41 for channels, boundary layers and pipe flows respectively (Nagib and Chauhan 2008; Marusic et al. 2010, 2013). Moreover, their universality has recently raised interrogations in the community to whether there might be effects of the surface condition such as the type of roughness (Amir and Castro, 2011).

Furthermore, Coles (1956) extended the log-law to cover both the overlap and outer region of the boundary layer by introducing a wake function, w, and modifying the equation to

$$\frac{U}{U_\tau} = \frac{1}{\kappa}\ln\left(\frac{yU_\tau}{\nu}\right) + B + \frac{\Pi}{\kappa}w\left(\frac{y}{\delta}\right). \tag{2.14}$$

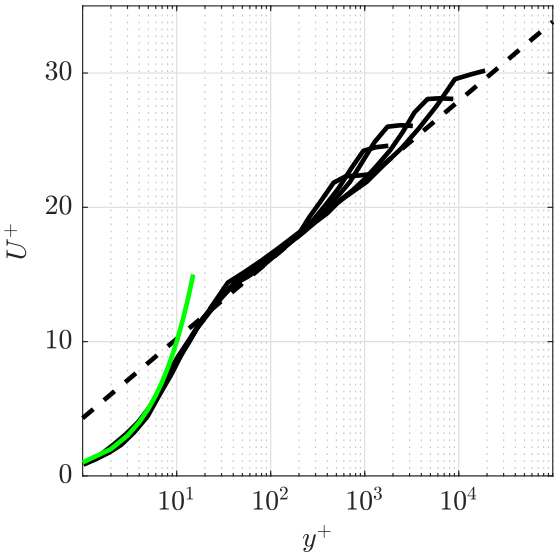

Figure 2.1: Inner-normalised velocity profiles at increasing Reynolds number over a flat plate turbulent boundary layer highlighting a universal scaling region. The green line denotes the $U^+ = y^+$ solution valid below $y^+ = 6$. The black dashed line denotes the logarithmic fit $\frac{1}{\kappa}\ln(y^+) + B$ with κ and B being 0.39 and 4.3. The data is adapted from DeGraaff and Eaton (2000).

.

Figure 2.1 illustrates the inner-scaled mean streamwise velocity profiles at different momentum thickness-based Reynolds numbers Re_θ ranging between 1430–31000 of a turbulent boundary layer over a flat plate. The figure shows a good degree of collapse of the profiles for $y^+ < 6$ in the form of $U^+ = y^+$ (with the superscript $^+$ referring to the velocity being scaled with U_τ and the wall-normal distance with ν/U_τ), which is known as the viscous sublayer. Between $6 < y^+ < 50$, a buffer layer is shown to prevail and also collapses all the profiles into a single curve. Beyond $y^+ > 50$, a logarithmic scaling is shown to occur for the velocity distribution with an increasing upper bound when increasing Reynolds numbers. Beyond this upper limit, an overshoot of the velocity from the logarithmic behaviour is observed, which is indicative of the wake region of the flow. This region is characterised by the wake strength parameter Π and is believed to

stem from a dual effect of the velocity jumps in the uniform momentum zones and the jump across the turbulent/non-turbulent interface (Krug et al., 2017).

2.2 Rough-wall turbulent boundary layers

Similarly to smooth-wall turbulence, rough-wall bounded flows are also of a major importance since they come in a wide variety of arrangements and configurations in engineering applications and in the natural environment. Among these plethora of conditions, few relevant examples are flows over plant canopies, atmospheric boundary layers, industrial flows such as oil and gas transportation, marine transportation as well as turbomachinary. Its main impacts are usually a faster transition from laminar to a turbulent flow, mixing enhancement and drag increase. Throughout the last century, a considerable amount of efforts were dedicated to the understanding and trials of finding a universality that would describe and predict the turbulent flow over roughness. Substantial reviews exist in the literature, among the recent ones Jiménez (2004), Castro (2007), Flack and Schultz (2014) and Squire et al. (2016). Surface roughness is known to induce a vertical and a horizontal shift in the logarithmic region of the velocity profile (see the U^+ vs y^+ plot from figure 2.2). This change is due to a momentum loss/gain relative to the smooth-wall one caused by an increase in friction, and the appearance of a virtual origin. The slope however, in addition to the smooth-wall universality issue, is still debated whether the roughness changes the value compared to the smooth-wall value (Schetz 1993; Amir and Castro 2011).

These modifications result in an equivalent relation of the log-law for turbulent boundary layer flows over rough walls which is expressed by

$$\frac{U}{U_\tau} = \frac{1}{\kappa}\ln\left((y-d)\frac{U_\tau}{\nu}\right) + B + \frac{\Pi}{\kappa}w\left(\frac{y}{\delta}\right) - \Delta U^+\left(\frac{hU_\tau}{\nu}\right), \tag{2.15}$$

where ΔU^+ and d are the roughness function and zero-plane displacement respectively, representative of the aerodynamic parameters of the roughness, and h is a reference roughness height which is geometry specific. While ΔU^+ simply translates the momentum loss/gain, various definitions exist for defining the two latter quantities d and h. d is commonly defined as the level of the actual mean momentum sink or the reference height for a velocity profile at which the mean surface shear appears to act (Thom 1971; Jackson 1981). This means the zero-plane displacement can be thought of as the height at which the mean drag starts acting on the flow (Castro, 2007) and it is generally a fraction of the height of the roughness elements (Amir and Castro, 2011). The reference h on the other hand is specific to the surface texture, height and roughness density. There exist a multitude of correlations between the roughness function and the surface properties and its statistics that have been proposed in various studies (see for example the review by Flack and Schultz 2010). Similarly, it is very common to use a proxy for

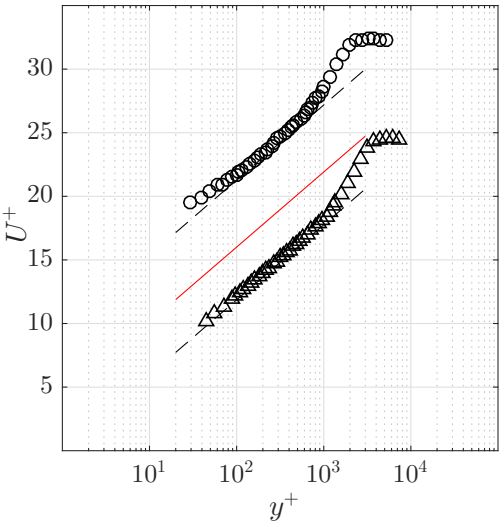

Figure 2.2: Inner-normalised velocity profiles of a turbulent boundary layer flow over a herringbone riblet surface investigated by Nugroho et al. (2013), illustrating a drag increase (triangle) and reduction (circle) respectively, while the red solid line represents the smooth-wall logarithmic distribution.

the roughness height known as h_s, which is the equivalent sand grain roughness height used in early drag predictions by Moody (1944) and popularised by Schlichting (1979) (which is discussed in the section 2.2.1).

Figure 2.2 highlights two velocity profiles scaled in inner units from a turbulent boundary layer over a herringbone riblet surface, with the latter characterised by a converging/diverging pattern (Nugroho et al., 2013). While a logarithmic behaviour is shown to occur for the velocity distribution, downward and upward shifts are observed illustrating both drag increase (positive ΔU^+) and reduction (negative ΔU^+) respectively.

From an engineering standpoint, the importance of the roughness function is that once $\Delta U^+ = f(h^+)$ is known for a given roughness, it can be used in order to predict the drag at a given flow condition, provided that the h or h_s of that surface is known. This can be achieved by subjecting the rough wall to increasing Reynolds numbers till ΔU^+ reaches a monotonic variation with respect to h^+ (Jiménez 2004; Castro 2007; Flack and Schultz 2014; Squire et al. 2016). This monotonic varying state of $\Delta U^+ = f(h^+)$ is termed the fully-rough regime, and offers an alternative way of expressing the rough-wall profile. It is commonly used in the meteorological research community and is expressed by

$$\frac{U}{U_\tau} = \frac{1}{\kappa} \ln\left(\frac{y-d}{y_0}\right), \tag{2.16}$$

where y_0 is the roughness length which quantifies the momentum deficit. ΔU^+ and y_0 are equivalent measures of roughness and related by

$$\Delta U^+ = B + \frac{1}{\kappa} \ln\left(\frac{y_0 U_\tau}{\nu}\right) = B + \frac{1}{\kappa} \ln\left(\frac{h U_\tau}{\nu}\right) + \frac{1}{\kappa} \ln\left(\frac{y_0}{h}\right). \tag{2.17}$$

2.2.1 Roughness characterisation

The characterisation of roughness has always been of great importance for both engineering and research communities, and many works have been proposed over the years. In the early 30's of the previous century, Nikuradse (1933) provided a compelling investigation of a turbulent flow over a roughened pipe surface, with various sizes of sieved sand glued to the surface. He observed for a given ratio of the pipe radius to the nominal height of the roughness (r/h), that the friction factor undergoes different regimes depending on the roughness Reynolds number h^+. He found that for $h^+ < 6$, the flow remained hydrodynamically smooth, with the skin-friction coefficient decreasing with a given slope. For $6 < h^+ < 70$, C_f was shown to increase sharply, then asymptotes to a constant value for $h^+ > 70$, terming the former the transitional and the latter the fully-rough regimes respectively. He also observed that by increasing (r/h), a proportional increase is obtained for the skin-friction coefficient in the fully rough regime. Combing the friction measurements with the velocity profile ones, he proposed a modified log-law valid in the fully-rough regime and is expressed by

$$\frac{U}{U_\tau} = \frac{1}{\kappa} \ln\left(\frac{y}{h}\right) + 8.5. \tag{2.18}$$

Following Nikuradse's benchmark study, Colebrook et al. (1939) collected results from several industrial pipe flows and proposed a universal interpolation formula expressed by

$$\Delta U^+ = \frac{1}{\kappa} \ln\left(1 + 0.26h^+\right), \tag{2.19}$$

which Moody (1944) later used to compute his very well-known skin-friction diagram. In the perspective of modelling the effects of surface roughness on the mean flow, Schlichting (1979) experimentally surveyed a range of surfaces both staggered and regularly distributed roughness made of spheres, cones and angular plates in the fully rough regime. Using his measurements, he proposed the concept of a roughness length scale which is equivalent to Nikuradse's sand grain roughness, hence the term *equivalent sand grain roughness height*. By assuming a universal logarithmic scaling law for the rough-wall profiles (i.e. universality of κ and B), he formulated a new expression for the roughness function based on h_s which is expressed by

$$\Delta U^+ = \frac{1}{\kappa} \ln(h_s^+) - 3.5. \tag{2.20}$$

He further equated Nikuradse's relation with his and provided a conversion formula that allows to obtain an equivalent sand roughness height, and is expressed by

$$\frac{h_s}{h} = e^{((8.5-A)/\kappa)}, \tag{2.21}$$

with A being the log-law intercept of a flow over a given surface of roughness height h, which can be determined empirically. However, Schlichting (1979) argued that the roughness function does not only depend on the relative roughness height, but can also be function of density, shape, texture and spatial distribution of the roughness. An example of a collection of studies by Jiménez (2004) regarding the roughness function for several rough surfaces as a function of the roughness Reynolds number is presented in figure 2.3. The figure includes the original results from Nikuradse (1933) as well as other surfaces such as uniform packed spheres, riblets and galvanised iron roughness. As pointed out by Schlichting (1979), the roughness function reaches a fully rough regime (collapse of all the data) at nearly $h_s^+ > 70$. Earlier to that stage, it varies considerably depending on the flow, and can even achieve a drag reduction for a particular type of roughness such as the riblets (Jiménez, 2004).

Subsequent studies tried to account for additional parameters besides the height of the roughness h, and there is currently ongoing research on wall roughness with a focus on this aspect. Few examples focused on the effect of roughness density (Sigal and Danberg, 1990), plane and frontal solidities (Van Rij et al., 2002), frontal surface roughness angle (Bons, 2010), the root-mean-square and skewness of the surface roughness (Flack and Schultz, 2010) or more recently the roughness effective slope (Napoli et al. 2008; Yuan and Piomelli 2014). Most of these surface correlations have been considered in cases where the roughness is homogeneously distributed. However, as observed is many recent studies (Vanderwel and Ganapathisubramani 2015; Yang and Anderson 2017; Anderson et al. 2018; Chung et al. 2018; Chan et al. 2018), heterogeneous surfaces have large-scale effects on the structure of the turbulent boundary layer and can potentially affect the aerodynamic drag differently, rendering these predictive tools questionable. The current investigation will attempt to address the effects of heterogeneous surfaces and will try to investigate possible ways of its characterisation.

2.2.2 Organised motion

High Reynolds number smooth-wall bounded turbulent flows are known to be populated by several types of coherent structures. Smits et al. (2011) categorised them into four principle classes which inherently take place altogether, namely, the near-wall streaks, hairpin vortices, large- and very-large-scale motions (LSMs and VLSMs respectively). The near-wall region is home to well-organised structures which were evidenced experimentally by Kline et al. (1967). The near-wall structures are known to form low-speed streaks that constantly stretch, lift-up and oscillate to then burst in the buffer region in sequences of motions knowns as sweeps and ejections (Corino and Brodkey, 1969), which were examined through the quadrant decomposition of the Reynolds shear stress component (Wallace et al., 1972). They were shown to have a nearly constant

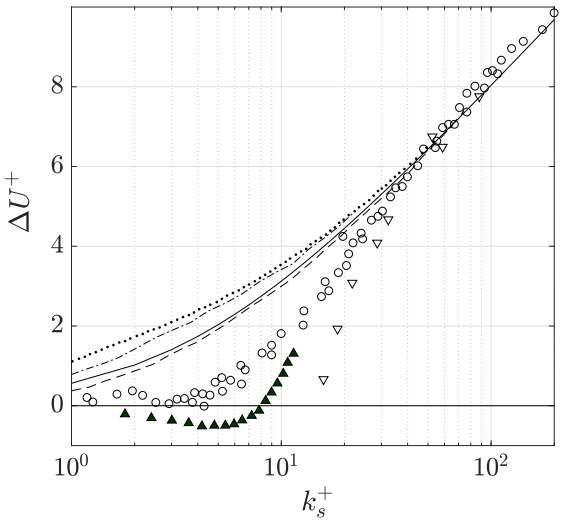

Figure 2.3: Variation of the roughness function for several rough surfaces with respect to the Reynolds number based on the equivalent sand grain roughness height. The circle symbol represents the uniform sand grain experiments of Nikuradse (1933), while the solid line represents Colebrook's relation (Colebrook et al., 1939). Results are replicated from the review article of Jiménez (2004).

width and length of about 100 and 1000 wall units respectively, and constitute the primary source of turbulence production.

The next class of coherent structures are defined as the horseshoe/hairpin vortices which were identified experimentally by Head and Bandyopadhyay (1981), however were mentioned in earlier works of Theodorsen (1952) and Townsend (1976) who termed them attached eddies instead. These hairpin vortices were shown to extend from the near-wall region through their legs up to the outer region through their head, which are characterised by an inclination of about 45^o. Their shape was shown to evolve from a horseshoe-like shape at low Reynolds numbers to a highly elongated hairpin-like structure at higher Reynolds numbers. Haidari and Smith (1994) investigated their generation mechanism and suggested that these structures result from the development of three-dimensional instabilities of a two-dimensional flow.

It was further shown that when they convect at the same speed, they organise themselves into packets of coherent structures forming the large-scale motions (Ganapathisubramani et al. 2003; Adrian 2007; Smits et al. 2011). These large-scale coherent structures are also refereed to as turbulent bulges whose streamwise extent vary between 1–3δ. Additional features known as very-large-scale motions (for pipe and channel flows) or superstructures (for turbulent boundary layers) were also identified (Kim and Adrian 1999; Hutchins and Marusic 2007; Monty et al. 2009). These structures attain a streamwise extent of 12–15δ for pipes and channels, and can reach 20δ in turbulent boundary layers. They are characterised by a spanwise meandering and their signature is highest in the upper edge of the logarithmic region. They are shown to be responsible for a fraction of the turbulence production/Reynolds shear stresses, and their contribution

becomes more important at high Reynolds numbers as these structures become more energetic (Adrian, 2007; Monty et al., 2009; Smits et al., 2011). To illustrate the organisation of the coherent structures, Kim and Adrian (1999) proposed a conceptual model as shown in figure 2.4, whereby hairpin vortices align coherently in groups of long packets to form the large-scale motions. Successively, these large-scale motions line up coherently to form in turn the very-large-scale structures.

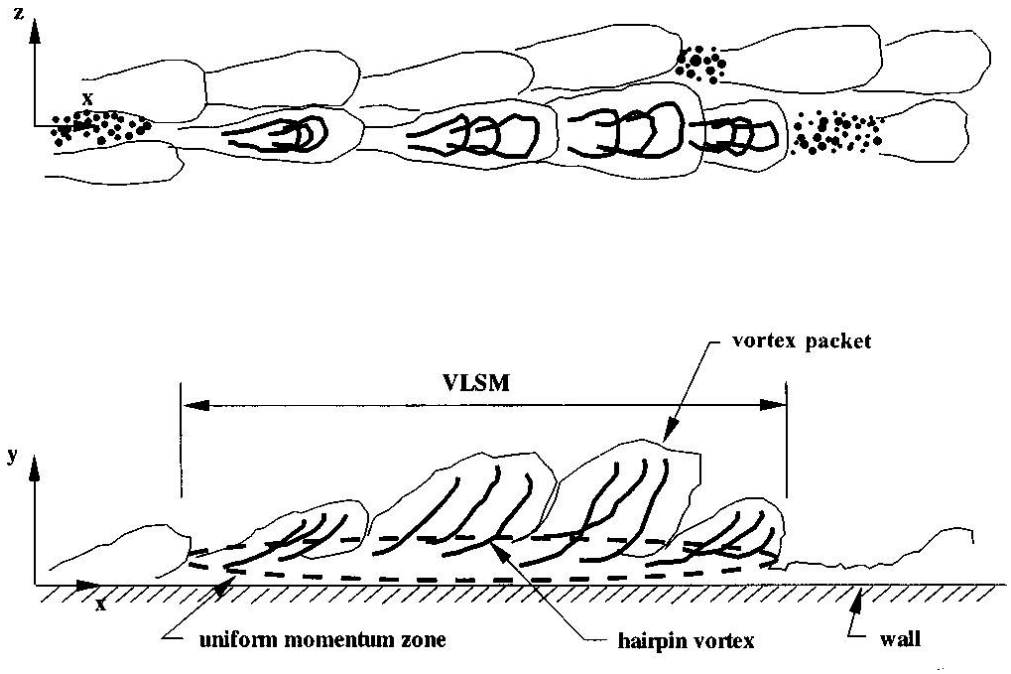

Figure 2.4: Conceptual model proposed by Kim and Adrian (1999) on the coherent structures conjecturing the organisation and alignment of hairpin vortex packets , large- and very-large-scale motions.

It is also interesting to mention that one of the debated questions involve the so-called inner-outer interactions, where researchers quested the possibility of large-scale structures affecting the near-wall small-scale structures. Hutchins and Marusic (2007) carefully examined the premultiplied energy spectra of the streamwise velocity fluctuations and highlighted at "high-enough" Reynolds numbers (i.e. large/small scale separations) that an outer spectral peak appears in the upper edge of the logarithmic region, owing to the energetic coherent structures. They showed that by increasing the scale separation, a footprint in the inner spectral peak is observed due to the energising coherent structures in the logarithmic region, suggesting that the amplitude of the near-wall small scales are being modulated by the large scales of the outer region. This was explicitly investigated and quantified by Mathis et al. (2009) who scale-decomposed the velocity signal (time-series of hot-wire measurements) into small- and large-scale components. They observed the small scales to carry an amplified signal when a large-scale structure is detected. By examining the correlation function of the large-scale signal with the envelope of the small-scale fluctuations, they showed the evidence of an amplitude modulation, supporting the hypothesis of the existence of the inner-outer interactions. It was further

shown that besides the amplitude modulation, a frequency modulation is also present and these effects intensify when the Reynolds number is increased (Ganapathisubramani et al., 2012).

2.2.3 Outer-layer similarity hypothesis

High Reynolds number turbulent boundary layers over smooth walls can be broken into inner- (viscous dominant) and outer- (inertial driven) layers. The first one consist of a viscous sublayer itself made of two parts. The linear sublayer where the Reynolds stresses are small compared to the viscous stresses, and the buffer layer where both the viscous and Reynolds stresses are of the same order of magnitude. In the outer region, the inertial forces are dominant and the flow behaves as a wake flow, bounded by a turbulent fluid below and a turbulence-free fluid above and is characterised by its turbulent/non-turbulent activity. The crossover between the inner and outer regions results in a logarithmic region also sometimes referred to as an inertial sublayer (also called the constant shear layer in the case of turbulent boundary layers) where the streamwise velocity profile is characterised by a logarithmic distribution reflecting a multiscale momentum cascade (Smits et al. 2011; Marusic et al. 2013).

When the flow is subjected to a rough surface condition, structural modifications occur especially near the wall, affecting both the mean flow and the turbulence properties. At high Reynolds numbers, the roughness protrusions generate strong wakes and shear layers that essentially inhibit/destroy the near-wall streak cycle. While the mean and turbulent flow within the canopy remain strongly inhomogeneous, vortical structures shed from the canopy still attain a certain depth of the flow, which also lead to spatial heterogeneities in the wall-parallel plane. This generally can extend up to five times the mean roughness height defining hence what is termed as the roughness sublayer (Jiménez 2004; Castro 2007; Flack and Schultz 2010; Squire et al. 2016). A comparative schematic between the mean (statistical) flow composition in terms of the classical layers highlighting the effect of surface roughness is provided in figure 2.5. The upper boundary of the logarithmic region in both the smooth and rough walls is given by the outer length scale and generally does not exceed 0.2δ. On the other, the lower boundary is no longer set by the inner units as in the smooth wall but instead is dictated by the extent of the roughness sublayer. The latter is commonly defined as the layer at which roughness effects are still distinguishable and is characterised by the appearance of significant dispersive stresses due to the flow spatial inhomogeneities of the flow. This is generally found to be between 3–5h in the wall-normal direction.

Extensive efforts were dedicated to try and assess the impact of surface roughness on the smooth-wall structural paradigm previously mentioned. Hong et al. (2012) investigated the characteristics of the coherent structures in a rough surface made of pyramids in a turbulent channel flow within and right above the canopy layer. Using a refractive

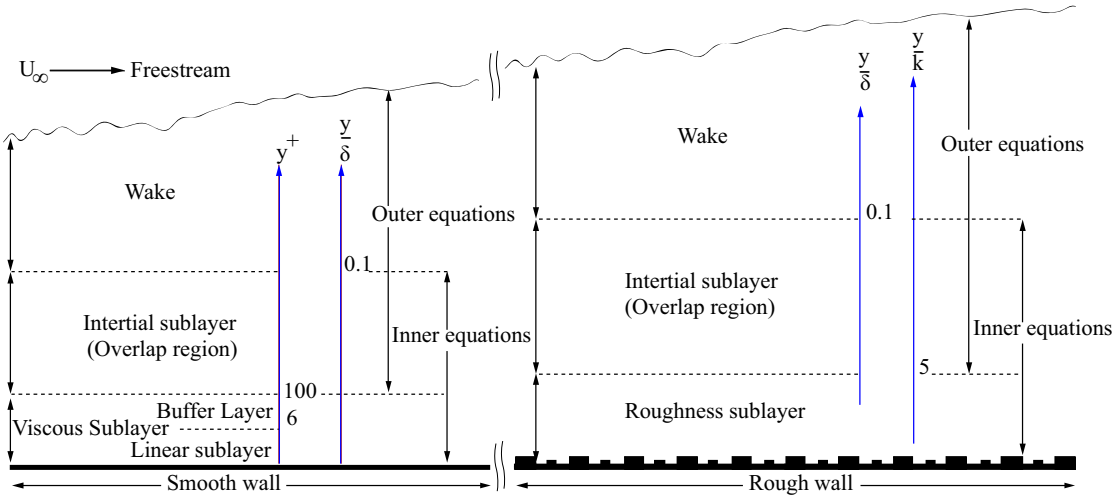

Figure 2.5: Generic representation of a high Reynolds number turbulent boundary layer flow over a (left) smooth- and (right) rough-wall, highlighting the layer decomposition.

index-matched facility, they were able to observe eddies whose extents are comparable to the roughness elements, which were shown to interact with the outer layer large-scale structures. Using conditional averaging, they highlighted large inclined shear layers containing negative vorticity bounded by ejections and sweeps below and above respectively. Their additional wall-parallel plane measurement added more information to the three-dimensional nature of the flow by emphasising pairs of counter rotating vortices at the intersection of two vortex trains. These signatures were explained to be part of a single coherent structure resembling a U-shaped hairpin (inverted classical Λ-shaped hairpin) that develops as the spanwise vorticity is stretched in the canyons between roughness elements. Relatively similar findings were reported in an earlier study by Finnigan et al. (2009) who investigated the turbulence structure above and within a vegetation canopy. Using both data from wind tunnel measurements and large-eddy simulations (LES), they observed that the roughness sublayer is home to characteristic eddies consisting of a downstream head-down sweep generating hairpin, superimposed to an upstream head-up ejection generating hairpin. They further argued that using this dual-hairpin model, an explanation can be provided as to why the sweep motions are more important than ejection motions in the roughness sublayer, as opposed to the classical hairpin model, which fails to provide a justification for this behaviour (Flack et al. 2005; Schultz and Flack 2005; Flack et al. 2007; Wu and Christensen 2007; Amir and Castro 2011). However, these near-wall (roughness sublayer) structures were only reported in a few studies, and it is very likely that their presence and nature highly depend on the surface condition, hence cannot be generalised to any type of rough surface.

In the outer layer (logarithmic and wake regions), hairpin packets were reported by several studies to be a prominent feature of rough walls similar to smooth walls. These were reported in flows over atmospheric boundary layers and urban-like roughness (Cheng and Castro 2002; Coceal et al. 2007; Inagaki and Kanda 2010; Placidi

2015; Jacob and Anderson 2017). They were also observed in highly ordered two- and three-dimensional roughness made of such as woven mesh, spanwise rods, sandgrains, sinusoidal or pyramidal topography (Krogstad et al. 1992; Flack et al. 2005, 2007; Volino et al. 2007, 2011; Guala et al. 2012; Marchis et al. 2015; Squire et al. 2016). They were shown to be additionally present in engineering surfaces, such as grooved, honed or riblet type, or simply surfaces damaged by deposition of foreign materials applicable in turbomachines (Shockling et al. 2006; Schultz 2007; Wu and Christensen 2010; Mejia-Alvarez and Christensen 2013; Pathikonda and Christensen 2017; Kevin et al. 2019; Barros and Christensen 2019).

A large number of the aforementioned studies share reasonable qualitative similarities regarding the organised motion in the outer layer of rough walls. The hairpin vortex packets in the inertial region contribute heavily to the Reynolds shear stress (Wu and Christensen, 2010). Roughness enhances the vertical inclination of the coherent structures caused by an increase in the velocity fluctuations. This causes a brake up of the large-scale motions near the roughness into smaller scales of the order of the mean roughness height, which in turn causes a shortening in the streamwise spatial coherence and a reduction in the turbulent stress anisotropy (Krogstad et al., 1992). The reduction in the streamwise spatial coherence of the LSMs as opposed to their smooth-wall counter part has also been hypothesised to be driven by the emergence of abundant isolated vortical structures emanating from the canopy layer, causing a reduction in the spacing between consecutive hairpins in the vortex packets (Wu and Christensen, 2010). However, it has also been reported that this reduction diminishes with increasing distance from the wall (Volino et al., 2011).

The similarity between the rough- and smooth-wall structural paradigms stems from an established concept of flow universality initiated by Hama (1954) which was formulated later on by Townsend as the Reynolds number wall-similarity hypothesis (Townsend, 1976). Its validity relies on two conditions: (i) a large separation between the inertial and viscous scales ($\delta^+ \gg 1$) and (ii) a small relative roughness height to the depth of the flow ($h/\delta \ll 1$). In virtue of these conditions, the streamwise velocity defect as well as turbulence quantities of the flow over rough and smooth surfaces can be hypothesised to have a universal form,

$$\frac{U_\infty - U}{U_\tau} = f\left(\frac{y}{\delta}\right), \qquad \frac{\overline{u_i u_j}}{U_\tau^2} = g_{ij}\left(\frac{y}{\delta}\right), \tag{2.22a, b}$$

where $\overline{u_i u_j}$ is the Reynolds stress tensor. The two functions $f(\cdot)$ and $g_{ij}(\cdot)$ are assumed to be universal in the outer layer and as such do not depend on the details of the surface condition. In other words, aside from affecting the near-wall region, surface roughness principally increases the drag (U_τ) and sets the boundary layer thickness (δ) while the turbulence structure remains unaffected by the surface condition. This hypothesis remains up-to-date a powerful predictive tool for engineers, since on one hand, it allows

the prediction of the turbulence distribution in a rough-wall flow at a given Reynolds number. On the other hand, the knowledge of the mean velocity distribution is sufficient to predict its drag (U_τ).

The validity of this hypothesis remains a subject of debate in the community, since there is need for both the achievement of high Reynolds number flows, besides its validation in generic rough surfaces. While the former condition can be relatively well-satisfied thanks to the existence of high Reynolds number facilities and an increase in computational resources, the latter seems less trivial since there is a large number of configurations of rough walls for which this hypothesis needs to be valid.

Early studies that provided experimental evidence of Townsends similarity hypothesis were carried out in several flow conditions such as a roughened pipe surface (Perry and Abell, 1977), a rough-wall boundary layer (Andreopoulos and Bradshaw, 1981) and a rough turbine blade (Acharya et al., 1986). The results highlighted a good collapse of the mean velocity defect profiles between smooth- and rough-wall flows, but also in the turbulence statistics. Later on, Perry and Li (1990) investigated both two- and three-dimensional rough walls in a boundary layer and showed not only Townsend's hypothesis is valid for the mean and turbulence structures, but also, the spectral characteristics of the turbulent length scales are self-similar. Following those works, there has been a large number of studies ever since providing support for the outer-layer similarity hypothesis (Raupach 1992; Schultz and Flack 2005; Connelly et al. 2006; Castro 2007; Volino et al. 2007; Wu and Christensen 2007). Squire et al. (2016) recently performed measurements of a high Reynolds number turbulent boundary layer over both smooth and rough walls. They examined the first, second and third order statistics as well as the spectra of the streamwise velocity fluctuations, and reported an excellent agreement between the smooth and rough wall results. Their comparison between the smooth and rough wall spectrograms is shown in figure 2.6 and clearly illustrated that apart from the near-wall region, the energy distribution among all wavenumbers in the outer region is the same (since the difference is nearly zero beyond the solid line).

Despite the overwhelming evidence and numerous experimental observations of outer-layer similarity, other researchers have pointed out that in some cases, rough-wall flows do not exhibit similarity with smooth-wall flows, since the roughness effects extend farther away from the wall. Krogstad et al. (1992) investigated a turbulent boundary layer flow over a mesh-type roughness, and reported a relative increase in the wake strength parameter despite a collapse in the mean velocity defect profiles. On the other hand, the turbulence stresses were shown to be considerably affected by the wall condition, as well as the sweep and ejections events when compared to the smooth wall in the outer region. They additionally showed the roughness signature in the velocity spectra across all wavemunbers, indicating the roughness sublayer has impacted the outer region. These results were further shown to extend even to the attributes of the coherent

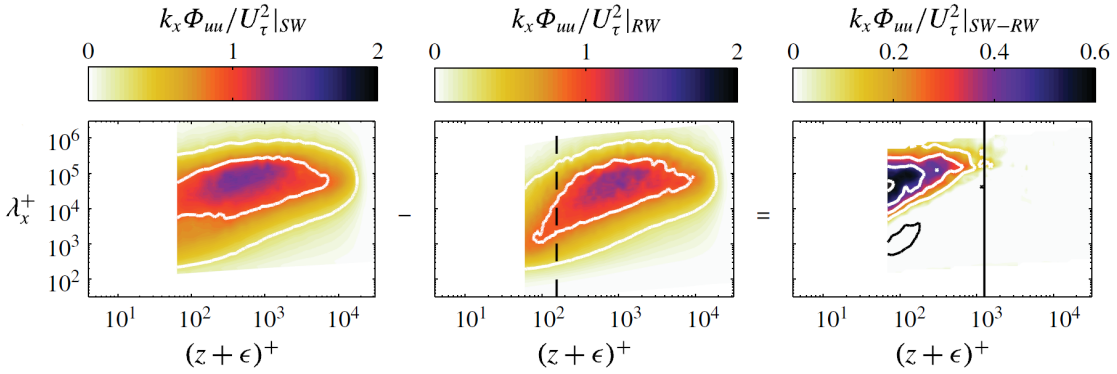

Figure 2.6: Comparison between the (left) smooth- and (middle) rough-wall premultiplied streamwise energy spectrograms at similar δ^+, and (right) their difference. The white lines compare the same contour level while the dashed and solid black lines represent the wall-normal location of h_s^+ and the edge of the inner region respectively. Result taken from Squire et al. (2016).

motions in the outer layer, with a large increase in the inclination of their spatial coherence and a shortening of the streamwise coherent length scales (Krogstad and Antonia, 1994). In a two-dimensional roughness configuration made of spanwise rods placed at a fixed streamwise spacing, Volino et al. (2009) examined the turbulence structures in a boundary layer. They reported significant changes in the turbulence motions characteristics in the outer flow, especially observed in the wall-normal and Reynolds shear stress intensities, despite the mean flow being qualitatively unaffected. As opposed to Krogstad and Antonia (1994), the scales of motions emanating from the roughness have led to an increased spatial coherence in the outer layer, while the hairpin packets exhibited similar inclination as smooth walls. Volino et al. (2009) attributed these changes to large-scale attached eddies which they argued are larger in the case of a two-dimensional (transverse bars) than three-dimensional (cube) roughness, originating from the roughness elements attaining the edge of the boundary layer. This apparent controversy has been addressed by several researchers (Jiménez 2004; Flack et al. 2007; Amir and Castro 2011) who proposed a relative roughness height based on the equivalent sandgrain roughness length scale h_s/δ instead of h/δ. From that perspective, if $k_s/\delta > 0.1$, the outer flow in expected to be affected.

Trying to characterise the effect of roughness in terms of relative roughness height only is not accurate enough to clarify the applicability of Townsends similarity hypothesis. In fact, in the recent years, there has been a growing interest in the study of flows over surfaces that have large-scale spatial variations. These surfaces were shown to lead large-scale mean and turbulent flow modifications, despite following the necessary conditions for outer-layer similarity (i.e. $\delta^+ \gg 1$ and $k/\delta \ll 1$). In a direct numerical simulation (DNS) of a pipe flow over spanwise-streamwise heterogeneous roughness, Chan et al. (2018) showed that the influence of the dispersive stresses (stresses originating from spatial inhomogeneity) highly depend on the spanwise wavelength. They showed for

wavelengths comparable to the pipe radius, the dispersive stresses extend further above the canopy layer, inducing lack of outer-layer similarity in the mean, turbulence and spectral characteristics. Chung et al. (2018) conducted a DNS of a channel flow over heterogeneous lateral shear stress surfaces, and similarly highlighted the importance of the spanwise wavelength. They demonstrated that for small wavelengths, the flow remains relatively homogeneous, with roughness effects confined in the near-wall region. However, for wavelengths comparable to the channel height, strong large-scale secondary motions occupy the entire flow, leading to an overall drag increase and the breakdown of local as well as global outer-layer similarity. It is interesting to point out that for studies that reported secondary flows, the above results are in contrast to other researchers observations that showed the existence of outer-layer similarity (Wu and Christensen 2007, 2010; Pathikonda and Christensen 2017).

There is still currently a debate about under which exact circumstances the similarity is valid. Two main problem with the available studies are that, to date, most of the literature on the validity of Townsends similarity concerns itself with homogeneous surfaces. In fact, studies involving heterogeneous surfaces where the turbulent boundary layer is subjected to large-scale changes such as the presence of secondary flows are less documented in the literature. Second, this examination requires the knowledge of the skin-friction velocity (U_τ), which is usually estimated through indirect means in most rough-wall boundary layer experiments (Reynolds shear stress profile or modified Clauser-chart). This leads to difficulties in determining the applicability of the similarity laws since there is significant scatter in the data due to various uncertainties. This leads to several questions with regards to these flows. For example, do these surfaces uniformly alter the entire boundary layer such that local skin friction is still sufficient to ensure outer-layer similarity? Can we apply a local similarity hypothesis in certain parts of a flow over a heterogeneous surface? If so, what does this similarity indicate about the entire flow? Before we address some of these questions, an overview of flow over heterogeneous surfaces and the importance of the skin friction are provided in the following sections.

2.3 Heterogeneous surface roughness

2.3.1 Types of surface heterogeneities

Among the various types of rough-wall topographies, spanwise heterogeneous surfaces earned an increased consideration owing to their presence in a wide variety of environmental and engineering applications. As mentioned in section 1.1, their examples span flows in rivers, wind farms, marine-fouled turbine blades, herringbone riblets, superhydrophobic surfaces among others (Nezu et al. 1993; Nugroho et al. 2013; Barros and Christensen 2014; Türk et al. 2014; Vanderwel et al. 2017). These surfaces

are characterised by a common length scale represented by their spanwise characteristic wavelength. If the latter is comparable to the dominant length scale of the flow, large-scale secondary motions can occur (Vanderwel and Ganapathisubramani 2015; Yang and Anderson 2017; Chung et al. 2018; Chan et al. 2018). Hence, in general, a surface can only be viewed of a homogeneous or heterogeneous nature after comparing its surface properties with the flow developing over it.

There are abundant parameters in the literature that are used to correlate the surface and aerodynamic properties of the flow. Whether it is randomly arranged, highly ordered or irregularly distributed roughness, it can have strong dependence on the amplitude, spacing, density, slope or directionality among other parameters. However, it has been suggested for secondary motion producing surfaces, the spanwise wavelength scaled with the dominant length scale of the flow (S/δ) characterises best the surface. To illustrate this, figure 2.7 shows a comparison between surfaces that do and do not exhibit a particular spanwise wavelength which can trigger secondary motions in the cross-plane hence leading to mean flow heterogeneity.

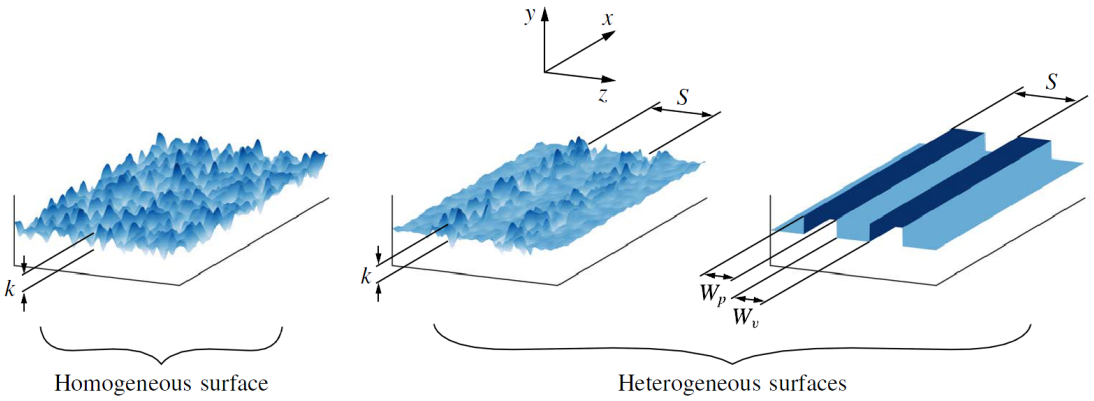

Figure 2.7: Comparison of homogeneous rough, heterogeneous rough and smooth surfaces. There are three related length scales which can be used to define the heterogeneity: The width of the peak or "high" roughness (W_p), the width of the valley or "low" roughness (W_v) and the spacing between adjacent valleys (S).

The heterogeneous class itself can be divided into multiple categories. In fact, several studies revealed the existence of the secondary motions generated over different surface conditions, which suggests the existence of different mechanisms responsible for such large modification of the primary flow. Kevin et al. (2017) discussed how different types of surfaces can exhibit secondary flows and proposed a classification based on the local isotropy/anisotropy of the skin-friction coefficient C_f. However, in addition to their classification, a different configuration can also be defined based on surface elevation variations, which would also indirectly lead to variations in local C_f. Therefore, surfaces can be topographically heterogeneous (alternating elevated and recessed regions), or frictionally heterogeneous (alternating high and low shear stress). Intuitively, a third category can be thought of as a hybrid between the first two classes. Examples of such surfaces have already been examined by researchers and are presented in figure

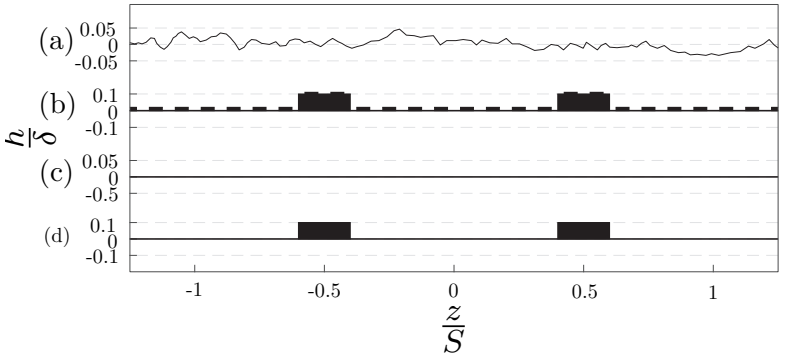

Figure 2.8: Comparison of the spanwise-profile surface topographies, between (a) Barros and Christensen (2014), (b) Vanderwel and Ganapathisubramani (2015), (c) Kevin et al. (2017) and (d) an example of a surface tested in the current investigation.

2.8. Figure 2.8 illustrates a comparison between different types of surfaces from three different studies that have reported development of these time-averaged secondary flows.

2.3.2 Turbulence-driven secondary flows

The seminal work of Nikuradse (1930) on the turbulent flows in non-circular pipes has highlighted the presence of important large-scale features known as secondary flows. These structures embedded within a primary flow manifest in the form of streamwise vortices. Prandtl (1952) showed they can exist in various flow conditions, and classified them in two kinds based on their generation mechanism. The first kind is generated due to mean flow skewness such as in pipe systems with curvatures, whereas the second kind originates from turbulence anisotropy such as in straight non-circular duct flows.

Until the late sixties, the majority of efforts routed towards the description and understanding of these two kinds of secondary flows in the presence of smooth surfaces. The introduction of surface roughness was probably first carried out by Hinze (1967, 1973). Hinze experimentally investigated the secondary flows in a rectangular duct with a partially corrugated wall. He observed the occurrence of turbulent secondary flows in both, the duct corners as well as in the rough-to-smooth spanwise step-change. Using hot-wire anemometry, Hinze examined the turbulent-kinetic energy (TKE) balance equation at the plane of symmetry and concluded that at a high enough distance from the wall, a secondary flow is induced by virtue of the turbulence production and viscous dissipation imbalance. He showed that the imbalance is caused by the anisotropy in the turbulence stresses, which itself is consequence of the wall condition. He reported that downwash and upwash motions occurred above the high and low drag strips respectively.

Secondary flows have also earned an increased interest in the hydraulics research community, since in fluvial processes, they are often associated with the formation of bedforms and cause variations in the topographical sediment distribution (Colombini, 1993;

Gyr and Kinzelbach, 2004). Nezu and co-workers performed both field and laboratory experiments in order to investigate secondary flows (Nezu and Nakagawa, 1984; Nezu et al., 1993). In order to reproduce the bedforms effect in laboratory, they have used alternating ridges of trapezoidal shapes at different spanwise spacings. They found that for a spacing equivalent to the flow depth, strong secondary flows are produced. They showed that the upwash and downwah motions occurred above the ridges and valleys respectively, inducing significant spanwise mean flow, turbulence and drag heterogeneity. Following the previous results, McLelland et al. (1999) conducted experiments of an open channel flow over a bed formed of bimodal sand gravel mixture with uniform heights. They observed that after less than an hour of continuous flow, sorting of particles is observed with coarse and fine sediments alternating in the spanwise direction, indicating that secondary flows occurred. They further reported that the fine sediment is entrained from regions of high shear stress and deposited in regions of low shear stress. This process enhances the lateral fluctuations which leads to higher gradient in the Reynolds stresses and turbulence anisotropy, generating a self-sustained process. In light of the previous results, Wang and Cheng (2005, 2006) carried out open channel flow experiments in both situations, bedform (topographical)-type and strip (wall-drag)-type. Similarly to the previous studies, they noticed pairs of counter-rotating cells at the roughness discontinuity with an upwash occurring over the smooth strip, and downwash over the rough strip. In the case of alternating ridges, they reported the upwash and downwash to occur over and in between ridges respectively, also in agreement with the previous findings.

During the last decade, a significant amount of research was conducted thanks to the advances in computational and experimental resources. In fact, it became naturally questionable with the presence of secondary flows, whether the established concepts of homogeneous roughness from which traditional predictive tools are derived remain applicable. In a highly irregular surface roughness replicated from a damaged turbine blade, Mejia-Alvarez and Christensen (2013) performed wall-parallel field measurements within the roughness sublayer of a boundary layer. They reported that in the time-average sense, the roughness promoted flow channeling in the form of high- and low-momentum pathways, with an enhanced turbulent and vortical activity in the boundaries of the high- and low-momentum pathways (HMPs and LMPs respectively). In a follow-up study, Barros and Christensen (2014) performed cross-plane field measurements and clearly identified the presence of secondary flows, despite the roughness topography being highly irregular. They showed that the LMPs (upwash) and HMPs (downwash) occurred above recessed and elevated parts of the topography, with the LMPs being home to enhanced turbulent kinetic energy as well as Reynolds shear stresses.

Anderson and co-workers performed a series of large-eddy simulations to model the flow over both types of surface heterogeneities. In a boundary layer flow over transverse aerodynamic roughness transition (strip-type), Willingham et al. (2014) observed the

LMPs and HMPs to be located above regions of low and high roughness respectively. They showed that the LMPs are sustained by the transverse mixing induced by the drag discontinuity, and the width of the high roughness influences strongly the strength of the mixing, as opposed to a lesser influence of the ratio of the high-to-low roughness. A follow-up study by Anderson et al. (2015) examined the secondary flow mechanism from both experimental and numerical measurements. They showed that by considering the TKE transport equation, local cross-plane variations in the Reynolds stresses create an imbalance between production and dissipation, thus causing the amplified radial motions which is in agreement with Hinze's findings (Hinze 1967, 1973). They also found by analysing the streamwise vorticity transport equation, vorticity production is sustained by the Reynolds stress anisotropy, supporting that these secondary flows are Prandtl's second kind. In the ridge-type register, Yang and Anderson (2017) studied topographical-driven secondary flows in a channel flow, and found that the lateral spanwise spacing between ridges represents an important scaling parameter of the heterogeneity. In fact, it could indicate the existence or absence of structural similarity depending on whether the flow behaves homogeneously or heterogeneously. Similar results were shown in an earlier experimental study by Vanderwel and Ganapathisubramani (2015). They reported that the spanwise spacing between ridges in a rough surface dramatically affects the strength and size of the secondary flows. By systematically varying S/δ (the spanwise spacing relative to the boundary layer thickness), they demonstrated that the secondary motions can only emerge beyond a certain value of S/δ, reach their full potential when $S/\delta \approx \mathcal{O}(1)$ then reduce in strength for larger spacings. Interestingly, the location of the upwash and downwash motions was shown to be different for these two studies. Vanderwel and Ganapathisubramani (2015) observed the upwash to occur over the ridges similar to Nezu and Nakagawa (1984) and Wang and Cheng (2006) whereas Yang and Anderson (2017) showed their occurrence above the recessed region of the surface.

Several additional studies have been conducted by researchers on other types of surfaces. Nugroho et al. (2013) investigated a turbulent boundary layer flow over a converging-diverging riblet-type, and reported large-scale periodicity in the form of HMPs and LMPs. They observed large modifications in the spectral characteristics of the turbulent structures within those regions, and an increased energy content at the LMPs than the HMPs. Subsequent studies by Kevin et al. (2017, 2019) on the same surface revealed the existence of counter-rotating cells, which led to strong spanwise variations in the Reynolds stresses and TKE fields accentuated above the upwash region. The latter harbours large-scale low-momentum regions with strong lateral meandering in the outer region, which induces a diagonal tilt in the coherent structures between the HMPs and LMPs. This is shown to enhance lateral momentum transfer, also depicted by a frequent large-scale turbulence-free stream engulfing behaviour above the HMPs. Spanwise structural modifications were also reported by Bai et al. (2018), who performed wall-parallel field measurements of a turbulent boundary layer over alternating smooth

and rough patches. They observed in the log region, the spatial coherence of the low-speed streaks to be increased over the LMPs and decreased over the HMPs, with an enhanced meandering over the HMPs. Similarly, between the LMPs and HMPs, the turbulent structures showed a yawed coherence caused by the lateral flow. Secondary flows were also observed over surfaces with alternating no-slip and free-slip boundary condition mimicking superhydrophobic surfaces. Türk et al. (2014) and Stroh et al. (2016) reported that a vortex pair located above the discontinuity is formed, with downwash over the free-slip and upwash over the no-slip. Increasing the spanwise wavelength led the instability to bifurcate as a new vortex pair of much larger scale appears and acts oppositely to the primary pair, inducing the HMPs and LMPs to be located above regions of no-slip (high drag) and free-slip (low drag) regions respectively.

In a DNS of a pipe flow over spanwise-streamwise staggered heterogeneous roughness, Chan et al. (2018) reported that the size of the secondary flows (as well as the dispersive stresses) highly depend on the spanwise wavelength. They showed for wavelengths comparable to the pipe radius, the secondary motions increased in their strength and size. Similarly, Chung et al. (2018) conducted a DNS of a channel flow over heterogeneous lateral shear stress surfaces, and highlighted the importance of the spanwise wavelength. They demonstrated that for small wavelengths, the flow remains relatively homogeneous, with secondary motions confined in the near-wall region. However, for wavelengths comparable to the channel height, strong large-scale secondary motions occupy the entire flow. Furthermore, in a similar surface configuration to that presented in chapter 4, Hwang and Lee (2018) investigated using a DNS the effect of the ridge width as well as the spanwise wavelength. They argued that the size of the secondary flow scales with the valley width, while its strength is essentially influenced by the spanwise wavelength. Likewise, they have demonstrated that the secondary flows result from the turbulence anisotropy. Finally, by examining the TKE budget, they argued that the rotational sense of these secondary flows can be inferred from the imbalance between production and dissipation.

In light of these numerous reviews and studies, we want to further investigate some of the following questions: Is it possible to predict the location of the upwash and downwash motions for the topographical heterogeneous surfaces based on geometrical information rather through the turbulence energy production/dissipation imbalance? What are the other relevant length scales that carry the heterogeneity information? Can outer-layer similarity still be satisfied in the presence of secondary flows under certain conditions?

2.4 Skin-friction drag

2.4.1 Importance of the skin friction

The skin friction represents a result of the conversion of the free stream momentum into a shear force by means of the turbulent boundary layer. Due to the increasing interest to reducing the energy consumption and the environmental impact from fuel-consumption-based systems, the accurate measurement of this quantity is as important to engineers as to researchers. From an engineering perspective, the prediction of C_f is crucial in order to accurately design aerodynamically efficient vehicles (e.g. submarines, aircraft, ships, cars etc.). In fact, the frictional contributions can reach up to 50% of the total drag for an airliner at a cruising speed, and can raise up to 90% for ships while it represents almost all of the pressure losses in internal flows (Von Karman 1934; Moody 1944; Hoerner 1965; Marusic et al. 2013). Besides the engineering expectation, the accurate knowledge of the skin friction simply improves numerical predictive tools that rely on wall functions such as large-eddy simulations. On the other hand, the skin friction is of crucial importance since it's providing understanding of wall turbulence dynamics, by being a scaling quantity for both the near-wall as well as the outer region of the turbulent boundary layer. Perhaps more importantly for this work, the only way to examine whether the outer-layer similarity hypothesis is valid or violated in our investigation is the accurate measurement of this quantity.

2.4.2 Measurement of skin friction

Any investigation of a turbulent boundary layer necessitates the measurement of the wall shear stress, since this quantity influences strongly the fluid motion near the wall. It is well known to be a major scaling parameter of wall-bounded flows, with a high degree of universality whether smooth or rough wall, and with or without pressure gradient. Despite its importance and the relentless efforts from researchers, the wall shear stress always remains a challenging quantity to determine.

There are two types of method that can be distinguished in the literature; indirect methods and direct methods. As opposed to direct methods, indirect methods essentially rely on mean and turbulent flow profile assumptions in order to be used, and by definition infer the wall shear stress rather than measure it directly at the wall. A commonly used way is to deduce the friction velocity from the log region of the mean velocity profile, using the Clauser chart method (Clauser, 1956). The main drawback of this method is that a hypothesis has to be made on the value of the Von-Karman constant and the smooth-wall intercept, which are known to vary across different wall conditions (boundary layers, pipes and channels). In case of rough walls, a modified Clauser chart can also be used following the procedure of Perry and Li (1990), where the method is

based on the determination of the virtual origin by an assumption of a linear variation of U/U_∞ with $ln(yU_\infty/\nu)$. Assuming the validity of this log region between $yU_\tau/\nu \geq 100$ and $y/\delta \leq 0.2$, U_τ is determined as

$$U_\tau = \kappa U_\infty \left[\frac{\partial(\frac{U}{U_\infty})}{\partial(ln(\frac{(y-d)U_\infty}{\nu}))} \right]. \tag{2.23}$$

Another profile-based method for boundary layer flows is the total shear stress, which assumes that a constant shear stress region equal to the wall shear stress exists in the overlap region. Adding viscous and turbulent shear stresses, the friction velocity can then be calculated from the profile plateau found to be characteristic of the overlap between the inner and outer layers (Schultz and Flack, 2005),

$$U_\tau = \sqrt{\nu \frac{\partial U}{\partial y} - \overline{uv}}. \tag{2.24}$$

Another alternative is the classical momentum thickness gradient method also known as the Von-Karman momentum integral method (Von Karman, 1934). The wall shear stress is related to the momentum and displacement thickness and is expressed as

$$\tau_w = \rho U_\infty^2 \left[\frac{d\theta}{dx} + (H+2)\frac{\theta}{U_\infty}\frac{dU_\infty}{dx} \right]. \tag{2.25}$$

with H being the shape factor defined as the ratio between the displacement thickness δ^* and the momentum thickness θ. However, not only the turbulence terms are neglected in this form, but the determination of the gradient quantities in the streamwise direction requires a sufficient distance for the growth of the flow, which renders it use impractical in most experiments. The practicality of these methods have also other drawbacks, where additional uncertainties in velocity and probe location measurements can directly influence the estimation of wall shear stress, leading to higher uncertainties of the order of 10% to 20% (Connelly et al., 2006). There exists several other profile-based techniques, and for a more detailed review of their advantages and limitations the reader is refereed to the recent work by Orlu and Vinuesa (2017).

On top of its typical difficulty to experimentally measure the wall friction in smooth walls (pure viscous drag), the impact of roughness and its additional pressure drag makes the task even more complicated by limiting the number of measurement techniques which can be used. Therefore, the use of a direct method becomes more appropriate if it is feasible in rough walls.

There are several studies that have reviewed these methods and their applications (Fernholz and Finleyt 1996; Naughton and Sheplak 2002; Ruedi et al. 2003). These techniques can be divided into several categories, floating-element-based, pressure-based, heat-transfer-based and optical-based methods. Perhaps the oldest direct measurement

system that is able to measure the skin friction is the floating-element drag balance. This method is generally used in high shear stress flows such as rough walls and it is based on directly measuring the force exerted by the incoming flow on a sensing surface, mounted parallel to the wall. By knowing the drag force experienced by the floating element, it becomes straightforward to deduce the wall shear stress of a given surface. Ferreira et al. (2018) reported that the skin-friction coefficient determined in the case of a smooth-wall flow can be within 2% uncertainty, while for rough walls the it can even be below 1%. The most common issues encountered when setting a floating-element drag balance are mainly due to the effect of the air gaps between the floating-element and the surrounding surface, pressure gradients, leaks or simply surface misalignment.

An alternative method is the Preston tube which essentially relies on the pressure difference between a classical Pitot tube resting at the wall and a static pressure port drilled through the surface (Tropea and Foss, 2007). This technique however makes use of the assumption that the log-law is valid (universality of κ and B), and also requires a calibration that involves relating the friction velocity against the pressure difference. Besides the calibration uncertainties, the main source of errors encountered when using this method is related to the tube being misaligned to the incoming flow. Other methods are also used such as Stanton tube (high frequency response version of the Preston tube) and sublayer fence. However, their employability for rough walls can be limited depending on the roughness arrangement.

Other measurement techniques such as hot film makes use of the fact that the heat transfer rate relates to the wall shear stress. These are basically metal-based sensors located at the wall, which are heated by means of a constant temperature anemometer. However due to a partial heat loss dissipated at the substrate, this method performs well under fluids of high conductivity such as water, and are less effective in air. The alternative is to use wall hot wires which are the equivalent classical hot wire probes, but installed at the surface, with the advantage of providing a high frequency response. The main sources of uncertainties of these techniques are the temperature changes which cause drifts and calibration errors, as well as the difficulty to mount on a rough surface.

There are also techniques based on optical measurements such as oil-film interferometry and particle image velocimetry (PIV). Their main advantage is the degree of intrusiveness which is mitigated compared with the previously mentioned methods. Similarly to the floating-element drag balance, there is no need to calibrate the sensor based on a heat transfer or pressure measurement basis, hence reducing the overall uncertainty of the techniques. Oil-film interferometry is based on the relation between the thinning rate of an oil film/droplet deposited on the surface and the shear stress applied by the incoming flow (Naughton and Sheplak, 2002). It has a high degree of accuracy in estimating the mean wall shear stress similar to the drag balance, however remains impractical for non smooth walls. Its main drawback remains that its viscosity, which is sensitive to temperature changes, hence the rate at which the film/droplets gets sheared.

Otherwise, particle image velocimetry, or more specifically particle tracking velocimetry (PTV) can reveal to be an interesting option. In fact, Kahler et al. (2013) was able to assess the mean wall shear stress with high accuracy, by measuring the mean velocity profile down to the viscous sublayer where the mean velocity is known to vary linearly with the wall distance. The main difficulty of this method is linked to the use of a long distance microscope and a micro-PIV type of approach in order to resolve the very near-wall region, but can similarly be less effective when the studied surface presents rough protrusions.

Given that the current investigation interests itself in the response of a turbulent boundary layer subjected to smooth heterogeneous surfaces, oil-film interferometry is privileged since these surfaces do not experience any pressure drag (absence of streamwise protrusions). This will allow us to examine the spanwise variation of the viscous drag as a result of surface heterogeneities. Overall, this will provide us with an unambiguous assessment of the outer-layer similarity hypothesis using direct measurements. This will enable us to identify the applicability and limitations of these similarity laws in turbulent boundary layer flows over heterogeneous surfaces.

3. Experimental methodology

In this chapter, the experimental facility, test cases and measurement techniques involved are described. First the facility where the measurements were carried out is described. Followed by the roughness arrangements being used on top of the boundary layer flat plates. Then the test cases undertaken are presented, completed by the description of the measurement techniques and procedures employed to investigate the present problem.

3.1 Wind tunnel facility

The experimental investigations were conducted in an open-circuit suction type wind tunnel at the University of Southampton, in which several rough-wall studies have been documented (e.g. Reynolds et al. 2007; Vanderwel et al. 2017). As illustrated in figure 3.1, the extent of the working section is 0.6 m $\times$ 0.9 m $\times$ 4.5 m in (y, z, x); wall-normal, spanwise and streamwise directions respectively. The wind speed velocity generated can reach up to 30 m/s, with a turbulence intensity measured to be less than 0.5%. The fan speed is controlled through an analogue output from an NI-USB-6212 National instrument Data-Acquisition system (DAQ), which in turn is controlled by a MATLAB program. The wind speed is acquired using a microprocessor based FC510 manometer. The instrument is operated by connecting it to a Pitot probe, which measures the dynamic pressure processed and acquired digitally through the DAQ, then reduced to velocity using the Bernoulli equation: $U = \sqrt{\frac{2\Delta P}{\rho}}$. Atmospheric pressure changes are also accounted for in the wind tunnel laboratory through recordings from a weather station. The side as well as the top and bottom walls of the test-section are all made of acrylic in order to allow optical measurements when necessary.

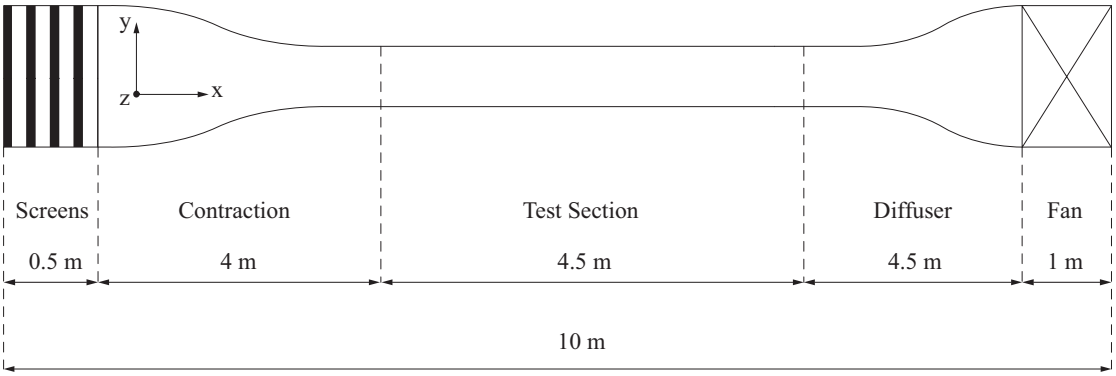

Figure 3.1: Schematics of the 3×2 open-circuit suction type wind tunnel at the University of Southampton.

3.2 Surface arrangement

Two sets of flat walls are used during the measurement campaigns. The first set was used for the experiments described in section 3.2.1 and discussed in chapter 4, while the second set was used for the experiments described in the sections 3.2.2 and 3.2.3, and discussed in the chapters 5 and 6 respectively. Both sets of surfaces are illustrated in the sketch of figure 3.2.

The first set (see figure 3.2(a)) is composed of aluminium flat plates making the

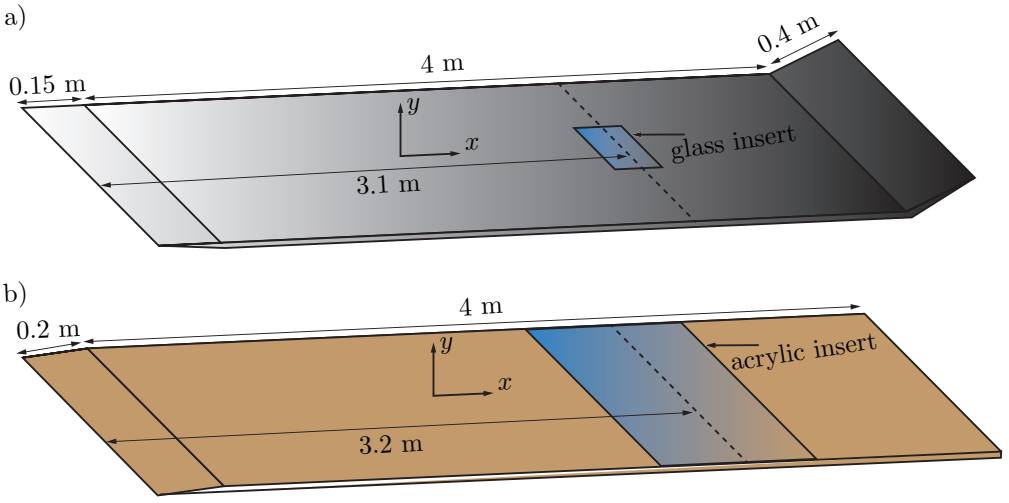

Figure 3.2: Schematics of the two sets of surfaces used where the boundary layer flow develops, with (a) used for the experiments described in section 3.2.1 while (b) is used for the experiments described in the sections 3.2.2 and 3.2.3. The streamwise location of the measurement locations for all the experiments were nominally set at $x = 3.1$ m for **Experiment 1** and $x = 3.2$ m for **Experiment 2**. For **Experiment 3**, the streamwise locations were varied between $x = 2.7$–3.4 m to investigate the streamwise step-change effect on the flow.

baseboard where the growing turbulent boundary layer is measured, and are made of four parts each 0.9 m long, in addition to three extra panels. The leading edge flat plate which consists of a plate of 0.15 m long with a sharp leading edge inclined to the horizontal by 15°. An additional 0.5 m long plate to cover the whole test section area, and finally a flap plate that is 0.4 m long, with an adjustable angle that ensures a constant pressure gradient along the measurement area, allowing to reach an overall distance of 4.25 m. The plates were positioned 0.15 m above the floor of the wind tunnel test section. The TBL is tripped at 50 mm from the leading edge using a zig-zag turbulator tape of 6 mm point-to-point and 0.5 mm thickness, allowing a turbulent boundary layer thickness δ growth of around 50 mm for a smooth surface with an Re_τ of approximately 1000. The pressure gradient was assessed at different speeds, and was measured by traversing the Pitot static probe in the streamwise direction, resulting in a pressure gradient of the order of $\frac{dP}{dx} = 0.2$ (Pa/m). This resulted in an acceleration parameter $K = (\nu/U_\infty[dU_\infty/dx])$ less than 3×10^{-8}.

The second and third measurement campaigns were performed over wooden-floor based flat plates (figure 3.2(b)), composed of four equally-sized boards of 0.9 long; three of which are made of wood over which gloss-PVC plastic sheets are bonded to, ensuring a smooth texture. A fourth board made of clear perspex is used to allow skin-friction measurements using the oil-film interferometry technique. The boundary layer plates are preceded by a ramp of 0.2 m long inclined by 4° to the horizontal ensuring a smooth transition of the flow from the bottom floor of the test section to the boundary layer plates. Similarly, the flow is tripped using a 6 mm point-to-point zig-zag turbulator tape of 0.5 mm height at 0.26 m downstream the leading edge of the ramp. A-priori, the wooden boards were painted with a PVA-water mixture in order to ensure they are humidity-proof to avoid bending. The panels are bolted down to the wind tunnel floor, and are ensured to be flat and horizontal to allow a turbulent boundary layer growth over a smooth surface. Similarly, the resulted acceleration parameter $K = (\nu/U_\infty[dU_\infty/dx])$ was less than 5×10^{-8}.

3.2.1 Experiment 1

The first problem investigated focuses on the effect of ridge spanwise spacing (heterogeneity length scale) on both viscous drag and turbulence characteristics. Second, the assessment of outer-layer similarity in the presence of spanwise heterogeneity for different Reynolds numbers. In order to model the spanwise surface elevation, a rectangular smooth foam tape (Self Adhesive EPDM Blend Sealing Strip) with a cross-section $h \times W$ of 5 mm $\times$ 20 mm is chosen. The longitudinal ridges are used to create the surface heterogeneity by varying the spacing between adjacent ridges by 40, 80 and 160 mm as shown in figure 3.3(b), such that $0.8 \leq S/\delta_{av} \leq 3.2$, where δ_{av} in **Experiment 1** represents an approximation of the spanwise-averaged boundary layer thickness measured

from the hot-wire profiles along the span. These spacings will be referred to as cases X1HS1, X1HS2 and X1HS3, respectively. The surface texture of the foam tape was scanned and its roughness characteristics length was found to be less than 30 μm, which represents a ratio of the roughness to the viscous length scale less than 2 wall units (at the highest Reynolds number examined in this study), hence can be considered to be a hydrodynamically smooth ridge. The geometrical characteristics of the three cases are summarised in the table 3.1, while figure 3.3 highlights the experimental set-up using hot-wire anemometry and oil-film interferometry to measure the velocity and the skin friction respectively. The details about the employed measurement techniques will be discussed in the sections 3.3.1 and 3.3.2.

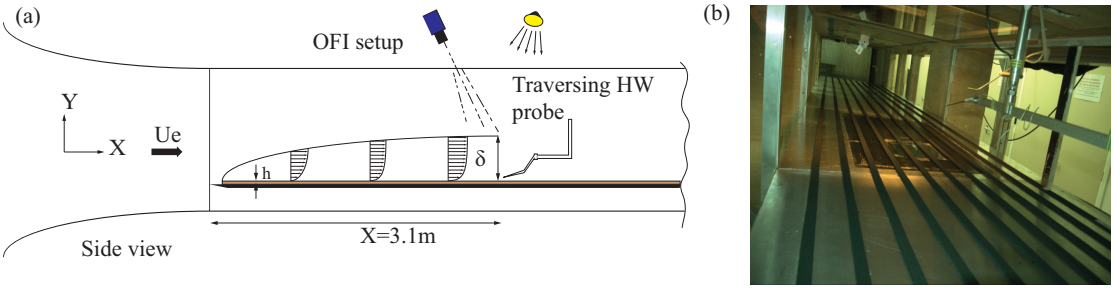

Figure 3.3: (a) Side view of the experimental setup used in the first measurement campaign using hot-wire anemometry and oil film interferometry. (b) View of the inside of the test section while setting up the X1HS2 case.

Case	h (mm)	W (mm)	S (mm)
X1HS1	5	20	40
X1HS2	5	20	80
X1HS3	5	20	160

Table 3.1: Geometrical characteristics on the surfaces used in **Experiment 1**.

3.2.2 Experiment 2

The overarching aim of this experiment is to document the characteristics of these three-dimensional flows. Similarly, we investigate the flow over a smooth ridge-type heterogeneous surface and assess the effect of shape and width of the ridges. Idealised heterogeneous surfaces were created using different profiles of smooth ridges made of clear perspex (with the same surface texture as the smooth wall). These profiles are selected in order to assess the secondary flow sensitivity to shapes and widths. A semi-circle, a triangle and a square are used for the study of the shape effect, while three rectangles with different widths W are used to investigate the width effect. These surfaces will be referred to by their labels X2HS1 to X2HS6 as shown in figure 3.4.

Their maximum heights h (6 mm) and spanwise spacings S (80 mm) were chosen to match 0.1 and 1 times the spanwise-averaged boundary layer thickness δ, respectively,

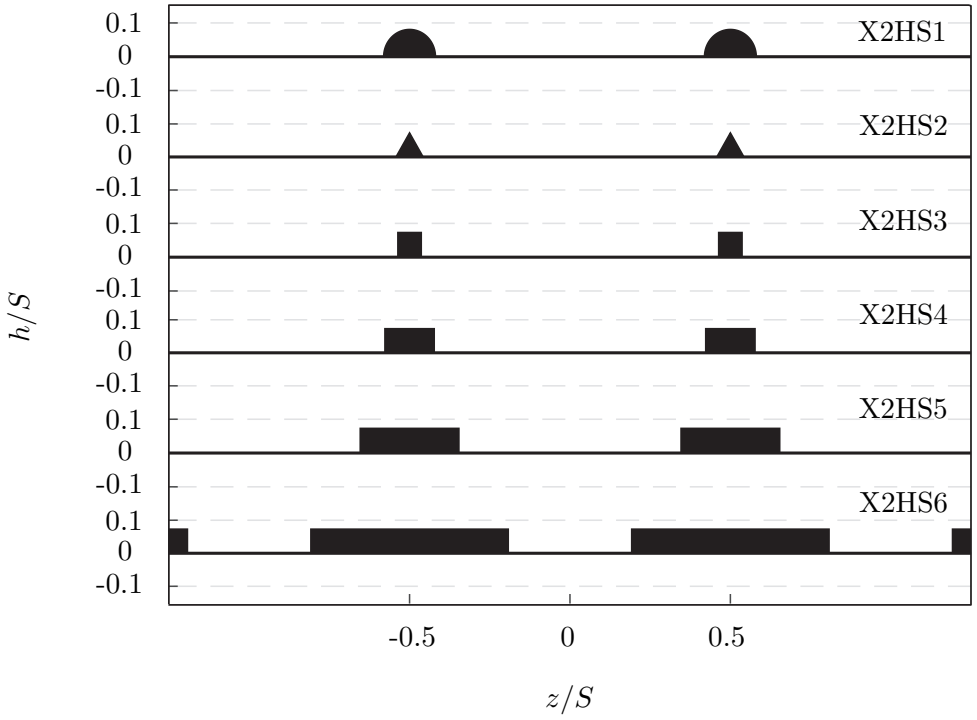

Figure 3.4: Schematics of the different geometries tested in the present investigation, with the cases X2HS1, X2HS2 and X2HS3 representing the shape effect while X2HS4, X2HS5 and X2HS6 representing the width effect.

in order to maximise potential secondary flows (Vanderwel and Ganapathisubramani, 2015). The geometrical characteristics of the six cases are summarised in the table 3.2, while figure 3.5 highlights the experimental set-up using stereoscopic PIV and oil-film interferometry to assess the velocity fields and the skin friction respectively. The details about the employed measurement techniques will be discussed in the sections 3.3.1 and 3.3.3.

Case	h (mm)	W (mm)	S (mm)
X2HS1	6	12	80
X2HS2	6	6	80
X2HS3	6	6	80
X2HS4	6	12	80
X2HS5	6	24	80
X2HS6	6	48	80

Table 3.2: Geometrical characteristics on the surfaces used in **Experiment 2**.

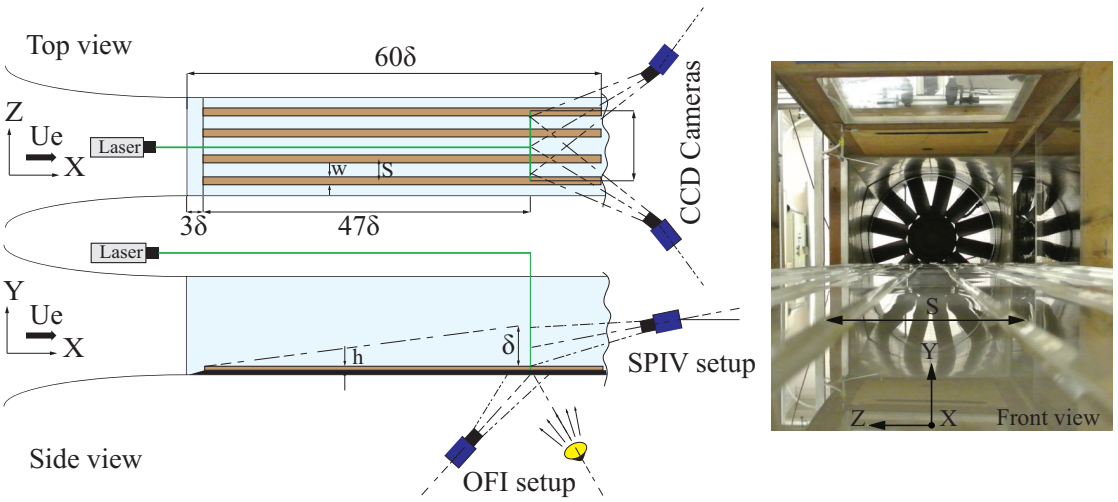

Figure 3.5: Left: Top and side view of the experimental setup and configuration of the experimental techniques employed during the second measurement campaign. Right: View from the inside of the test section. The streamwise measurement location was fixed at $x = 3.2$ m $\approx 50\ \delta$.

3.2.3 Experiment 3

In this third measurement campaign, we specifically want to examine the spatial evolution of these large-scale secondary motions along with their impact on the frictional drag as well as their impact on the newly growing internal boundary layer caused by the streamwise step-change. The surface heterogeneity was modelled using a similar geometry to X2HS4 case which has a rectangular cross section, made of clear perspex. These ridges extended from the test section inlet over a length of 2.8 m downstream the inlet, before we imposed a step-change to a smooth wall (the step-change distance from the leading edge corresponds to roughly 40δ as shown in figure 3.6 as is where we define the streamwise origin for **Experiment 3**). As in the previous experiment, their nominal heights and spanwise spacings were chosen to be $h = 6$ mm and $S = 80$ mm (to match 0.1 and 1 times δ), respectively, in order to maximise potential secondary flows. As shown in the figure 3.6, cross-plane stereo-PIV and planar-PIV are used both the investigate the cross-stream flow besides the streamwise evolution of the boundary layer at two spanwise locations. Cross-stream stereo-PIV is performed in one plane upstream the step change and three downstream locations past the step change, while planar-PIV was performed at both symmetry planes (peak and valley centres) of the surface heterogeneity. On the other hand, oil-film measurements were performed from the step up to the last stereo-PIV plane, in order to assess the effect of these evolving/decaying large-scale structures on the wall drag. The details about the employed measurement techniques and their settings will be discussed in the sections 3.3.1 and 3.3.3.

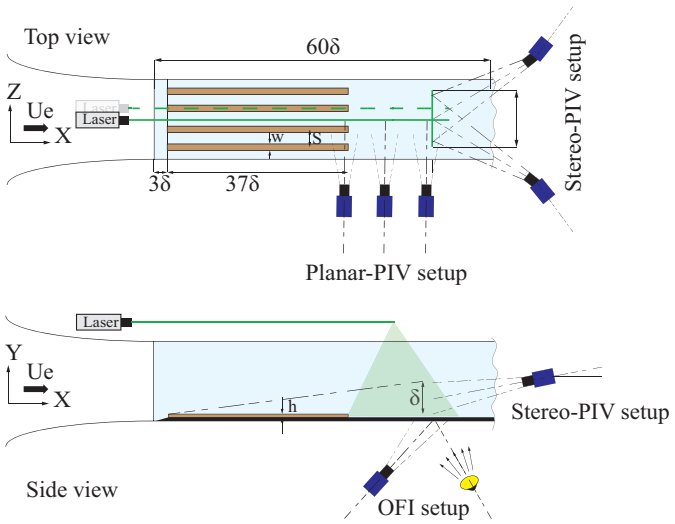

Figure 3.6: Schematics of the experimental arrangement of the surface step-change including the planar/stereo PIV setup (top) and the oil-film interferometry setups (bottom). The planar-PIV was performed at both symmetry plane $z/S = 0$ and 0.5

Case	**OFI**	**HWA**	**PIV**	**Measurement location** (m)
Experiment 1	✓	✓	✗	3.1
Experiment 2	✓	✗	✓	3.2
Experiment 3	✓	✗	✓	2.7–3.3

Table 3.3: Overview of the different experiments and the corresponding experimental techniques used.

3.3 Measurement techniques

3.3.1 Oil-film interferometry

Background

As discussed in the section 2.4, accurate measurements of the skin friction can reveal to be a challenging task in spite of the numerous available methods. Several of these methods are indirect assessment techniques and present several shortcomings as they rely on the measurement of other quantities that require calibrations (e.g. heat transfer or pressure measurements), or simply require flow informations (e.g. mean velocity or Reynolds shear stress profiles). That is the reason why methods that do not require information of the nature of the flow must be privileged when possible. This statement applies for the oil-film interferometric method which is a direct measurement tool for skin friction assessment. Its concept was first introduced by Squire (1961), then Tanner and Blows (1976) applied it to wall shear stress measurement in a flat wall turbulent boundary layer. Ever since, many researchers have tested the applicability of the OFI

technique under several flow conditions. The method has been used in many flows such as: adverse pressure-gradient boundary layers (Pailhas et al., 2009), turbulent boundary layers subjected to free stream turbulence (Blay Esteban et al., 2017) and also in "rough-wall" boundary layers whose surfaces presented a smooth texture (Akomah et al. 2011; Medjnoun et al. 2018, 2020). Many reviews on this technique can be found in the literature, see e.g. Naughton and Sheplak (2002) and Ruedi et al. (2003) and more recently Pailhas et al. (2009). One of the first to have quantified the skin friction was Tanner and Blows (1976) by looking at the thinning rate of the oil, measuring the time evolution of the oil thickness illuminated with a laser beam. They determined the local skin friction using the oil-film equation 3.1. They demonstrated based on the time evolution of the fringe pattern taken from images recorded at equal time intervals, that they were able to get accurate estimates of the skin friction when compared to the predictions from the Clauser chart method. This method is based upon the relationship between the thinning with time of an oil-film deposited on the test surface subjected to a tangential force exerted by the fluid on the wall, which is represented by the local wall shear stress. By assuming a two-dimensional airflow while the pressure gradient, gravity and surface tension terms negligible, Tanner and Blows (1976) showed that the governing differential equation that describes the slow viscous motion of a thin oil sheet is given by

$$-\mu\frac{\partial h}{\partial t} = \frac{\tau_x \partial h^2}{2\partial x}, \tag{3.1}$$

where $h(x,t)$ is the height of the oil-film and μ its dynamic viscosity.

A self-similar solution in time describing the asymptotic behaviour of the thin oil at large time is assumed (Naughton and Brown, 1996). Leading equation 3.1 to

$$h(x,t) = \frac{\mu}{t\sqrt{\tau_x(x)}}\int_{x_0}^{x}\frac{dx}{\sqrt{\tau_x(x)}}. \tag{3.2}$$

With the assumption that the shear stress gradient in the x direction is negligible, relation 3.2 reduces to

$$h(x,t) = \frac{\mu x}{\tau_x t}. \tag{3.3}$$

When the thin oil film is subjected to a monochromatic light source at an incidence angle, a part of the illuminating light is partially reflected by the air/oil interface and the remaining part passes through the film, and reflected by the solid surface then travels back again through the film. These two parts of light (ϕ_1 and ϕ_2) interfere with each other and produce a fringe pattern, with a separating distance which is proportional to the thinning of the oil film height.

The intensity of the resulting wave $(\phi_1 + \phi_2)$ is given by the interference formula

$$I = I_1 + I_2 + 2\sqrt{I_1 I_2}cos(\Phi), \tag{3.4}$$

where I_1 and I_2 represent the intensity of the two interfering waves and Φ the phase difference between ϕ_1 and ϕ_2. Making use of optical interference formulas, a relation for the height of the oil film can be obtained with respect to the phase difference Φ of the light intensity signal obtained from the fringe pattern, and is expressed by

$$h = \frac{\lambda\Phi}{4\pi}\frac{1}{\sqrt{(n_f^2 - n_a^2 sin(\theta_i)^2)}}, \tag{3.5}$$

where λ is the light wavelength, n_f and n_a, respectively, represent the refractive index of oil and air and θ_i the incidence angle of the light. Hence, by knowing the phase difference Φ at any location in the fringe pattern, the height of the oil-film can also be determined, which in turn allows a direct estimate of the wall shear stress.

However, this generally assumes that the oil film thickness varies axially with a monotonic increase from the leading edge of the film, and this cannot be always valid especially for cases where the flow presents three dimensionality. One way to overcome the three dimensionality effect is by assuming a local homogeneity of the flow, by putting oil droplets small enough compared to the flow heterogeneity (Ruedi et al., 2003), by cutting out the region into small elements over which the wall shear stress can be considered as constant. In this case, we get the same interferometric patterns as before, however with a constant step fringe spacing. Replacing the phase Φ in equation 3.5 by the inverse of the frequency of the measured signal (interfringe), we get the equation 3.6

$$\Delta_f = \frac{\lambda x}{2n_0 h}, \tag{3.6}$$

with $n_0 = \sqrt{(n_f^2 - n_a^2 sin(\theta_i)^2)}$. By replacing h by its expression 3.3 in the above relation, it leads to the following formula for the wall shear stress

$$\tau_w = \frac{2n_0 \mu c a}{\lambda}, \tag{3.7}$$

where c is the calibration coefficient (mm/pixel) and a the slope of the interfringe versus time curve (pixels/s). Pailhas et al. (2009) also suggested that in case of three-dimensionality, the implementation of a processing algorithm based upon a rotation of a grid over the fringe pattern, can allow the selection of a line normal to the fringes, enabling to determine its direction as well as magnitude such as

$$\tau_w = \sqrt{\tau_{w_x}^2 + \tau_{w_z}^2}, \tag{3.8}$$

and

$$\theta_{\tau_w} = tan^{-1}\left(\frac{\tau_{w_x}}{\tau_{w_z}}\right). \tag{3.9}$$

The fringe spacing can be extracted from the Fourier transformation applied to the intensity levels provided by the interferometric pattern. As mentioned by Pailhas et al. (2009), a possible weighting of the signal can be used through a Laplace-Gauss window and detecting the position of the characteristic peak in the Fourier space with a least square method in order to find the best Gaussian fit of this local peak, allowing a sub-pixel accuracy for its estimate. Once the fringe spacing is determined for each time step, the curve describing the fringe spacing versus time can be plotted. Then the slope of the best fitted straight line obtained with a least square method, is calculated to extract the wall shear stress value according to formula 3.7, provided that the oil characteristics and the optical calibration coefficients are known a priori.

Set-up description

Oil droplets (Dow Corning 200 Silicone oil) that are approximately 6 mm wide (less than 0.1δ) are deposited at various locations along the spanwise direction. For the first experiment, the droplets are positioned at the bottom glass plate (valley). Above the ridges, a streamwise section of the foam tape (50 mm long) is replaced by a glass plate (and sealed with wax) of the same width and height. The droplets are positioned on top of this glass plate. In the case of the second and third experiments, the droplets were positioned both at the perspex rods as well as the baseline perspex plate for the peaks and valleys respectively, since their surfaces permit optical accessibility. Inside the measurable area of the droplet ($\approx 50\%$ of the droplet area), the statistical uncertainty in C_f is less than 2%. Therefore, these droplets provide independent measurements of skin friction and will enable us to assess the spanwise variation of skin friction.

A sodium lamp with a wavelength of 589 nm is used to illuminate the oil in order to generate the interferograms as illustrated in figure 3.7. In order to capture the OFI images a LaVision Imager LX 16 MPixel CCD camera with a pixel size of 7.4 μm $\times$ 7.4 μm was used. A Nikon 200 mm AF Micro lens was fitted to the camera alongside a Scheimpflug adapter to account for the camera view angle. Using a two-dimensional calibration target as illustrated in figure 3.8 (circular dots with 2.5 mm diameter spaced by 6 mm), the camera coefficients were recovered through a third order polynomial fit. The standard deviation of the polynomial fit for all our measurements was around 1 pixel.

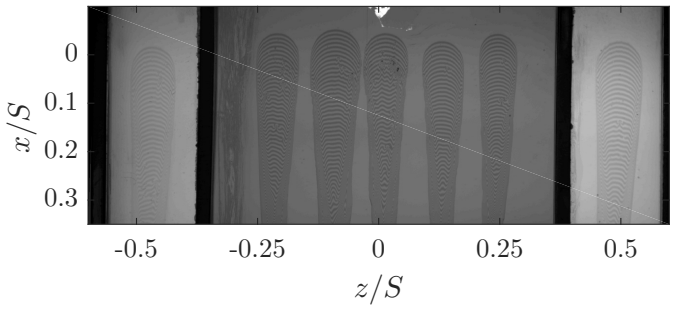

Figure 3.7: Top view of the oil droplets deposited over the smooth and rough part of the surface from the first experiment. Case: X1HS2.

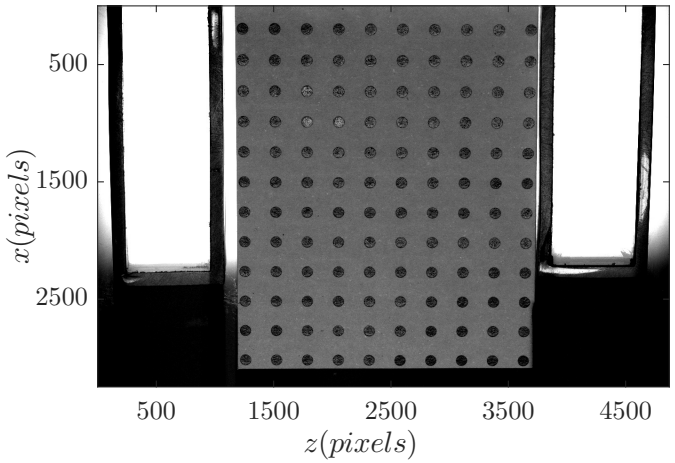

Figure 3.8: Image of the two-dimensional calibration target employed during these experiments. Case: X1HS2.

This resulted in a field of view of 50 mm $\times$ 100 mm in the (x, z)-plane for the first experiment, which was sufficient to capture a full wavelength for X1HS1 and X1HS2, while only a half was available for X1HS3. For the second and third experiments a full wavelength was recorded since the spanwise spacing was set to $S = 80$ mm. For the third experiment, this process was repeated several times at various streamwise locations such that to cover the variation of the skin friction in the non-equilibrium region, and reconstruct a map of the skin friction with the extent of $8S \times 1.2S$ in the (x, z)-plane.

Given the main source of uncertainty in the oil-film interferometry comes from the oil viscosity, it was crucial to calibrate it independently of these experiments. This has been performed for a wide range of temperatures using a DHR 3 TA Instruments rheometer, while monitoring flow temperature during the measurements. Results of the calibration are presented in the figure 3.9, which were collected from four different sets of calibrations. A second order polynomial as well as an exponential function were fitted to the cloud of points in order to obtain an analytical formula that best describes the viscosity variation, to allow for temperature corrections. The results showed that at low temperatures, the fits noticeably deviate from the calibration data. However, within the working range (290–300^o Kelvin), an excellent agreement with the analytical model is

observed. In the present study, the quadratic function was chosen from which a 99% confidence interval is illustrated in the shaded area of the figure 3.9. in order to apply the temperature correction.

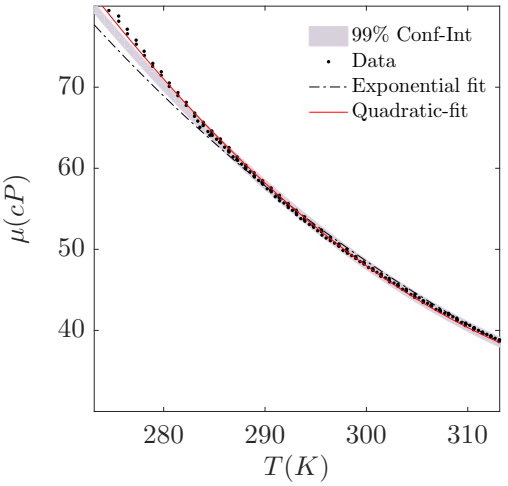

Figure 3.9: Results of the oil-film viscosity calibration from four runs collected using a DHR 3 TA Instruments rheometer. A confidence interval of 99% is presented along the raw data as well as two different fitting functions; (black dot-dashed line) exponential and (red solid line) quadratic fits. The calibration was performed for a range of 270^o–320^o Kelvin.

A series of 100 interferograms per spacing and speed are acquired for approximately 10 minutes in each run using LaVision DAVIS 8.2. The interferograms are then post-processed using a similar method described by Blay Esteban et al. (2017). The light intensity of the pattern extracted from the interferogram resembles a sine wave with a Gaussian noise due to the non-uniformity of the light illumination. A two-step process is used in order to determine the wall shear stress. First, the peaks and valleys of this wavy signal that represent the constructive and destructive interferences of the reflected light waves are identified using a Fast-Fourier Transform. A second estimation of the fringe spacing was made by first filtering the signal using the Savitzky-Golay smoothing filter. This filtering process uses n (n varies depending the length of the signal) points around the point that is being filtered to fit a polynomial of order $m = 4$. Savitzky-Golay filters are optimal for smoothing the signal by minimizing the least-squares error in fitting a polynomial to each frame of noisy data. In order to have a sub-pixel accuracy on the fringe spacing, a Fourier sinewave signal is fitted to the filtered signal. Once the frequency of the signal is obtained with sub-pixel accuracy, the fringe spacing is computed as well, then plotted against time. The wall shear stress is then determined using equation 3.7. This process is repeated for several spanwise locations, hence enables the description of the drag variation in the spanwise direction as shown in figure 3.10. Our current results showed a relative uncertainty in the skin friction coefficient based on the smooth wall correlation of Nagib et al. (2007) less than 2.5%. A summary of

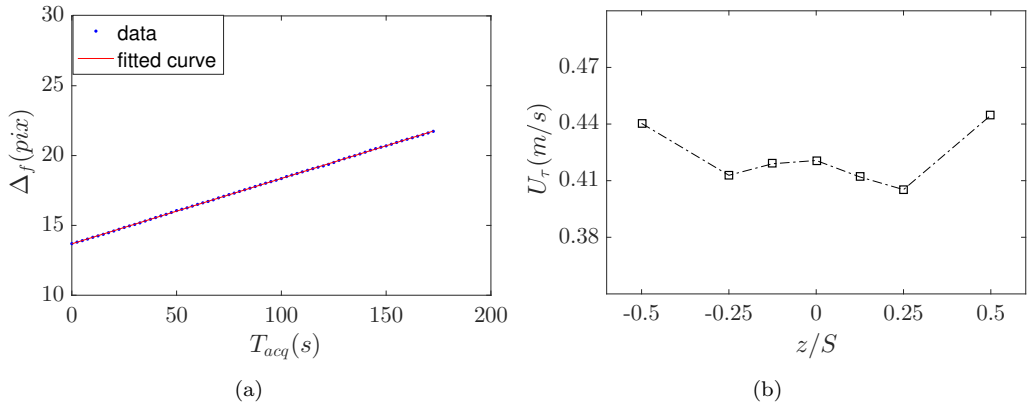

(a) (b)

Figure 3.10: (a) Example of a time evolution of the fringe spacing at one of the spanwise locations and (b) estimation of the friction velocity using the described procedure at different spanwise locations with $U_\infty = 10$ m/s from the first experiment. Case: X1HS2.

the number of samples N, acquisition frequency F_a, duration T_{acq} and measurement locations are provided in the table 3.4 below.

Case	N **samples**	F_a (Hz)	T_{acq} (s)	x**-location** (m)
Experiment 1	100	0.5–1	100–200	3.1
Experiment 2	100	0.5–1	100–200	3.2
Experiment 3	100	0.5	200	2.7–3.3

Table 3.4: Overview of the different settings of the oil-film interferometry for the different experiments.

3.3.2 Hot-wire anemometry

Background

One of the most well-established techniques yet always present amongst the experimental fluid dynamics community is the hot-wire anemometry technique (Orlu and Vinuesa, 2017). It is used to measure the instantaneous velocities of fluid flows based on the sensor heat transfer by the fluid surrounding it (moving air around the sensor). The sensor in the hot-wire anemometer is either a thin metal wire or a film (wall shear stress probes) made of a material with a high temperature coefficient of resistance, generally tungsten (used throughout these experiments) or platinum. The wire is constantly heated by an electric current and the flow velocity is obtained by the heat convected from the sensor as it operates. The sensor is connected to one of the arms of a Wheatstone bridge, the opposite arm being connected to a variable resistance controlling the overheat ratio, defined as,

$$a_w = \frac{R_w - R_a}{R_a}, \tag{3.10}$$

where R_w is the sensor resistance when heated and R_a is the sensor unheated resistance. Typical values of a_w for air measurements range from 0.05 to 1.0.

The system can be operated in three different modes: constant current anemometer (CCA) maintains the current constant and measure changes in the resistance of the wire, constant temperature anemometer (CTA) keeps the resistance of the wire constant and measures the change in current and constant voltage anemometer (CVA) which keeps the voltage constant and measures the changes in current.

Set-up description

Hot-wire anemometry measurements were conducted for the first experiment. To this end, an Auspex A55P05 single hot-wire boundary layer type probe is used in order to measure the time series of the streamwise velocity at different wall-normal locations, to determine the statistical characteristics of the flow. The probe is also traversed in the spanwise direction in order to obtain additional information due to the heterogeneity of the flow herein studied. As shown in figure 3.11, these stations are represented by P, M and V which refer to the peak, mid-peak-valley and valley locations, coinciding respectively with the spanwise-normalised distance $z/S = 0.5$, 0.25 and 0. For X1HS1 spacing case, the profiles were only acquired at P and V locations.

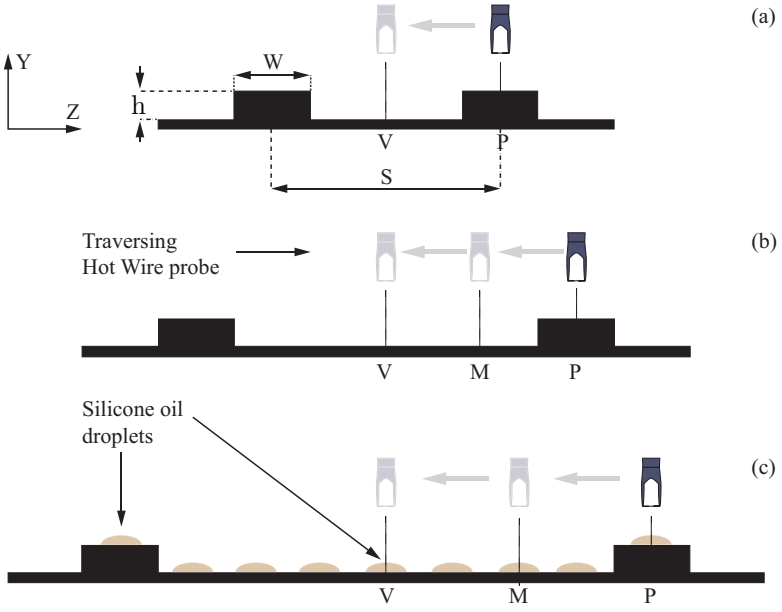

Figure 3.11: Schematics of the three spacings investigated in the first measurement campaign with, (a): X1HS1 $\frac{S}{\delta_{av}} \approx 0.8$, (b): X1HS2 $\frac{S}{\delta_{av}} \approx 1.7$ and (c): X1HS3 $\frac{S}{\delta_{av}} \approx 3.2$. The spanwise reference points V, M and P are representative of the valley, mid-valley-peak and the peak locations, respectively.

The single wire probe had a 10 mm long prongs spanned by a 3 mm long and 5 μm diameter tungsten wire with a sensing length of about 1 mm, bounded on either sides by copper-plated sections. The resulting length-to-diameter ratio of the probe is 200 which follows the recommendation of Hutchins et al. (2009). A DANTEC Streamline Pro CTA system was used and operated at fixed overheat ratio a_w= 0.8. The turbulent boundary layer profiles consisted of 42 wall-normal locations, each of which had an acquisition time of 3 to 5 minutes with a sampling rate of 25 to 70 kHz and low-pass filtered at 10 kHz to 30 kHz depending on the free stream velocity. The latter allows to remove the high frequencies due to noise and prevent aliasing (Nyquist criterion) while the former is in order to obtain converged mean, turbulence intensity and spectra. The output was recorded by a 16-bit National Instruments USB-6212 BNC, A/D data acquisition board. Similarly, the free stream velocity as well as the temperature were recorded throughout the measurement, using a Pitot-static probe connected to a Furness FCO510 transducer and a T-type Omega thermocouple respectively. Before recording, the signal was conditioned by optimising the gain and removing its offset while a temperature correction was also applied.

A wall-normal velocity profile is measured at several locations using an automated traverse system. The traverse is a stepper motor based, with two servo-motors that allow two degrees of freedom both in the spanwise and wall-normal directions. The motors were controlled through a MATLAB software, which is included in the acquisition software. As the facility is a suction type wind tunnel, any hole or perforation on the wall can act as an additional source of momentum which in turn can perturb the base flow leading to inaccuracies. Therefore, these sources were duct-taped every time a station was changed.

Before the measurements, preliminary tests were carried out to assess the time necessary to converge the second order moment, and to estimate the boundary layer thickness, so we can base the roughness spacing on the scale of a boundary layer thickness. Similarly, in order to measure and converge the spectra, we first needed to have an idea of the highest frequency in the flow. Based on the estimations of the boundary layer thickness, we measured the spectra within the log region, at around 15% of δ, and the cut-off and sampling frequencies F_c and F_s respectively were chosen according to the estimation of the measured spectra. The preliminary tests are presented in the table 3.5, where τ and τ_{eddy} are the eddy turn over time and the number of the cycles of the largest scale in the flow respectively.

U_∞ (m/s)	δ (mm)	τ (ms)	T_{acq} (s)	τ_{eddy}	F_c (kHz)	F_s (kHz)
10	50	5.0	300	6×10^4	10	30
15	47	3.13	250	8×10^4	30	75
20	44	2.2	200	9×10^4	30	75
25	42	1.68	150	9×10^4	30	75

Table 3.5: Preliminary test of the hot-wire measurements for **Experiment 1**.

A microscope camera was used in order to assess the wire location relative to the wall. The procedure consists of traversing the wire down close to the wall, and using the microscope camera, the reflection of the wire starts being observed at the wall. This can be achieved by putting a light source above the wire location. Two successive images were then captured at two different locations from the wall, with a known displacement, as shown in the figure 3.12. Overlaying the two images using any image processing

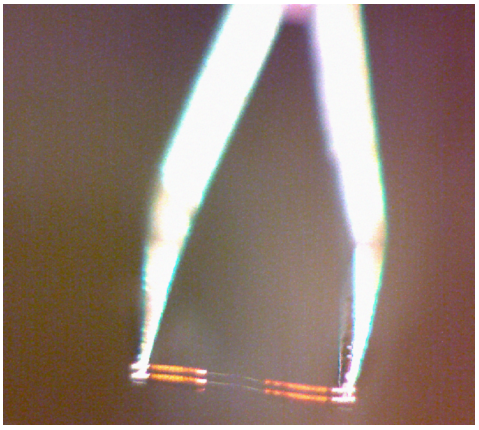

Figure 3.12: Hot-wire wall location determination using a microscope camera.

software would allow the determination of the current wire location with respect to the wall by simply converting the pixels to millimetres. A note concerning monitoring the hot-wire near the wall. When operating at high velocities two main constraints were observed. The first one being the shedding of the wake behind the traverse arm which leads to vibrations on the traverse arm, which in turn effects the stability of the probe. The second one is the force acting on the arm generating a lift force observed to subtly change the actual wire location from the wall, resulting in biases regarding the wire location of the order of 0.2 - 0.5 mm (depending on the wind speed). These offsets were accounted for in the post-processing of the velocity profiles.

Hot-Wire calibration

The output signal of a hot-wire measurement is a voltage signal; so a calibration procedure of the voltages against known velocities must be performed. This calibration procedure involves the determination of a relationship between the output voltage E of the wire and the velocity which is usually given by a Pitot static probe measured in the free stream U_∞, the sensor is then exposed to a range of velocities. The relationship given by King$'$s law (King, 1914)

$$E^2 = A + BU^n, \tag{3.11}$$

with n varying between 0.39 - 0.45, is then fitted to the calibration points.

Temperature variations that might occur during the experiment are recorded to correct the sensor voltage output before the velocity conversion. Regarding temperature corrections, a linear formula is typically applied as proposed by Abdel-Rahman et al. (1987) as

$$E_{cor} = E_{meas} \times \xi, \tag{3.12}$$

with

$$\xi = \sqrt{\frac{T_w - T_{ref}}{T_w - T_a}}, \tag{3.13}$$

where T_w the wire temperature, T_{ref} the temperature of the wire during the calibration (assumed to be constant for CTA system) and the ambient temperature T_a.

As we need to vary the Reynolds number in our investigation, different calibrations were required to cover the range of velocities. The hot-wire is calibrated using a 20-point curve, calibration velocities ranging from 3 m/s to 30 m/s for the 15, 20 and 25 m/s cases, and 1.5 m/s to 15 m/s for the 10 m/s case. The reference velocity for the calibration was obtained using a Pitot static probe connected to a Furness FCO510 manometer. King$'$s law is then applied in order to convert the raw data to velocity. Temperature during the calibration and the experiment was recorded using a thermocouple in order to apply temperature corrections of the measurements as explained in the previous paragraph. Hultmark and Smits (2010) proposed a method for temperature drift corrections based on a knowledge of a single calibration, however this method does not account for variations in ambient pressure and humidity changes in the surrounding of the hot-wire probe. To overcome this change of the ambient conditions, pre- and post-calibrations are performed on a set of measurements, to account for this bias error. A linear interpolation method (based on time) is used in order to correct for the drift in temperature in each point of the profile as shown in the figure 3.13. The results highlight a slight difference between both the pre- and post-calibration, whilst the temperature changes during the calibrations are shown to weakly change.

The major contributions of uncertainties in hot-wire measurements come essentially from the calibration error, temperature and electrical drifts as well as ambient pressure changes, which make up 1–2% the overall uncertainty (Tropea and Foss, 2007; Orlu and Vinuesa, 2017). These are presently accounted for partially through these simultaneous measurement of the temperature and interpolation between pre- and post-calibration mentioned above.

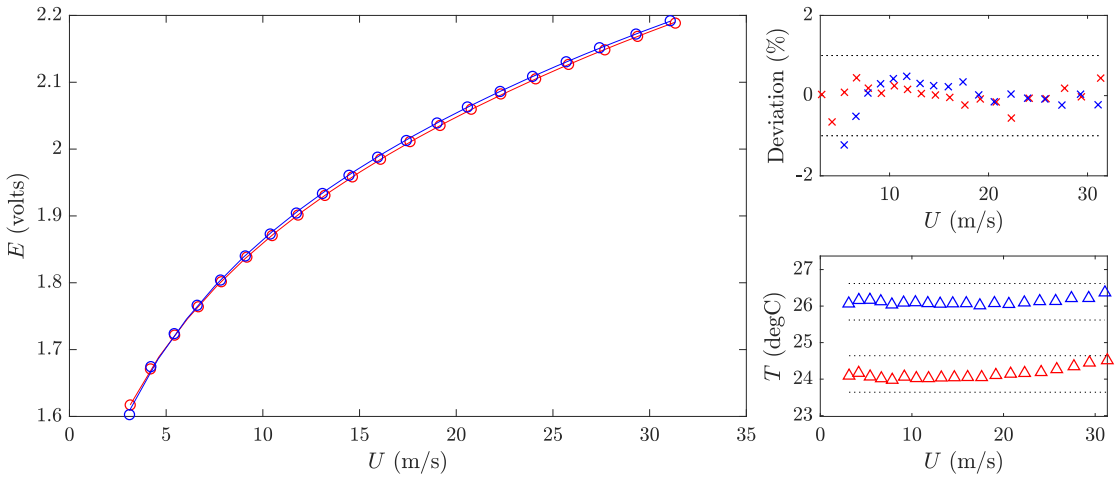

Figure 3.13: Hot-wire probe calibrations. the blue and red colours are for the pre- and post-calibrations respectively. Left: circles represent calibration data and the curves are their respective King's Law fits. Top right: average temperature deviation during the calibration procedure shown to be less than 0.5%. Bottom right: evolution of the average temperature for the range of speeds for the calibrations.

3.3.3 Particle Image Velocimetry

Background

Particle image velocimetry compared to hot-wire anemometry and other single-point measurement techniques offers the advantage of providing global field assessment of instantaneous velocity fields, whether planar or volumetric. In this prospect, it provides the advantage of being a flow visualization as well as a flow diagnostic technique. The working principle of this technique essentially requires an optically transparent test section, particles or tracers which are assumed to follow the flow, a light source generally being monochromatic lasers to illuminate the region of interest and a recording device that consists of a camera. When the particles are illuminated, a light scattering is formed and captured by the camera sensors. The particle coordinates on the image plane are converted to physical coordinates in the object plane through a mapping function. The images are then processed in pairs. The flow trajectories are inferred by interrogating smaller sized windows that contain packets of particles. In order to have a representative estimate of the local velocity, each window should typically have 15 particles on average that move coherently, with a particle size of 2–3 pixels. Interrogation windows are assigned coordinates and are cross-correlated with the windows from the second image, having similar coordinates. This results in a correlation map inside the interrogation window, with generally one main lobe representative of the average particle displacement. This process is repeated for all the interrogation windows within one image pair, hence leading to a map of particle displacements, which are then converted to velocity field, provided that a time delay between two successive images is known.

PIV has become a widely used technique in the fluid mechanics community in general, more specifically within the turbulence research field, in order to describe and understand its flow physics. The theory an applications of PIV have been extensively reviewed by many researchers. For a detailed review of this technique, the reader can refer to the work of Adrian and Westerweel (2011).

Setup description for 2D2C-PIV

In order to investigate the development of the secondary flows past a heterogeneous-to-homogeneous step-change (**Experiment 3**), planar (2D2C) PIV is employed to capture the flow field evolution downstream the surface discontinuity. The measurements are acquired in the (x, y)-plane between 2.4–3.4 m downstream the leading edge. The flow is seeded with vaporised glycol-water solution tracers ($\approx 1\mu m$ in diameter) illuminated with a laser light sheet sourced by two 2-pulse Litron Nd:YAG laser systems operating at 200 and 250 mJ each, in order to get an extended field of view (FOV). The time difference between two pulses of each source was set such that to maximize the pixel displacement of the particles. A LaVision optical system for the beam focus/expansion of the light sheet is used, which comprises of two spherical lenses; a +50 convex and +100 concave in order to focus the beams, and a concave cylindrical lens with a focal length of +10 mm in order to get a wide expanded light sheet of about 1.5 mm thickness. Two spanwise locations are chosen in order to investigate the flow evolution. As shown in figure 3.6, the streamwise-wall-normal (x, y)-planes are acquired at the two spanwise symmetry planes $z/S = 0$ and $z/S = 0.5$ (valley and peak respectively). Three 16 Megapixel resolution cameras equipped with Sigma 105 mm lenses used in order to get a wide FOV, with a distance of the image-to-object plane being around 1 m. With the given setup, the resulting FOV was approximately $10\delta \times 2\delta$ in the (x, y)-plane (from -δ upstream the step-change to 9δ downstream). In order to obtain statistically independent realizations, image pairs are acquired at 0.3 Hz. A total of 2000 samples were necessary in order to converge at least the first order moments. The acquisition is performed through Davis 8.3 and the raw images are preprocessed in ordered to minimize the background noise by the removal of minimum light intensity with a kernel size of 5 × 5 pixels. The particle images are subsequently interrogated using a decreasing multipass scheme starting from a window of 48 × 48 to a final pass of 16 × 16 with a 50% overlap between the interrogated windows. This resulted in an effective spatial resolution of approximately 0.45 mm × 0.45 mm.

Setup description for stereo-PIV

Following the observations from previous studies, potential secondary flows are expected to generate a large-scale modification of the turbulent boundary layer leading

to strong spanwise heterogeneities. For the second experiment, the cross-plane (y, z) is investigated using stereo-PIV measurements performed at a streamwise location similar to that of the OFI measurements ($x = 3.2$ m downstream the leading edge) as described in the setup illustrated in figure 3.14. Similarly to the planar-PIV, the flow is traced by vaporised glycerol-water solution particles generated by a Magnum 1200 fog machine, then illuminated with a laser light sheet sourced by a two-pulse Litron Nd:YAG laser operating at 200 mJ. A LaVision optical system for the beam focus/expansion of the light sheet is used, which comprised of convex and concave lenses in order to focus the beam, and a cylindrical lens in order to expand the sheet with relatively constant thickness in the measurement plane (≈ 1.5 mm thickness). The particle images are recorded by two high-resolution LaVision Imager LX 16 MP CCD cameras fitted with a Nikon 200 mm AF Micro lens each and mounted on Scheimpflug adapters to account for the oblique view angle ($\pm 42°$), and are placed at nearly 1 m from the object plane. A double-sided dual plane calibration target aligned with the laser light sheet was used to determine the mapping function for each camera, using a third-order polynomial fit. This resulted in a FOV of approximately $2\delta \times 3\delta$ in the (y, z)-plane. Using LaVision's DaVis 8.3 software, 3000 statistically independent realizations of image pairs are acquired for each case at 0.6 Hz, with a time delay between two pulses of 20 µs at a free stream velocity $U_\infty = 20\,\mathrm{m\,s^{-1}}$. This resulted in an average displacement of 7–8 pixels, amounting to approximately 1.5% bias uncertainty in the measurement (given the sub-pixel uncertainty being around ± 0.1 pixels). The velocity vector fields were subsequently obtained by interrogating particle images using a decreasing multipass scheme starting from window sizes of 48 pixels $\times$ 48 pixels to a final pass at 24 pixels $\times$ 24 pixels with 50% overlap. The resulting vector fields were subsequently low-pass filtered at $l^+_{SPIV} \approx 55$ (with l^+_{SPIV} being the inner-normalised interrogation window size of the SPIV grid). This prevents the comparison between cases to be affected by the grid resolution due to marginal differences in Re_τ. This procedure was subsequently repeated for the third experiment, in order to cover the streamwise evolution of the boundary layer past the step-chang. Four stations are acquired similarly at: -0.6δ, 0.25δ, 4δ and 8δ past the step-change. The image pairs are processed in Davis with a cross-correlation stereo PIV scheme, using a similar protocol as the one used for the second experiment. The table 3.6 summarises the main settings and the resulting parameters of the planar- and stereoscopic-PIV experiments.

Many factors can contribute to the overall uncertainty in the measurement, both statistical as well as systematic. The leading order uncertainties for planar-PIV are the pixel size which introduces what is called pixel-locking (or peak-locking). This is essentially encountered when the particle images are not sufficiently bigger than a single pixel, leading to the particles being "locked" at a given integer value, while its subpixel accuracy becomes unknown. This is compensated for by defocusing the cameras slightly for the planar-PIV while this issue was less important for stereo-PIV since the particle sizes were between 2 and 3 pixels. The second source of error comes from the

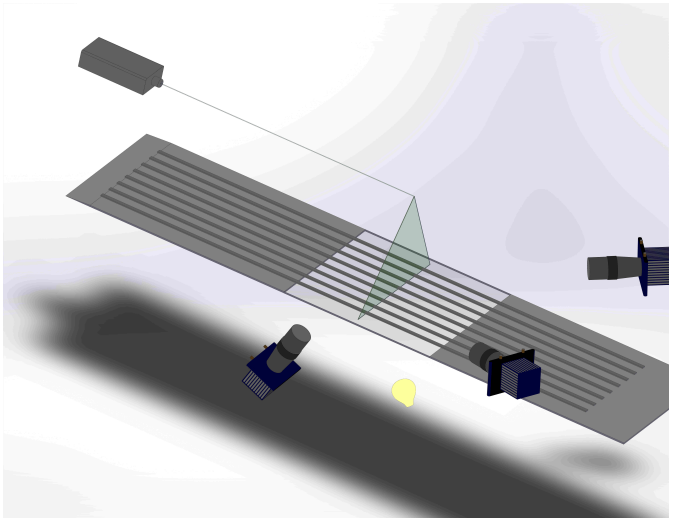

Figure 3.14: Perspective view of a generic experimental stereo-PIV and oil-film setup used in the second and third measurement campaigns.

misalignment of the calibration plate to the laser light sheet in the stereo-PIV setup. To this end, a procedure based on the computation of the disparity map as described by Wieneke (2005) is applied to the datasets. This self-calibration corrects for the coefficients of the third order polynomial, leading to considerably reduced biased vector fields.

Parameters	**Planar**	**Stereo**
FOV	(x, y) $10\delta \times 2\delta$	(z, y) $3\delta \times 2\delta$
First pass IW size	48 pixels × 48 pixels	64 pixels × 64 pixels
Final pass IW size	16 pixels × 16 pixels	24 pixels × 24 pixels
Laser pulse delay	50 μs	20 μs
Average pixel displacement	15 pixels	7–8 pixels
Acquisition frequency	0.3 Hz	0.6 Hz
Spatial resolution	0.95 mm	1.1 mm
Effective resolution	0.475–0.5	0.50–0.55
Number of samples	2000	2500-3000
Laser power (1 and 2)	200 and 250 mJ	200 mJ
Laser optics	(-50,+100) and -10 mm	(-50,+100) and -50 mm
Number of cameras	3	2
Camera resolution	16 Megapixel	16 Megapixel
Camera pitch size	7.4 μm	7.4 μm
$f_\#$	4	4
Camera lens	Sigma 105 mm	Nikon 200 mm
Camera angle	0	38°–42°

Table 3.6: Parameters of the planar and stereoscopic particle image velocimetry experiments conducted in the second and third measurement campaigns.

3.3.4 Measurement uncertainty

Despite the attention paid during the experimental setup and data acquisition procedures, measurements will still be tainted by a degree of uncertainty due to various sources of errors. These uncertainties are generally divided into two groups. They can be caused by systematic errors and depend on the accuracy of the measurement technique (limited by the technology being employed). They can also be attributed to random errors which depend on precision of the measured quantity (limited by the number of samples available e.g. repeatability). In this section, we try to quantify the main sources of errors that contribute to the uncertainty in the oil-film interferometry, hot-wire anemometry as well as the particle image velocimetry measurements.

Oil-film interferometry

The wall-shear stress is determined using equation 3.7. Hence, the uncertainty on τ_w depends on the optical characteristics of the test surface, oil viscosity, the camera calibration coefficient, the fringe spacing as well as the light wavelength used to illuminate the oil. Assuming the constituent variables of τ_w are uncorrelated between each other, a linear uncertainty propagation yields

$$\epsilon_{\tau_w} = \sqrt{\left(\frac{\partial \tau_w}{\partial n_0}\epsilon_{n_0}\right)^2 + \left(\frac{\partial \tau_w}{\partial \mu}\epsilon_{\mu}\right)^2 + \left(\frac{\partial \tau_w}{\partial c}\epsilon_{c}\right)^2 + \left(\frac{\partial \tau_w}{\partial a}\epsilon_{a}\right)^2 + \left(\frac{\partial \tau_w}{\partial \lambda}\epsilon_{\lambda}\right)^2} \tag{3.14}$$

In order to estimate the sensitivity terms (partial derivative terms), equation 3.7 is derived with respect to each variable. This results in the following relations whose quantities are readily available

$$\begin{cases} \frac{\partial \tau_w}{\partial n_0} = \frac{2\mu c a}{\lambda} = \frac{\tau_w}{n_0} \\ \frac{\partial \tau_w}{\partial \mu} = \frac{2 n_0 c a}{\lambda} = \frac{\tau_w}{\mu} \\ \frac{\partial \tau_w}{\partial c} = \frac{2 n_0 \mu a}{\lambda} = \frac{\tau_w}{c} \\ \frac{\partial \tau_w}{\partial a} = \frac{2 n_0 \mu c}{\lambda} = \frac{\tau_w}{a} \\ \frac{\partial \tau_w}{\partial \lambda} = -\frac{2 n_0 \mu c a}{\lambda^2} = -\frac{\tau_w}{\lambda} \end{cases}$$

The uncertainty on each variable in also quantified as follow. For ϵ_{n_0}, an additional linear uncertainty propagation was needed since this quantity is function of n_f, n_a and θ. The former two quantities are function of pressure, humidity and temperature. For typical working conditions in the laboratory, these have been quantified, and their uncertainty is estimated from the variation of the temperature throughout the measurement (since the humidity and atmospheric pressure remain constant within the acquisition). The uncertainty in θ is given by the resolution of electronic level used. The uncertainty in the light wavelength λ was also estimated from the variation of temperature, while the camera calibration coefficient is tainted by both the uncertainties from the third order

polynomial fit as well as the uncertainty arising from the calibration target itself. The last additional sources of uncertainties stem from the oil viscosity calibration and the fringe spacing fits. For the latter quantities, ϵ_μ and ϵ_a were assessed from the uncertainty in the fitting coefficients with 95% confidence bounds. This produced an uncertainty of about 2.35% in τ_w as illustrated in the table 3.7

Source	Relative uncertainty (%)
Optical characteristics n_0	0.03
Oil viscosity	2.21
fringe spacing	0.71
Camera calibration	0.39
Light wavelength	0.10
Total (ϵ_{τ_w})	2.35

Table 3.7: Uncertainty budget on the wall shear stress τ_w estimated for a representative case with a freestream velocity of $U_\infty = 20$ m/s.

Once the uncertainty on the wall shear stress is determined, we further estimate the errors that propagate into the skin-friction coefficient based on the equation

$$C_f = \frac{2\tau_w}{\rho U_\infty^2}, \tag{3.15}$$

Following the same linear uncertainty propagation approach on equation 3.15, we obtain the following

$$\epsilon_{C_f} = \sqrt{\left(\frac{\partial C_f}{\partial \tau_w}\epsilon_{\tau_w}\right)^2 + \left(\frac{\partial C_f}{\partial \rho}\epsilon_\rho\right)^2 + \left(\frac{\partial C_f}{\partial U_\infty}\epsilon_{U_\infty}\right)^2 + \left(\epsilon_{C_{f_{stat}}}\right)^2} \tag{3.16}$$

This can be expressed through the following relations as before

$$\begin{cases} \frac{\partial C_f}{\partial \tau_w} = \frac{2}{\rho U_\infty^2} = \frac{C_f}{\tau_w} \\ \frac{\partial C_f}{\partial \rho} = -\frac{2\tau_w}{\rho^2 U_\infty^2} = -\frac{C_f}{\rho} \\ \frac{\partial C_f}{\partial U_\infty} = -\frac{4\tau_w}{\rho U_\infty^3} = -\frac{2C_f}{U_\infty} \end{cases}$$

The error corresponding to each of the sensitivity terms are also quantified with ϵ_{τ_w} already provided above. The uncertainty in the air density ϵ_ρ is determined from the temperature variation throughout the measurement (1.96 $\times$ the standard deviation around the mean for a confidence interval of 95%) as well from an uncertainty due to the resolution of the sensor (0.1^o). On the other hand, an additional linear uncertainty propagation had to be carried out for ϵ_{U_∞}, since it is both function of dynamic pressure estimated from a Pitot-static tube and the air density, this in an addition to a statistical uncertainty on U_∞. Finally the statistical error in C_f was estimated by measuring the quantity at different slices within a single oil droplet (within the measurable area), and assuming the variation around the mean of the values are normally distributed (Gaussian distribution).

Type	Relative uncertainty (%)
Systematic	2.42
Statistical	1.1
Total (ϵ_{C_f})	2.66

Table 3.8: Uncertainty budget on the skin-friction coefficient C_f estimated for an average case with a freestream velocity of $U_\infty = 20$ m/s, with a statistical uncertainty quantified for a 95% confidence interval.

The overall uncertainty in C_f is shown to reach 2.66% as shown in the table 3.8. The results clearly indicate that the leading source of error in the OFI measurements arise from the uncertainty in the oil viscosity, followed by the error in determining the fringe spacing (sub-pixel accuracy).

Hot-wire anemometry

Uncertainties in hot-wire anemometry measurements arise from several sources. According to Orlu and Vinuesa (2017), the main sources are associated with the calibration, linearisation and the drifts in temperature. The latter additionally induces variations in air density as it is a function of both temperature and atmospheric pressure. In order to assess the different sources of errors, equation 3.11 is rearranged as

$$U = \frac{1}{B^2}\left(\frac{E^2}{R_w(R_w - R_a)} - A\right)^m, \tag{3.17}$$

with the power m generally equal to 2, $A = 0.39\frac{\pi l k_a}{\chi R_{ref}}$, $B = 0.51\frac{\pi l k_a}{\chi R_{ref}}\left[\frac{\rho_a d}{\mu_a}\right]^{0.5}$, $R_w = R_{ref}\left[1 + \chi(T_w - T_{ref})\right]$ and $R_a = R_{ref}\left[1 + \chi(T_a - T_{ref})\right]$. The variables l and d being respectively the sensing length and diameter of the hot-wire sensor, χ and k_a being the temperature coefficient of the wire resistivity around the reference temperature T_{ref} and thermal conductivity at ambient temperature respectively. ρ_a and μ_a are the ambient air density and dynamic viscosity respectively. Applying a linear uncertainty propagation to equation 3.17 results in the following sensitivity relations

$$\begin{cases} \frac{\partial U}{\partial E} = \frac{4}{E}\left(1 + \frac{A}{B\sqrt{U}}\right) \\ \frac{\partial U}{\partial T_a} = \frac{2}{T_w - T_a}\left(1 + \frac{A}{B\sqrt{U}}\right) \\ \frac{\partial U}{\partial \rho_a} = -\frac{U}{\rho_a}, \text{ with } \frac{\partial \rho_a}{\partial T_a} = -\frac{\rho_a}{T_a} \text{ and } \frac{\partial \rho_a}{\partial P_a} = \frac{\rho_a}{P_a} \text{ assuming } (A, B) \text{ being constant} \\ \frac{\partial U}{\partial \mu_a} = \frac{U}{\mu_a}, \text{ with } \frac{\partial \mu_a}{\partial T_a} = \frac{\mu_a}{2}\left(\frac{T_a + 360}{T_a(T_a + 120)}\right) \end{cases}$$

This shows that the uncertainty in the hot-wire velocity measurements depends on the electrical drift, temperature drift as well as changes in the viscosity and air density. The overall uncertainty in the velocity U can therefore be written as

$$\epsilon_U = \sqrt{\left(\frac{\partial U}{\partial E}\epsilon_E\right)^2 + \left(\frac{\partial U}{\partial T_a}\epsilon_{T_a}\right)^2 + \left(\frac{\partial U}{\partial \rho_a}\epsilon_{\rho_a}\right)^2 + \left(\frac{\partial U}{\partial \mu_a}\epsilon_{\mu_a}\right)^2 + (\epsilon_{fit})^2 + \left(\epsilon_{U_{ref}}\right)^2} \tag{3.18}$$

The uncertainty in the voltage ϵ_E can be estimated from the pre- and post-calibration. The uncertainties in temperature, density and viscosity are estimated in the same way as previously done for the OFI. Additionally, the uncertainty in the fitting coefficients and the reference velocity (calibrator) add up to the overall measurement uncertainty. The latter is based on Bernoulli's relation: $U = \sqrt{\frac{2\Delta P}{\rho}}$, for which an additional linear uncertainty propagation is carried out. Using data from a representative measurement at $U = 20$ m/s, the relative contributions of the different sources of error can be computed. The resulting uncertainty budget for the hot-wire measurement is given in the table 3.9, highlighting the leading source of error to be the reference velocity which amounts to roughly 1%, followed by the uncertainty in the fitting and changes in the atmospheric conditions. The variations in the electrical drift are shown to be relatively small in comparison with the overall uncertainty, found to be $\epsilon_U \approx 1.3\%$. It is worth mentioning that the statistical uncertainties in the hot-wire measurements are relatively small. The maximum relative uncertainty in the mean (estimated from the near wall region) is approximately 0.1%, whereas the error in the variance is 0.66%.

Source	Relative uncertainty (%)
Fit	0.44
Calibrator	1.03
Electric drift	0.13
Temperature drift	0.7
Density and viscosity changes	0.32
Statistical	0.11
Total (ϵ_U)	1.3

Table 3.9: Uncertainty budget on the velocity U estimated for a representative case with a freestream velocity of $U_\infty = 20$ m/s.

Particle image velocimetry

Uncertainty quantification of PIV measurements can be a daunting task due to the numerous sources of errors present throughout the process. There are many works that reviewed the uncertainty in PIV measurements (see e.g. Adrian 2005; Sciacchitano et al. 2015; Wieneke 2017). According to these studies, many hidden factors aside from the PIV correlation algorithms used can influence the overall accuracy of the measurements. These can arise due to synchronisation between lasers and cameras, perspective errors, misalignment between the light sheet and calibration target, particle size leading to pixel

locking, camera sensor noise, inhomogeneous seeding density, variations in light intensity and out-of-plane motion among others. The discussion of these different aspects will not be addressed as it is beyond the objective of the present study. However, an estimation of the bias error in the accuracy of the particle locations of the order of 0.1 pixels is used as reference, following the study of Sciacchitano et al. (2015). It was shown that most of the PIV algorithms perform to within an accuracy of $\pm 0.05\%$. This means that for an average particle displacement of 7–8 pixels as in this study (throughout the FOV), the uncertainty in the particle displacement, hence, in velocity is roughly 1–1.5%. Additionally, due to the limited number of samples, the statistical error can also contribute to the uncertainty in the mean and turbulence quantities. Using the method outlined by Benedict and Gould (1996) and considering a confidence interval of 95%, the statistical uncertainty in the mean velocity across all cases is found to be less than 0.7%, while the uncertainty in the variance is approximately 4%.

4. Charateristics of turbulent boundary layers over smooth surfaces with spanwise heterogeneities

4.1 Introduction

In this chapter, a turbulent boundary layer flow developing over a heterogeneous surfaces is experimental investigated to examine the mean flow and turbulence characteristics, and to document the variation of skin-friction that might affect the applicability of traditional scaling and similarity laws. The heterogeneity is imposed along the spanwise direction and consists of streamwise-aligned smooth raised ridges whose spanwise spacing S is is varied between 0.8δ to 3.2δ. Single-point velocity measurements alongside direct skin-friction measurements are used to examine the validity of Townsends similarity hypothesis. The experimental arrangement for this study is described in the section 3.2.1. Parts of this chapter have been published in Medjnoun et al. (2018).

4.2 The mean surface shear stress

A critical part of the analysis of a turbulent boundary layer is the accurate assessment of the friction velocity, since most of the analysis is based upon this quantity. The following results from the OFI method describe the response of the surface shear stress to the presence of a surface heterogeneity. Figure 4.1 shows the spanwise distribution of the local skin-friction coefficient for the different spacings at two Reynolds numbers ($Re_x = U_\infty x/\nu$ where x is the distance to the measurement location from leading edge) obtained for two different free stream velocities. As expected for a higher Reynolds number, the skin-friction coefficient is lower. At low Reynolds number, the values of C_f for the X1HS1 and X1HS2 surfaces are greater than the smooth wall value with the

X1HS1 surface producing the most viscous drag. Interestingly, the measurements of the X1HS3 surface indicate a potential drag reduction within the valley. The variation of $C_f(z)$ across the span differs significantly due to the surface heterogeneity. This result can be interpreted as a consequence of a global change in the mean flow due to the presence of secondary flows (as observed by Vanderwel and Ganapathisubramani 2015), which in turn leads to local modifications of the skin friction. From figure 4.1, we observe that the skin-friction coefficient is higher on the elevated region of the surface compared to the rest of the valley area. This indicates that the mean velocity gradient at the wall dU/dy is higher at the elevated surface compared to the valley, which is a result of the reorganisation of the turbulent boundary layer structure across the cross-plane. As reported by Vanderwel and Ganapathisubramani (2015), the secondary flows create HMPs in the valleys and LMPs along the elevated region of the surface. This in turn leads to the spatial heterogeneity in the skin friction. Interestingly, as shown in figure 4.1, the previous observation leads to a counter-intuitive result, that the skin friction is higher at the location of the LMP compared to that at the valley.

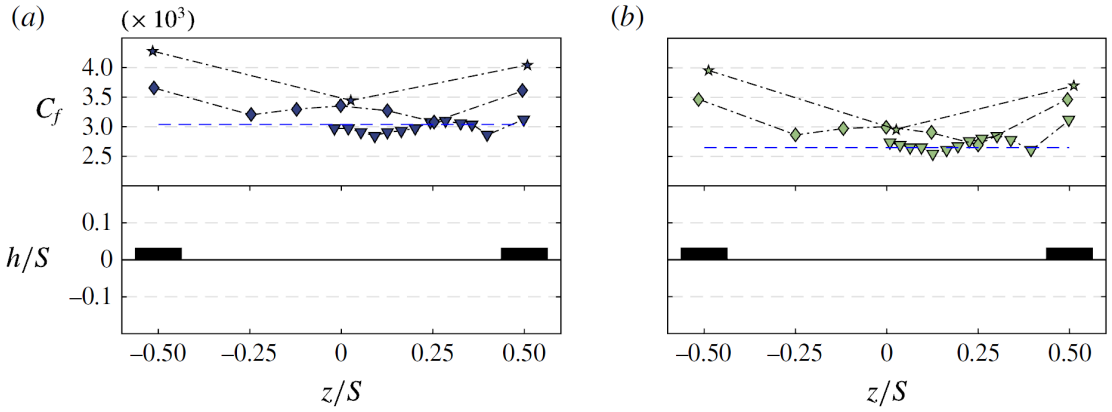

Figure 4.1: Spanwise variation of the skin-friction coefficient subjected to different spacings at different unit Reynolds numbers (★): X1HS1, (◆): X1HS2, (▼): X1HS3 and (−−): smooth wall. (a) $Re_x = 2{\times}10^6$, (b) $Re_x = 4{\times}10^6$.

Figure 4.2 shows the effect of Reynolds number on the spanwise distribution of $C_f(z)$ for both the X1HS2 and X1HS3 spacings. We notice that the reduction in C_f with Reynolds number is higher in the valley (HMP) compared to the surface elevation (LMP), which consistently holds for all the cases (including X1HS1). This behaviour indicates the existence of different activities at the LMPs and HMPs promoted by potential secondary flows that lead to a Reynolds number effect. The response of the spanwise distribution of the skin-friction coefficient $C_f(z)$ to X1HS2 and X1HS3 seems to follow a wavy type of behaviour with a different shape and magnitude. For X1HS2, a bump in the skin-friction distribution is formed with a local maximum (at the valley centre) observed at z/S = 0, then decays when getting close to the surface elevation. This region is labelled Zone 1 as illustrated in figure 4.2(a). For X1HS3 (as shown in figure 4.2(b)), two different zones can be observed. These zones can be identified as the regions between local minima in the spanwise distribution of C_f. The first zone extends from

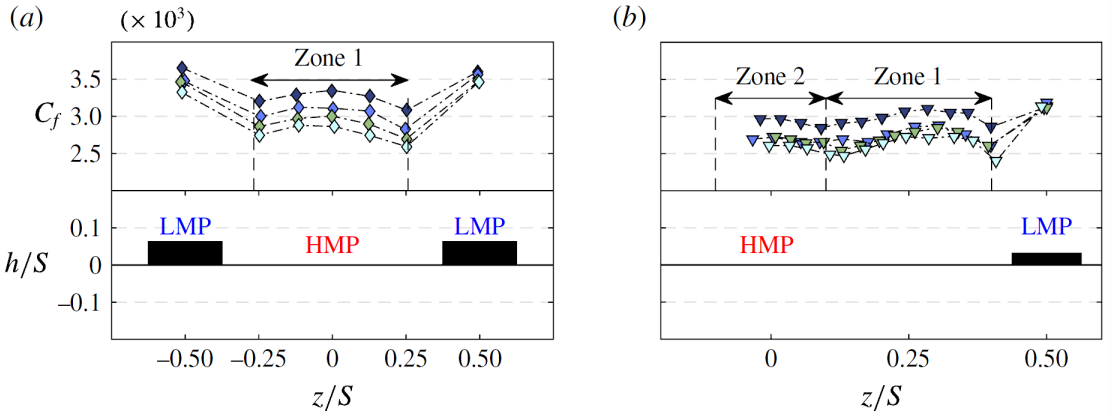

Figure 4.2: Spanwise distribution of the skin-friction coefficient and observation of the potential secondary and tertiary flow signatures represented by Zone 1 and Zone 2 respectively for (a) X1HS2 and (b) X1HS3 spacings, at different Reynolds numbers; (▼) : 2×10^6, (▼): 3×10^6, (▼): 3.9×10^6 (▽): 4.9×10^6.

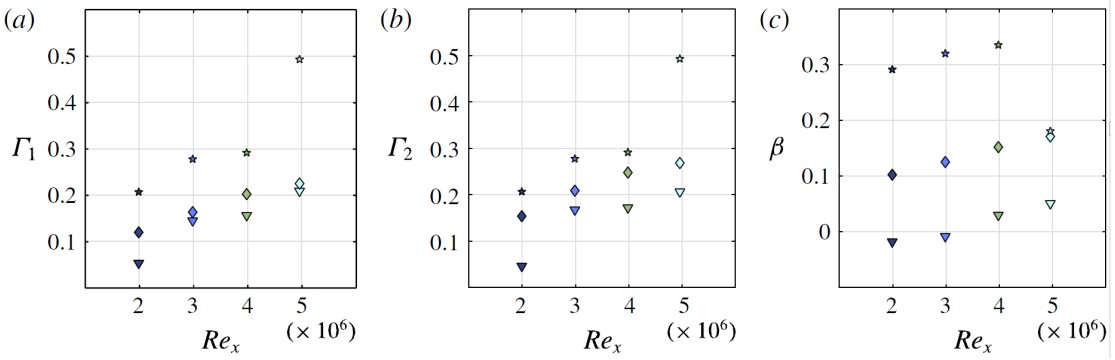

Figure 4.3: (a) Γ_1 and (b) Γ_2 plots illustrating respectively the global and local heterogeneity in the skin friction as defined in equation 4.1. (C) Spanwise-averaged skin-friction coefficient normalised with the smooth-wall data varying across the spacings at different Reynolds number, (★): X1HS1, (◆): X1HS2, (▼): X1HS3.

the edge of the surface elevation up to $z/S \approx 0.1$ and is similar to Zone 1 found for X1HS2. The second zone appears in the centre of the valley and spans from z/S = -0.1 to 0.1. These patterns (and zones) are also consistent with the locations of the HMPs and LMPs observed by Vanderwel and Ganapathisubramani (2015). The region labelled Zone 1 can be presumed to be the extent of the HMP induced by two counter-rotating rolling modes flanking the surface elevation. This region exists for both X1HS2 and X1HS3. However, Zone 2 for X1HS3 could be considered an effect of a tertiary flow (as identified by Vanderwel and Ganapathisubramani 2015) and is likely to be induced at the centre of the valley due to the larger value of S/δ_{av}.

Following these observations, it is evident that when a turbulent boundary layer grows over a spanwise heterogeneous surface, it not only leads to large scale flow field modifications, but also affects the surface stress distribution and the total drag generated by these surfaces will depend on the length scale of the heterogeneity.

Following the previous results, we attempt to quantify the variation in surface stress with surface heterogeneities in different ways. Figures 4.3(a) and (b) shows the ratios, defined as

$$\Gamma_1 = \frac{\frac{1}{W_p}\int_{-W_p/2}^{W_p/2} C_f(z)dz|_{peak}}{\frac{1}{W_v}\int_{-W_v/2}^{W_v/2} C_f(z)dz|_{valley}} - 1, \qquad \Gamma_2 = \frac{C_f(z = z_{peak})}{C_f(z = z_{peak} + W)}, \tag{4.1a, b}$$

with Γ_1 can be considered a global measure of flow heterogeneity which also enables us to quantify the amount of viscous drag produced by the low- and high-momentum pathways at different Reynolds numbers across different spacings. As an alternative measure, Γ_2 determines the ratio of the skin friction at the surface elevation over the skin-friction at an equivalent distance from the peak when normalised by the width of the ridge, which can be considered a measure of a local flow heterogeneity. Γ_1 and Γ_2 appear to both depend on the Reynolds number (Re_x) and spanwise spacing. Both quantities appear to systematically be higher for X1HS1 and decreases with increasing spacing (X1HS2 and X1HS3) with slightly higher values of Γ_2 for the X1HS2 and X1HS3 cases. As mentioned before, the variation in skin friction with Reynolds number is different for peaks and valleys, which translates to higher relative drag at the peak compared to the valley at high Reynolds number. It should be noted that the value of Γ_1 does not account for any effects caused by differences in the ratio of the width of peak to the spacing. In fact, W_p/S varies between the cases (0.5, 0.25 and 0.125 respectively for X1HS1, X1HS2 and X1HS3) which can have an effect on the organisation of the LMPs and HMPs, which consequently can affect the wall drag.

The spanwise-averaged skin-friction coefficient was determined as

$$C_F = \frac{1}{S}\int_{-S/2}^{S/2} C_f(z)dz \tag{4.2}$$

and was evaluated at different Reynolds numbers and for different spacings. Figure 4.3(b) shows measurements of $\beta = (C_F/C_{f_{smooth}}) - 1$, which represents a measure of the drag increase due to the surface heterogeneity. The value of β was typically higher for the X1HS1 surface, whereas the X1HS2 and X1HS3 surfaces have relatively lower values. It monotonically increases from low to high Reynolds numbers for the X1HS2 and X1HS3 cases, but shows a sudden drop for X1HS1. The reason for the sudden drop at the highest Reynolds number for X1HS1 is due to the decrease in C_f measured in the valley, which is also observed in figure 4.3(a). Additionally, figure 4.3(b) also shows a negative value at low Reynolds numbers for X1HS3. This result indicates a potential drag reduction behaviour, however, the difference (skin-friction reduction) is of the order of the uncertainty of the measurements.

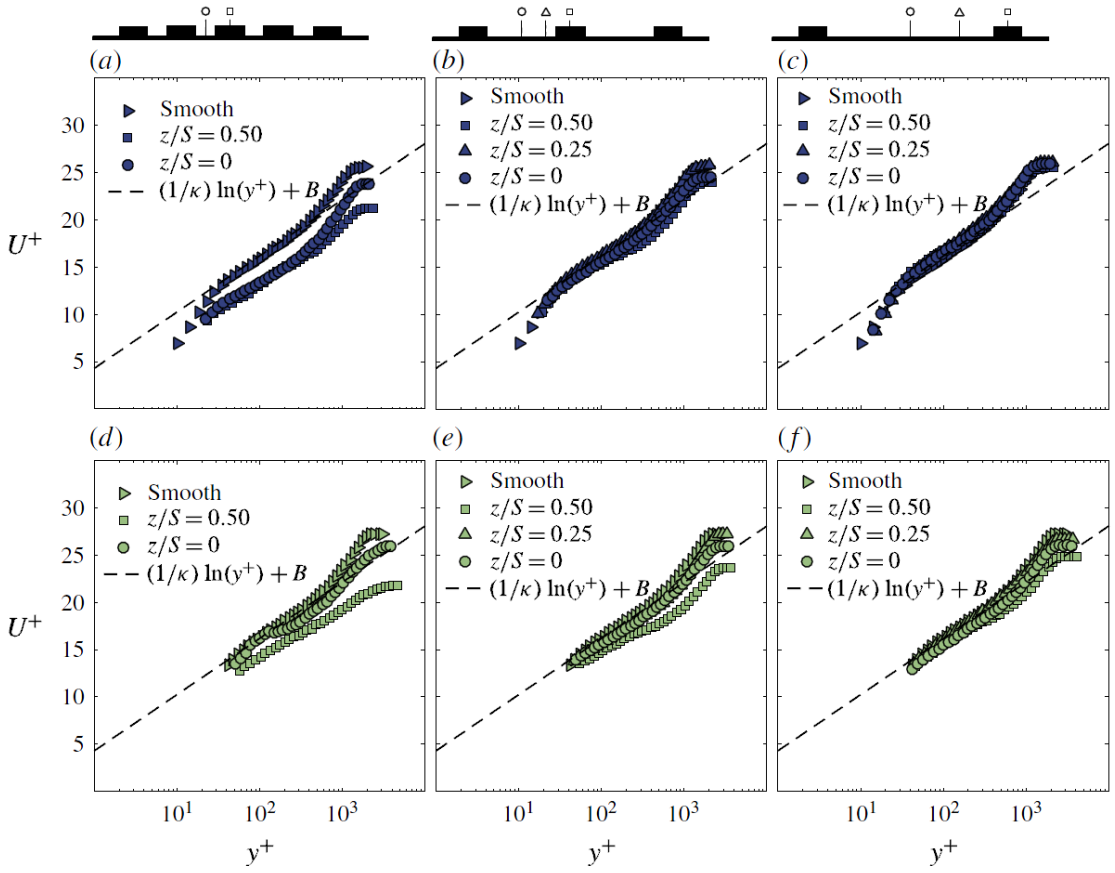

Figure 4.4: Inner scaling of the local velocity profiles for the (a,d) X1HS1, (b,e) X1HS2 and (c,f) X1HS3 spacings at (a,b,c) $Re_x = 2{\times}10^6$ and (d,e,f) $Re_x = 3.9{\times}10^6$. The values of the log-law slope κ and the smooth-wall intercept B used in this study are 0.387 and 4.29 respectively.

4.3 Mean velocity profiles

The mean streamwise velocity with the wall-normal location profiles are scaled with inner variables, U_τ for U and ν/U_τ for y, and plotted with the $^+$ symbol in figure 4.4. It is important to clarify the origin for the wall-normal direction as this is a source of contention in many studies of rough-wall flows. For the current study, the vertical origin was deliberately defined as the location where the flow touches the wall. This mean that, the origin for valley profiles is at the bottom of the surface while for the peak profiles, the origin is located at the peak. This will allow us to compare both the near-wall and outer-scaling laws at different spanwise locations. Figure 4.4 shows the effect of spacing in columns and Reynolds number in rows. All profiles seem to show the existence of a log-layer in the mean velocity profiles for different spanwise locations. At low Reynolds number, the hot-wire resolves the near-wall layer (buffer layer) down to 10 wall units. A good collapse in the near wall of the profiles can be seen for X1HS2 and X1HS3. However, inner-scaled velocity profiles seem to be more variable for X1HS1, observed both at the near-wall and the wake part of the boundary layer. A downward shift can

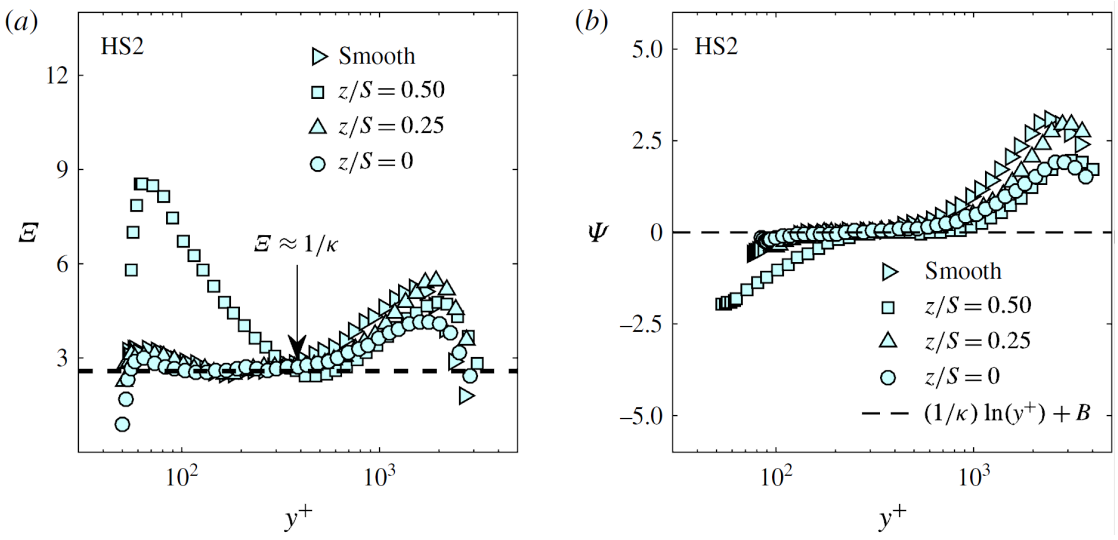

Figure 4.5: (a) Variation of the indicator function Ξ and (b) variation of the Ψ function for different spanwise locations at the highest Reynolds number for the X1HS2 case. In the present study, a second-order central-difference scheme was used in order to obtain Ξ.

be observed accompanied with a different wake strength for both locations $z/S = 0.5$ and $z/S = 0$. The wake seems to be weaker at the surface elevation and stronger at the valley. The mean velocity profiles show a trend that is similar to the skin friction where the mean flow is strongly affected by the heterogeneity for X1HS1, then the flow starts recovering towards the smooth wall for X1HS2 and X1HS3. This is confirmed in figures 4.4(d), (e) and (f) at higher Reynolds number. The wake strength appears to be weakening for the profiles at the peaks. From previous studies, the peaks coincide with the LMPs which are dominated by an upwash motion that increases the turbulence activity across the boundary layer, which can result in a lower activity of intermittency at the peak.

Surface roughness is known to induce a wall-normal as well as velocity shifts in the inner-normalised mean velocity profiles as shown in figure 4.4 resulting from both a roughness function (ΔU^+) and a zero-plane displacement (d). Despite the walls presenting a smooth texture, the fact that spanwise topographical variations are present, the quantities d and ΔU^+ cannot be assumed to be zero, as in smooth-walls. In this case, d is deduced from a modified indicator function by taking the derivative of equation 2.15 with respect to y, which leads to

$$\Xi = \left(y^+ - d^+\right) \frac{dU^+}{dy^+} = \frac{1}{\kappa}. \tag{4.3}$$

This form is usually used to identify the existence of a log-layer in the mean velocity profile and the determination of the log-layer slope, $1/\kappa$, for smooth walls (Österlund et al. 2000; Segalini et al. 2013). In the present study $1/\kappa \approx 2.58$ was fixed (measured

from the smooth-wall profiles) and d^+ is found to be the value that minimizes the difference Ξ - $1/\kappa$ in the plateau of Ξ as shown in figure 4.5(a). In should be noted that the values of the zero-plane displacement are negligibly small for the valley profiles, except at the peak which exhibited a substantial offset. In fact, the zero-plane displacement was found to vary between $0.2h$ and $0.7h$, however the measurement in the valley did not show any effective change in the location of the log-layer.

Once the zero-plane displacement is determined, the log-layer profiles are subtracted from the inner-normalised mean velocity profile to obtain a quantity, Ψ,

$$\Psi = U^+ - \frac{1}{\kappa}\ln\left(y^+ - d^+\right) - B + \Delta U^+. \tag{4.4}$$

Figure 4.5(b) shows the profiles of Ψ for different locations. ΔU^+ is determined as the value that minimises Ψ in the log region to a value of approximately zero. This procedure is repeated for all spacings and locations over a range of Reynolds numbers. The range of ΔU^+ obtained for the three cases for the different Reynolds numbers spans from -1 to 4.3 as illustrated in figure 4.6. There is no clear trend in the values of ΔU^+ for X1HS1 at the peak and valley. However, it is clear that for X1HS1, ΔU^+ is higher at the peak than the valley. For the X1HS2 and X1HS3 cases, a monotonic increase in ΔU^+ for the peak locations is observed, while, at the valley there are different trends with Re_θ ($Re_\theta = U_\infty\theta/\nu$ with θ representing the momentum thickness). Additionally, it is apparent that with increasing spacing, the roughness function and the roughness effects tend to decrease as observed in figure 4.3(b) which also showed the impact of the spanwise spacing in the total drag produced by these surfaces. In fact, for X1HS3, the values of ΔU^+ appear to be negative for lower Reynolds numbers (especially for z/S = 0 and 0.25), which could be interpreted as local drag reduction. It is worth pointing out that the analysis of d and ΔU^+ in this context is different to that generally done for the classical homogeneous rough surfaces, as these quantities have arisen due to the three-dimensionality of the flow, itself imposed by the surface condition.

In order to further assess the drag of the heterogeneous surfaces, the example of variation of C_f along the span for the X1HS2 case compared with a smooth wall is plotted against the local Reynolds number based on momentum thickness (computed from hot-wire data) in figure 4.7. The figure shows that the smooth wall OFI data matches relatively well with the semi-empirical relation of Nagib et al. (2007) (deviation less than 2.5%). As observed from the measurements of $C_f(z)$ for the X1HS2 case at different spanwise locations, the surface tends to create higher drag over the surface elevation than the valley (similar to the results observed from the figure 4.6). At the highest Reynolds number achieved in our facility, the difference in C_f for $z/S = 0.5$ and the smooth wall at $Re_\theta \approxeq 8000$ is around 35%. Different trends seem to exist along the span for X1HS2. At the peak, the skin friction seems to adopt a monotonic behaviour with a weak positive slope indicating skin-friction increase with Reynolds

number. However, a different evolution can be observed for the skin friction at $z/S = 0$ and $z/S = 0.25$. The skin-friction coefficient is observed to decrease until a certain Reynolds number which then transitions to an increasing C_f.

An additional way for estimating the roughness function is from the difference between the skin friction of a rough-wall from that of a smooth-wall at equivalent Reynolds numbers based on the momentum thickness (Hama 1954)

$$\Delta U^+ = \left(\sqrt{\frac{2}{C_f}}\right)_s - \left(\sqrt{\frac{2}{C_f}}\right)_r . \tag{4.5}$$

This allows us to obtain an estimate of the roughness function with the advantage that knowledge of the zero-plane displacement is not required. The roughness function evaluated from equation 4.5 showed consistent trends with comparison to ΔU^+ estimated from equation 4.4, however with differences in magnitude of up to $\pm 20\%$. These differences tend to systematically reduce with increasing spacing. The observed quantitative differences are because the ΔU^+ estimated from 4.5 is contingent on flow over both the smooth- and rough-wall exhibit wake similarity, which translates to a collapse in the mean velocity profiles in defect form. This suggests that the impact of surface heterogeneity on the wake strength Π should also be evaluated.

The wake strength depicts the departure of the mean velocity profiles from the logarithmic behaviour and most studies assume that rough and smooth walls have a universal wake parameter (Castro, 2007), which further feeds into the arguments of outer-layer similarity. Although different analytical expressions for the wake function w yield different values of Π (Nagib et al., 2007)), the conclusion drawn from the current study remain unchanged when employing alternative expressions. In the current study, the expression by Hinze (1975) is shown to best fit the wake region and is deemed appropriate for the subsequent analysis. The analytical expression is given as,

$$w\left(\frac{y}{\delta}\right) = 2\sin^2\left[\left(\frac{y}{\delta}\right)\frac{\pi}{2}\right]. \tag{4.6}$$

Π is subsequently determined through a best fit in the least square sense using the composite expression log-wake and the measured velocity profiles. Figure 4.7(b) illustrates the values of the wake strength obtained for the case of X1HS2 plotted against Re_θ (all values are tabulated in table 4.1). In the present case, we observe that Π is also affected by the spanwise heterogeneity of the surface which shows a weakening of the wake parameter. The smooth-wall results are shown to be in agreement with smooth-wall values found in the literature (depending on the choice of the function w and (κ, B)). Different trends appear for different spanwise locations. At the peak, the value of Π is lower and decreases with Re_θ. Similar observations can be made for the wake strength measured at the valley, but, relatively the value of Π is closer to the smooth-wall's. This behaviour is however different at $z/S = 0.25$, where Π is shown to increase initially with Reynolds

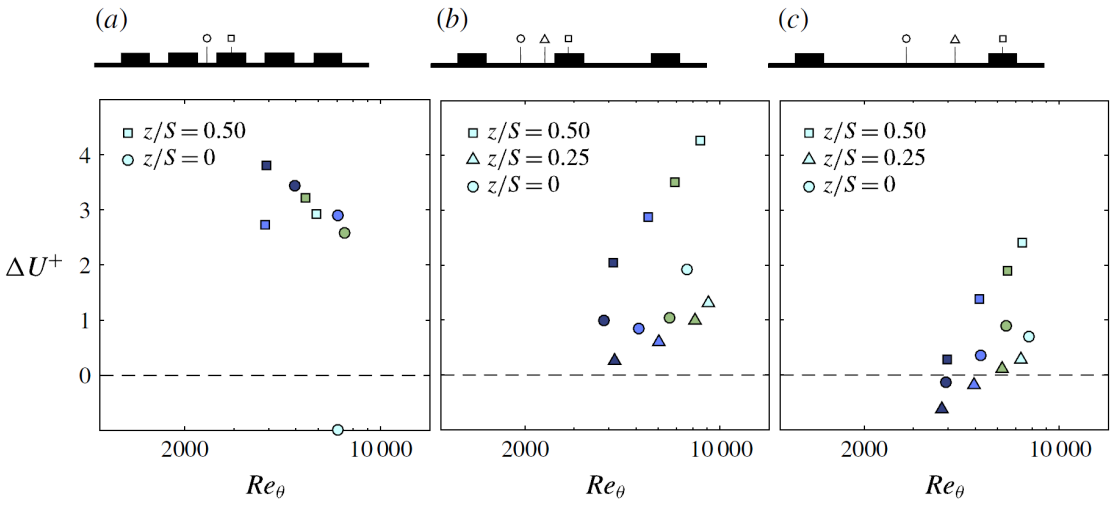

Figure 4.6: Evolution of the roughness function with Reynolds number based on the momentum thickness Re_θ at different spanwise locations, for (a): X1HS1, (b): X1HS2 and (c): X1HS3, with the ΔU^+ herein is estimated from the function Ψ. The symbol colours are explained in figure 4.2.

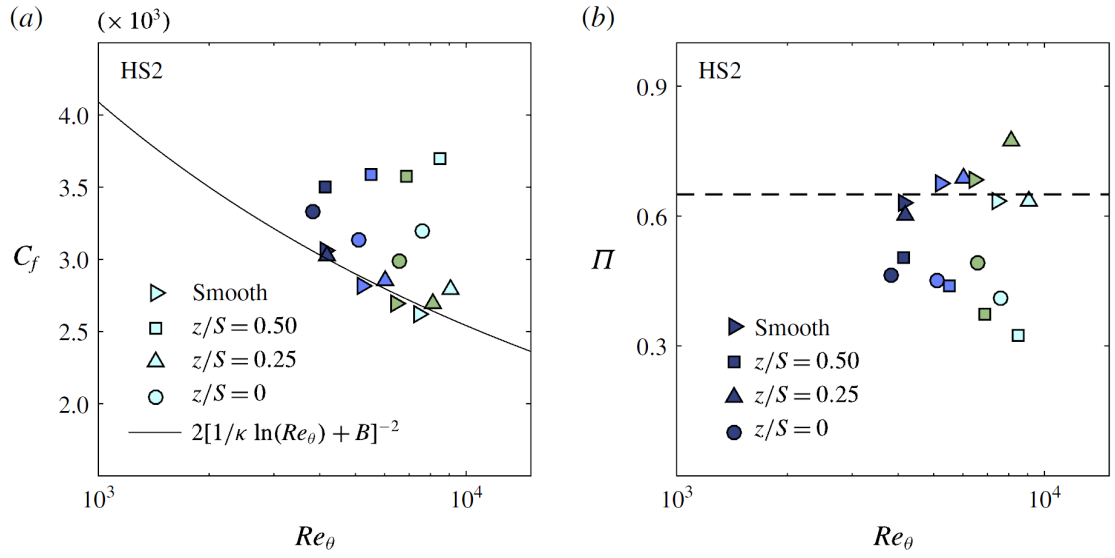

Figure 4.7: Variation of the (a) local skin-friction coefficient and (b) the wake strength with respect to the Reynolds number based on the momentum thickness for X1HS2 spacing at different spanwise locations. The black-dashed line represents the average value from the four different Reynolds numbers of the smooth-wall data with $\Pi \approx 0.65$. The symbol colours are explained in figure 4.2.

number and is seen to decrease after a certain Reynolds number. The scatter of the wake strength values not only illustrates the inhomogeneity in the mean flow but also in the turbulence. This also indicates that outer-layer similarity might not exist in these flows, as will be discussed in the following section.

Table 4.1 summarises the different values of different boundary layer characteristics for the three cases over a range of Reynolds numbers discussed above. Note that this

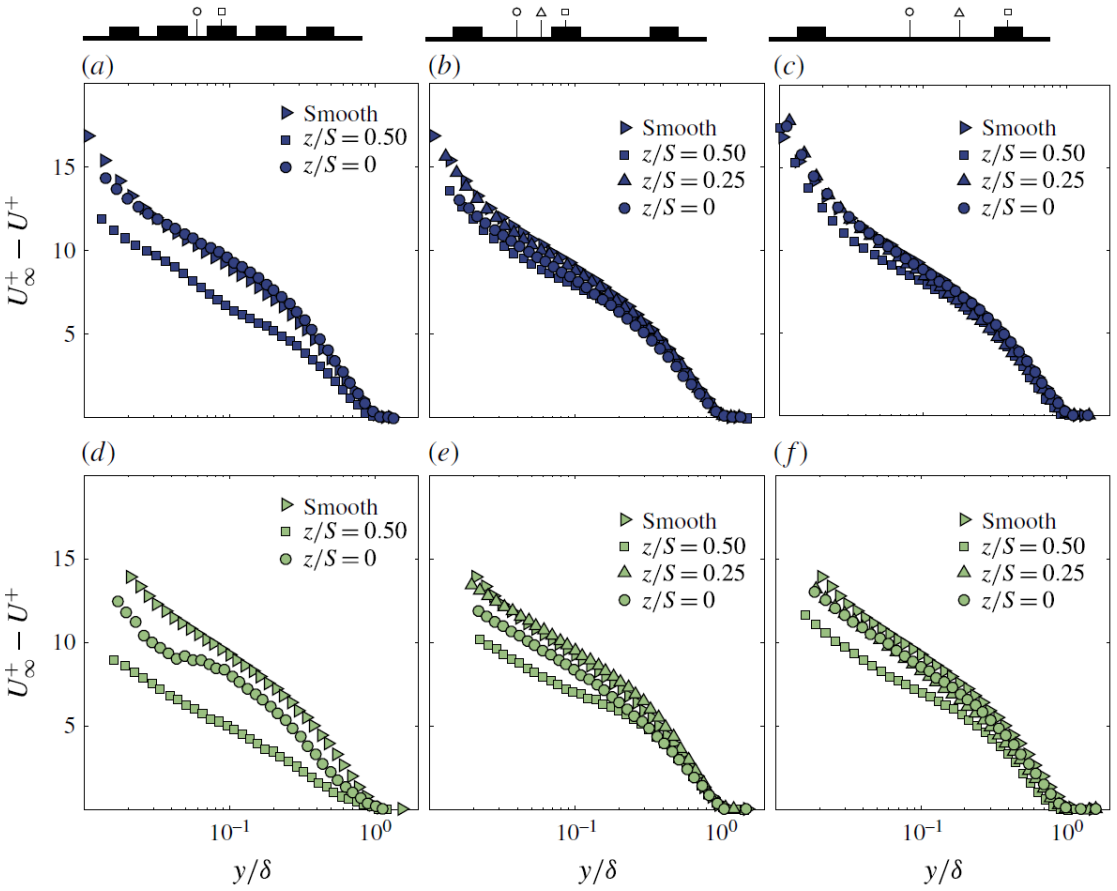

Figure 4.8: Outer scaling of the local velocity profiles for the (a,d) XIHS1, (b,e) XIHS2 and (c,f) XIHS3 spacings at (a,b,c) $Re_x = 2{\times}10^6$ and (d,e,f) $Re_x = 3.9{\times}10^6$.

table also has values of S/δ based on the local δ estimated from the profiles. However, in the context of secondary flows, it is perhaps suitable to define an average boundary layer thickness δ_{av} and normalise the spacing based on this value. The normalised-spacing of these average values are given in the table caption. This confirms that our cases are within the $S/\delta_{av} = \mathcal{O}(1)$.

Figure 4.8 shows the mean velocity profiles in defect form for the three spacings in column at two different Reynolds numbers in rows. Just as previous figures, the vertical origins are local (i.e. $y = 0$, where the wall is locally). The boundary layer thickness δ is also local from each profile. It is well established for homogeneous roughness that a collapse with smooth-wall data is observed from 0.2 δ onwards (Jiménez 2004, Castro 2007 and Squire et al. 2016), meaning that the surface roughness effects (viscous effects) are contained within the near-wall region, and the rest of the flow behaves as a smooth-wall flow. However, for heterogeneous surfaces as shown in figure 4.8(a), (b) and (c), we can observe a lack of collapse for all the cases. For the surfaces where S and δ are of the same order of magnitude, such as these, outer-layer similarity of local profiles is not expected to hold. At the peak, a strong deviation of the profiles from the smooth-wall

	Re_x	d/h			ΔU^+			Π			S/δ			$Re_\tau \times 10^3$		
Case	$\times 10^6$	P	M	V	P	M	V	P	M	V	P	M	V	P	M	V
X1HS1	2	0.4	-	0	3.7	-	3.4	0.3	-	0.75	0.85	-	0.77	1.58	-	1.57
	2.9	0.2	-	0	2.7	-	2.9	-1.1	-	0.67	0.79	-	0.73	2.45	-	2.31
	3.9	0.4	-	0	3.2	-	2.5	-0.1	-	0.30	0.76	-	0.71	3.21	-	3.02
	4.8	0.4	-	0	2.9	-	-1	0	-	0.34	0.88	-	0.84	3.34	-	2.78
X1HS2	2.1	0.4	0	0	2.0	0.2	1	0.56	0.60	0.47	1.63	1.59	1.64	1.42	1.35	1.37
	3	0.5	0	0	2.9	0.6	0.8	0.51	0.71	0.46	1.73	1.62	1.72	1.95	1.85	2.84
	4	0.7	0	0	3.5	1	1	0.45	0.80	0.50	1.75	1.63	1.81	2.55	2.41	2.29
	4.8	0.7	0	0	4.3	1.3	1.9	0.40	0.68	0.43	1.66	1.67	1.80	3.30	2.86	2.77
X1HS3	2	0.3	0	0	0.3	-0.6	-0.1	0.56	0.48	0.62	3.09	3.09	3.23	1.33	1.32	1.25
	3	0.4	0	0	1.3	-0.2	0.3	0.44	0.41	0.60	3.06	3.06	3.27	1.94	1.85	1.71
	4	0.4	0	0	1.9	0	1	0.35	0.42	0.53	3.05	3.17	3.36	2.63	2.33	2.22
	4.8	0.6	0	0	2.4	0.4	0.7	0.25	0.37	0.56	3.05	3.27	3.51	3.31	2.82	2.61

Table 4.1: Boundary layer characteristics for three different heterogeneous surfaces at different unit Reynolds numbers with X1HS1 : $\frac{S}{\delta_{av}} \approx 0.8$, X1HS2 : $\frac{S}{\delta_{av}} \approx 1.7$ and X1HS3 : $\frac{S}{\delta_{av}} \approx 3.2$. P, M and V refer to the spanwise locations of the peak, mid-peak-valley and valley, respectively.

can be observed, not only in the magnitude but also in shape. As the spacing increases, the shape of the profile starts to recover as seen for case X1HS3.

The above observation is consistent with the behaviour of the wake strength, which was shown to vary at different spanwise locations. Additionally, there seems to be a Reynolds number effect on these mean velocity profiles in defect form. As seen in figures 4.8(e) and (f), the collapse is worse between two points in the valley (centre of valley, $z/S = 0$, and mid-valley-peak point, $z/S = 0.25$). In fact, as the Reynolds number increases, the lack of collapse is found to get worse in the outer layer reaching almost the entire boundary layer thickness regardless of the spacing. This suggests that as Reynolds number increases, the secondary flows grow stronger in the outer region but its effect is not felt to the same extent at the wall. This leads to a lack of collapse in defect profiles, when scaled with a local skin-friction velocity, since the effect is not uniformly proportional across the vertical extent. Perhaps, this is the reason why Wu and Christensen (2007) found outer-layer similarity in flows over spanwise heterogeneities. They determined the skin-friction velocity in the outer region (using the Reynolds shear stress method) which could have provided a different estimate that is directly proportional to the strength of the secondary flow. However, this value is not representative of the local surface shear stress. This is also consistent with Nugroho et al. (2013), who indicated that the outer-layer similarity cannot hold in the presence of secondary flows due to the occurrence of the upwash and downwash motions.

These defect profiles also indicate why the skin friction is higher at the LMPs rather than the HMPs. The measured skin friction is representative of the viscous shear stress $\mu\frac{dU}{dy}$. The shape of the boundary layer at $z/S = 0.5$ seems to be fuller compared to that at $z/S = 0$, which is also higher than at $z/S = 0.25$. This is an indication of the variation of the velocity gradient at the wall across the span. Therefore the results we previously observed in the spatial distribution of the skin friction are in line with the data provided by the mean velocity profiles. Therefore, from the results presented herein, we observe that outer-layer similarity is not fulfilled when the turbulent boundary layer is perturbed by a surface heterogeneity. Note that according to the current spanwise wavelengths investigated, all of our cases and as indicated in the section 2.3 are expected to produce secondary flows. As Reynolds number increases, the effect of secondary motions on the mean flow increases, but, its effect on skin friction is perhaps not as strong. Therefore, when using the local drag for scaling, the lack of collapse is evident.

4.4 Properties of the turbulent flow

In order to assess the influence of these spanwise heterogeneous surfaces on turbulence statistics, inner-normalised turbulence intensity profiles are examined (figure 4.9, left column). Variations in the normalised profiles between the measurements from different

spanwise locations occur for each of the surfaces investigated. The differences in the magnitude along the span can be explained by the heterogeneity in spatial distribution of the wall shear stress. For instance, the value of U_τ is locally higher at the peak and therefore normalising the profiles with that value will lower the magnitude of turbulence compared to others. However, this alone cannot explain the lack of collapse since the shape of the profiles are substantially different. This would suggest the flow is influenced differently at different spanwise locations by the secondary motions. The lack of collapse of the normalised variance profiles is in line with results observed on the mean flow, which does not satisfy outer-layer similarity.

The outer-layer similarity in both mean flow and turbulence could be further examined through the diagnostic plot, first introduced by Alfredsson et al. (2011). It plots the streamwise fluctuation normalized by the local mean streamwise velocity against local mean streamwise velocity normalised by the free stream velocity. This removes the dependence of the profiles on skin-friction velocity and helps reveal a region in the flow where the local turbulence intensity varies linearly with U/U_∞. Although, in rough-wall flows, the slope is different compared to smooth walls but is independent of surface morphology for fully-rough conditions (Castro et al. 2013). Although this might be the case for homogeneous surfaces, the cases where heterogeneity underpins the flow has not yet been considered. Figure 4.9 shows the "diagnostic plots" (right column) for different spacings. The heterogeneity seems to have altered the profiles for X1HS1, where both the peak and valley profiles deviate from the smooth-wall and fully rough-wall slopes, exhibiting a transitional behaviour. This perhaps is due to the flow which is not fully-rough. However, as the spacing increases (for X1HS2 and X1HS3), the data appears to collapse on the smooth-wall line. This means, locally, despite the spanwise heterogeneities, the mean and turbulence go hand-in-hand. The relative motion of the turbulence and the mean flow structures are similar to that of a smooth-wall, which seems to hold best for X1HS3 where the spacing is largest. This gives further evidence on the effect of secondary motions on the mean flow and turbulence. The secondary flow affects mean flow and turbulence in the outer region proportionally and therefore they tend to collapse in this diagnostic form. However, since the effect of secondary motion is not the same at the wall, this leads to lack of collapse when plotted in outer-layer similarity form.

In order to examine the scales that are affected by the spanwise heterogeneities, spectral analysis is performed. Figure 4.10 shows the inner-normalised premultiplied energy spectra of the streamwise velocity fluctuations against the inner-normalised wall distance y^+ together with the normalised turbulence profiles. A generic smooth-wall case as well as different spanwise locations from X1HS2 case are shown (at a low Reynolds number, where it is still possible to capture the near-wall peak for the X1HS2 case). The near-wall peak in turbulence as well as in the spectra is located at around $y^+ \approx 15$. The spectral peak is approximately at 1000 wall units. The existence of the peak is due to the

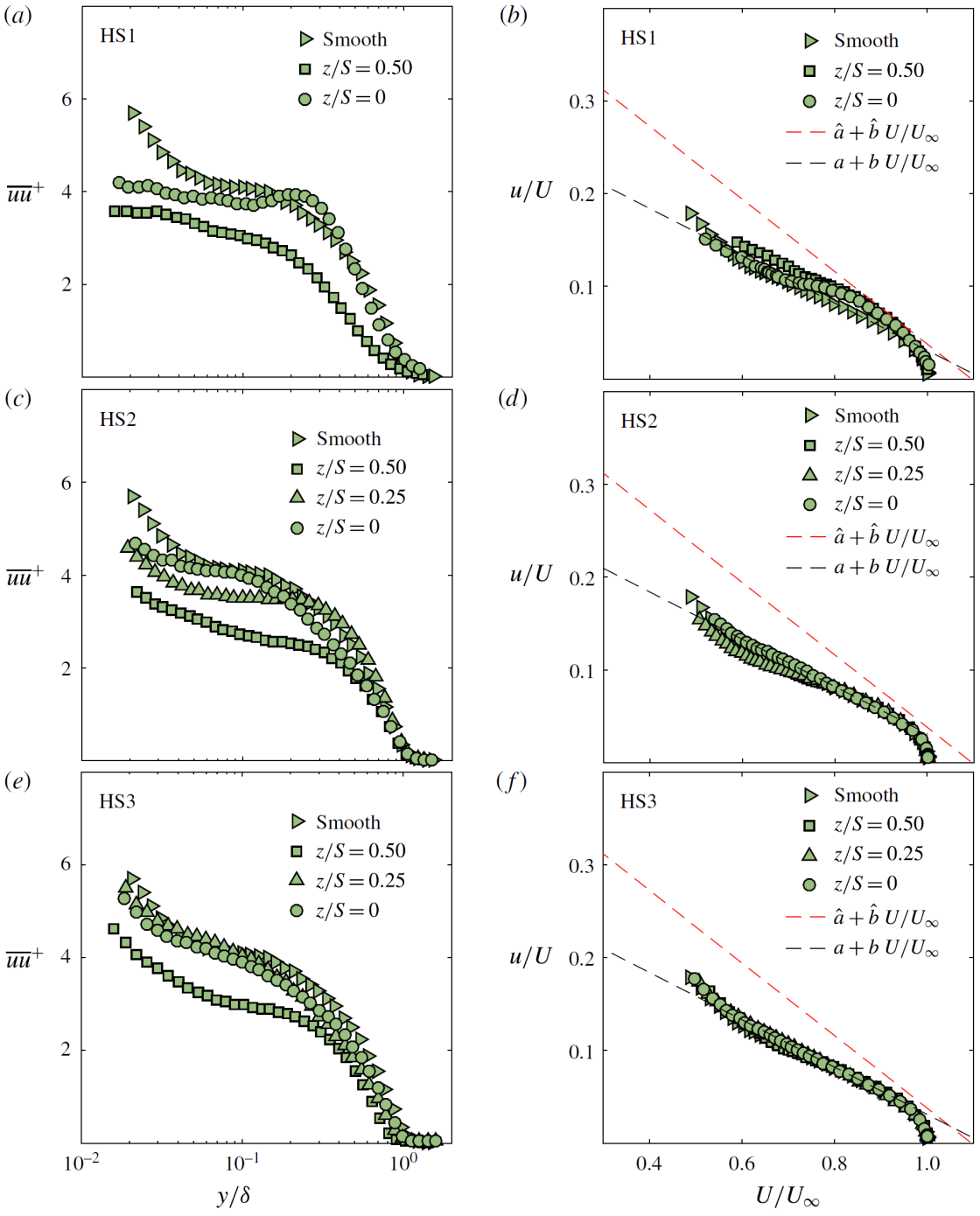

Figure 4.9: Effect of the surface heterogeneity on profiles of inner-normalised turbulence (a,c,e) and on the diagnostic plots (b,d,f) for the three spacings at $Re_x = 3.9{\times}10^6$.

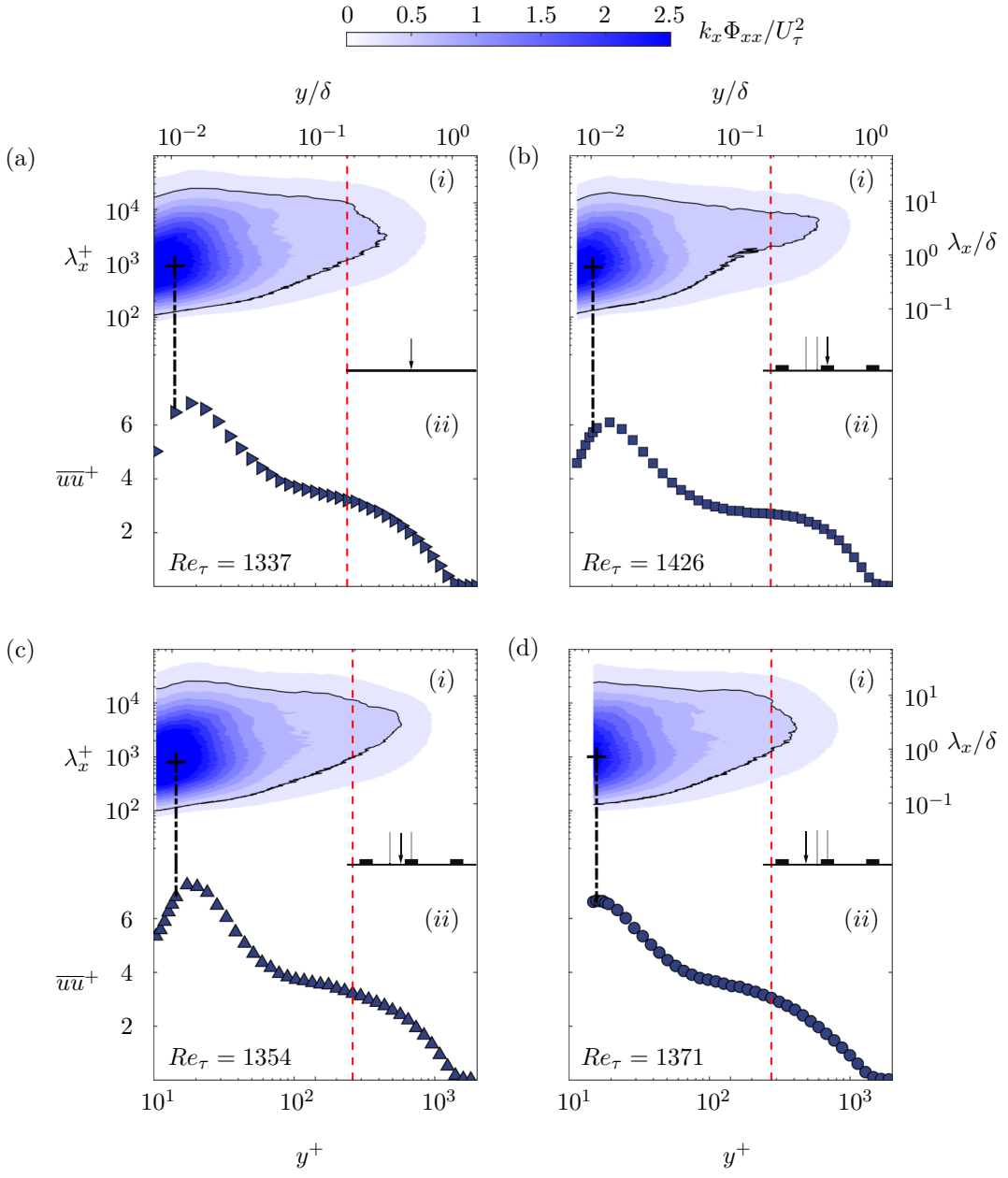

Figure 4.10: (i) Premultiplied streamwise energy spectrograms for the (a) smooth and (b,c,d) X1HS2 spacing case at $Re_x = 2{\times}10^6$ that are at relatively similar Re_τ and (ii) their respective broadband turbulence intensities. The red-dashed line marks the edge of the inner/outer boundary layer while the black contour line represent the energy level at $k_x\Phi_{xx}/U_\tau^2 = 0.5$.

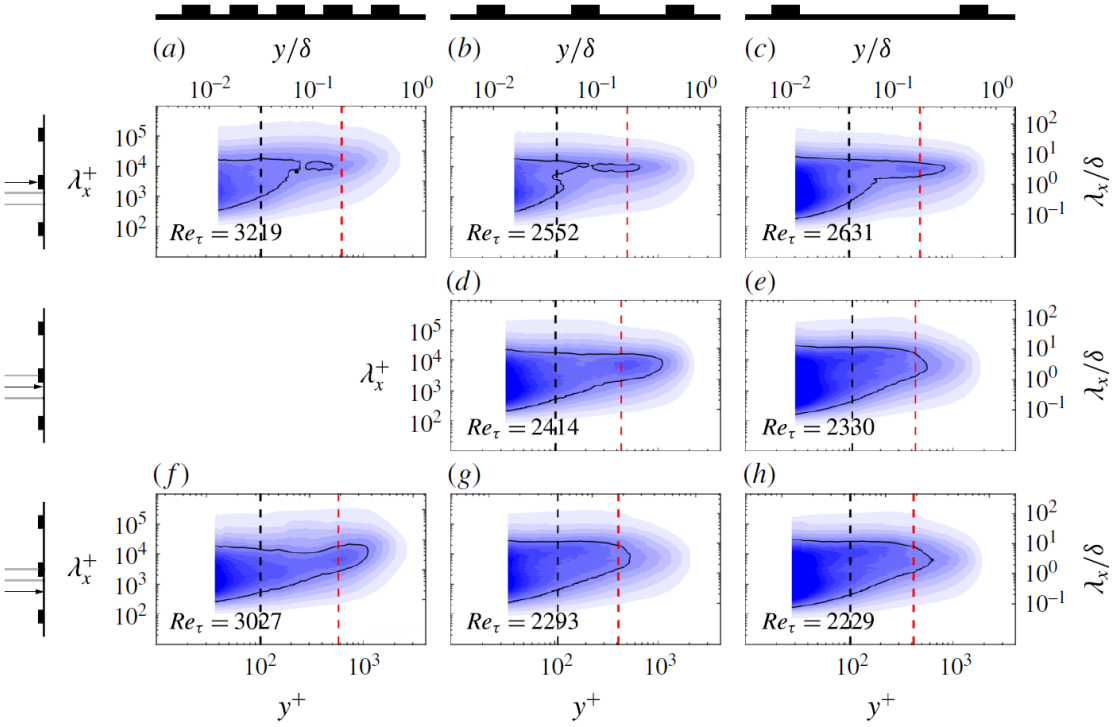

Figure 4.11: Premultiplied streamwise energy spectrograms for the three spacings at different spanwise location at $Re_x = 3.9{\times}10^6$. The columns are for different spacings and the rows are for different spanwise location as indicated in the figure. The black-dashed lines mark the wall-normal location at $y^+ \approx 100$ and the red-dashed lines at the wall-normal location $y/\delta \approx 0.2$ which are shown in figure 4.12 as extracted plots. The black contour line represent the energy level at $k_x\Phi_{xx}/U_\tau^2 = 0.3$.

presence of near-wall streaks in smooth walls. It seems that the spanwise heterogeneous smooth surface also retains the same characteristics at all spanwise locations. This further reinforces the claim that the effect of secondary flows on the near-wall region is limited and does not alter the structure or scaling locally in the viscous dominated region. Note that this behaviour cannot be captured at higher Reynolds number as the viscous sublayer becomes too small to be resolved in our measurements.

Spectrograms for the three different spacings (X1HS1, X1HS2 and X1HS3) at $Re_x \approx 4 \times 10^6$ are shown in figure 4.11. The figure shows the spectrograms for each spacing in the columns and the spanwise locations of the measurement in rows. Comparison of spectra at the peak (first row) across different spacings indicates that the spectra in the near-wall region become more energetic with increasing spacing. This is consistent with the variance profiles in the near-wall region. In fact, the near-wall energy content across all scales starts to approach that of a smooth-wall with increasing spacing. However, at this location, the spectra will always be affected since the boundary layer is growing over an element of finite spanwise width and this will presumably generate secondary motions regardless of how large the spacing is between adjacent ridges. In the outer region, this

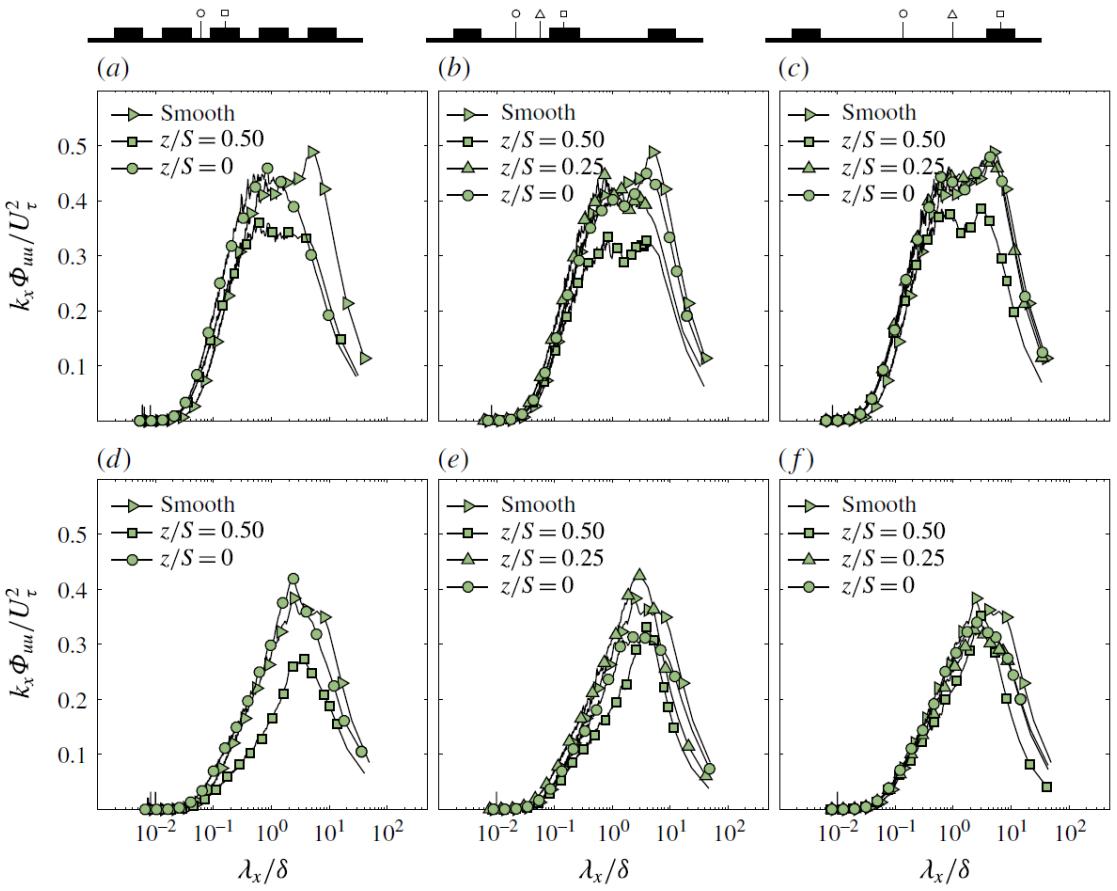

Figure 4.12: Normalized pre-multiplied energy spectra of the streamwise velocity fluctuation taken at $y^+ \approx 100$ (top row) and $y/\delta \approx 0.2$ (bottom row) for the three spacings at $Re_x = 3.9{\times}10^6$.

leads to a new energy containing region whose length-scale is nearly constant with wall-normal location. The energy contained in this region increases with increasing spacing.

The second row in figure 4.11 shows the premultiplied spectrograms at the mid-point between the peak and valley. This information is only available for X1HS2 and X1HS3 cases. X1HS3 appears to exhibits higher energy content compared to X1HS2 across all scales, especially in the inner region (i.e. $y^+ < 100$). However, X1HS2 seems to indicate a local peak in the outer region, which is not observed in the case of X1HS3. This is presumably due to the fact that at this location ($z/S = 0.25$) the strength of the induced secondary motions that flank the surface elevation become weaker for a higher value of S/δ_{av}.

The final row in figure 4.11 shows the variation in energy content at the valley of the three cases. The near-wall region of X1HS2 and X1HS3 appear to be similar for this spanwise location compared to X1HS1, which shows a less energetic near-wall region. However, in the outer region of X1HS1, an outer spectral peak seems to show as a higher energy content compared to the larger spacings is observed between $y/\delta = 0.1$ and 0.3 for a range of wavelengths. Similar to the previous observation from the second

row spectrograms, this also can be explained by the effect of the spacing between two adjacent strips.

In order to further assess the effect of surface heterogeneity on the spectra, a look at the energy distribution across the scales at two wall-normal locations for the three cases is presented. Figure 4.12 shows premultiplied energy spectra at both $y^+ \approx 100$ (top row) and $y/\delta \approx 0.2$ (bottom row) for different cases, which represent the black- and red-dashed lines in figure 4.11 respectively.

The energy distribution in the inner region (top row of figure 4.12) reveals the presence of local similarity in the spectra. In fact, a degree of similarity seems to exist for the wavelengths smaller than $\lambda_x \approx 0.3\delta$ across the spanwise locations, and increases with increasing spacing, whereas at wavelengths larger than $\lambda_x \approx 0.3\delta$, the collapse is essentially lost for the X1HS1 and X1HS2 cases. This indicates that in the inner region, the surface heterogeneity has a higher impact on the large scales than the small scales. The figure also shows that X1HS3 exhibits similarity with the smooth-wall even at larger scales at z/S =0.25 and 0. This suggests that similarity (or collapse) is lost for $z/S = 0.5$ while the presence of spectral similarity in the valley recovers (both at $z/S = 0.25$ and 0) for higher values of S/δ_{av}. Therefore, there is a tendency to return to universality with increasing spacing. However, even for the largest spacing considered here ($S/\delta_{av} \approx 3.2$), the large scales of the flow remain strongly affected by the surface heterogeneities at the surface elevation ($z/S = 0.5$). This is consistent with the very recent results presented by Yang and Anderson (2017) who found that the features of spatial auto-correlations are strongly dependant on the length scale of the spanwise heterogeneity.

The energy distribution in the outer region (bottom row of figure 4.12) reveals the existence of a similar trend for the small scales as in the inner region, where a good collapse in the small scales of the spectra (up to $\lambda_x/\delta \approx 0.1$) can be observed for all three cases across the different spanwise locations. Moreover, similarity seems to extend up to $\lambda_x/\delta \approx 1$ for the valley profiles (both at $z/S = 0.25$ and 0). Unlike the spectra at the valley, the premultiplied energy spectra at the surface elevation shows lack of similarity across all the scales for all three spacings. In fact, the magnitude of the outer spectral peak seems to be much lower compared to that of the valley regardless of the case. This effect tends to diminish with increasing spacing. This is in line with the findings of Nugroho et al. (2013), who made similar observations, where the overall magnitude of the energy spectra is lower than that of a smooth-wall. This suggests that secondary motions induced by the heterogeneous surface start to add new energetic scales in the outer region, which will go towards negating the validity of outer-layer similarity. It should also be noted that Re_τ decreases with increasing spacing and therefore the cases are not at matched friction Reynolds number (however, the variation are less than 20% and is not going to significantly affect this observation.

At this stage, it is unclear which property (mean flow, turbulence statistics or the spectra) will return to similarity first with increasing spacing. Given that the secondary motions are sustained by turbulent transport, it is expected that these phenomena likely take place simultaneously. However, further studies are required to examine this in more detail.

4.5 Summary

The characteristics of a turbulent boundary layer under the influence of surface heterogeneities have been investigated. Idealised heterogeneous surfaces were created by means of smooth streamwise-aligned ridges for three different spanwise spacings, $S/\delta_{av} \approx 0.8$, 1.7 and 3.2. Previous studies suggest that these surfaces induce large-scale secondary motions (with decreasing strength/significance). Data for skin friction from OFI and single point hot-wire velocity measurements were used to assess the limitations of similarity laws in these flows.

The effect of the surface heterogeneity on the wall drag was shown to both be a function of the spacing S/δ_{av} and Reynolds number indicating that the smooth heterogeneous surfaces were transitionally rough. The spanwise distribution of the C_f was shown to have variations with surface heterogeneity. The ratio of the skin-friction coefficient at the peak and the valley of the surface was as high as 1.5 for X1HS1 ($S/\delta_{av} \approx 0.8$) and down to 1.2 for X1HS3 ($S/\delta_{av} \approx 3.2$). The spanwise-averaged skin friction was up to 30% larger than that of a smooth-wall and this quantity also depends on the Reynolds number.

Mean velocity profiles at different spanwise locations exhibit a log-layer and this was used to compute the roughness function and the zero-plane displacement. The zero-plane displacement was found to vary between $0.2h$ and $0.7h$ (h being the height of the elevated smooth surface), however the measurement in the valley did not show any effective change in the location of the log-layer. The roughness function however, was shown to vary along the spanwise location with different regimes. This value of ΔU^+ is consistent with those obtained from an integral method. As illustrated for X1HS2, at the surface elevation the skin friction is observed to constantly increase with Re_θ, however a transitional behaviour is observed at the valley, where C_f is seen to decrease before increasing at the highest Reynolds number achieved in this experiment. The wake strength parameter Π was also assessed and was found to highly depend on the spanwise spacing. For $S/\delta_{av} \approx 0.8$, the wake was strongly reduced and weaker than that of the smooth- or rough-wall turbulent boundary layer. This can be related to the intermittency in the wake region which can be strongly affected by the presence of potential secondary flows, indicating a strong heterogeneity in the mean flow. The wake recovers at the valley to a smooth-wall value for higher spacings.

Mean velocity defect and turbulence intensity profiles do not follow outer-layer similarity across all locations for all cases. This suggests that even at the largest spacing of the study, $S/\delta_{av} \approx 3.2$, the secondary motions essentially destroy similarity. However, the turbulence intensity appears to be universally related to the mean flow at all locations for X1HS2 and X1HS3, while X1HS1 showed the profiles to be lined between the smooth and rough linear fits examined through diagnostic plots. This suggests that beyond a certain spanwise spacing S/δ_{av}, the mean flow and turbulence possess a degree of local similarity to each other and do not reflect the conditions at the wall. This also suggests that the influence of the secondary flow at the wall is not of similar extent to that in the outer region. The deviation of outer-layer similarity appears to start recovering for larger spacing at the valley indicating that even larger spacings are required to return to self-similarity.

The lack of similarity extends to spectra as well, with energy contained in the near-wall region increasing with increasing spacing (especially at the elevated surface), which is still less energetic than a smooth-wall. However, for larger spacings, the spectra in the near-wall region appears to approach that of a smooth-wall, especially for smaller wavelengths. The outer region starts to develop a new length scale (presumably from the secondary motions) across a range of wall positions for larger spacings. At the valley, an outer spectral peak is detected for $S/\delta_{av} \approx 0.8$. The energy here is higher than that of a smooth-wall but this peak is not apparent at larger spacings. The spectra in the outer region (beyond $y/\delta > 0.2$) appear to collapse in the smaller scales ($\lambda_x < 0.1\delta$) across all spanwise positions with increasing spacing. This suggests that the effect of secondary motions is not necessarily felt at the smaller scales other than to reorganise their presence through turbulent transport.

5. Effect of roughness geometry on the secondary flows in turbulent boundary layers over spanwise heterogeneous surfaces

5.1 Introduction

In this chapter, a turbulent boundary layer flow developing over spanwise heterogeneous surfaces whose spanwise characteristic length scales are comparable to the dominant length scale of flow is investigated. More specifically, the effect of surface geometry on the secondary flows and on skin friction is examined. The heterogeneity consists of smooth streamwise-aligned ridges of different shapes and widths with $S/\delta \approx \mathcal{O}(1)$. Cross-stream stereoscopic particle image velocimetry along with oil-film interferometry are used to investigate the flow field and assess the drag respectively. The experimental arrangement for this study is described in the section 3.2.2. Parts of this chapter have been published in Medjnoun et al. (2020).

5.2 The mean viscous drag and flow topology

Results from the OFI measurements are presented in figure 5.1. They describe the response of the surface shear stress to the presence of surface heterogeneity at various moderate Reynolds numbers Re_x obtained by varying the free stream speed. We specifically quantify the amount of viscous drag experienced by the wall at the valley, since this information is available for all the cases, estimated by:

$$C_f^* = \langle C_f(z_i) \rangle_{W_v}, \tag{5.1}$$

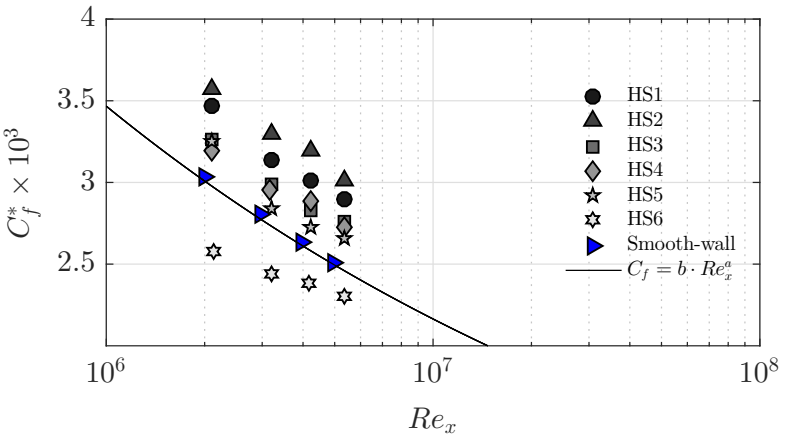

Figure 5.1: Variation of the valley spanwise-averaged skin-friction coefficient at various moderate Reynolds numbers for the different heterogeneous surfaces. The black solid line represents Schlichting's power-law with $a \approx -1/5$ and $b \approx 0.058$. The blue right-pointing triangles represent the smooth-wall data from Medjnoun et al. (2018).

with $\langle\cdot\rangle_{W_v}$ being the spatial average at the valley width ($W_v = S - W$) across the different discrete points z_i where the skin-friction coefficient was measured. The results show clearly the decay of the skin friction with respect to Reynolds number. This indicates that regardless of the surface heterogeneity, the flow remains Reynolds number dependant as opposed to rough-wall turbulence which asymptotes towards a constant value of C_f at "high-enough" Reynolds numbers (Jiménez 2004; Shockling et al. 2006; Flack and Schultz 2014; Djenidi et al. 2018). This can be explained by the fact that these surfaces do not present rough protrusions which in addition to viscous drag, lead to pressure drag which cause the fully-rough behaviour (Napoli et al. 2008; Yuan and Piomelli 2014). This observation leads to hypothesize that these smooth heterogeneous surfaces (as long as their texture is smooth) cannot meet the fully-rough conditions, and therefore will always remain a function of Reynolds number (from the skin-friction perspective). Meanwhile, these results show that the skin-friction coefficient is also dependant on the surface heterogeneity condition. In fact, if we compare the skin-friction coefficients at matched Re_x, we can clearly distinguish that the triangular cross-section case produces more skin friction than the half-round and the square, despite them having the same valley width ($(S - W)/\delta \approx 1$). This indicates the effect of geometry on the mean streamwise velocity gradient at the wall.

Schlichting's power-law curve (Schlichting, 1979) is shown to be in a good agreement in comparison with the present smooth-wall baseline case (compare the solid line against the blue right-pointing triangle in figure 5.1). The power-law further allowed to quantity these relative changes against the smooth-wall, and are tabulated in table 5.1 under the label β^*. This quantity clearly shows a net increase in skin friction at the valley for the cases X2HS1 to X2HS4 (relatively matched valley width $(S - W)/\delta$), with a 23% increase for X2HS2. On the other hand, X2HS5 and X2HS6 recorded lower values especially for the X2HS6 case which shows local skin-friction reduction. This can be due

Case	Symbol	h/δ	S/δ	W/δ	$(S-W)/\delta$	$C_f^* \times 10^3$	$C_F \times 10^3$	β^*	Re_τ	$\Gamma^* \times 10^2$	ξ
X2HS1	(●)	0.09	1.17	0.17	1	3.01	-	1.16	3125	4.42	4.61
X2HS2	(▼)	0.08	1.21	0.08	1.12	3.19	-	1.23	3347	5.27	6.83
X2HS3	(□)	0.09	1.14	0.08	1.05	2.82	-	1.09	3135	3.74	4.62
X2HS4	(◆)	0.09	1.26	0.18	1.07	2.88	2.87	1.11	2828	3.75	3.74
X2HS5	(★)	0.09	1.26	0.35	0.90	2.72	2.80	1.05	3239	3.21	2.71
X2HS6	(✡)	0.08	1.20	0.67	0.52	2.38	2.76	0.92	2829	2.78	1.72

Table 5.1: Geometrical characteristics and the aerodynamic parameters for the different heterogeneous surfaces measured at $Re_x \approx 4 \times 10^6$. The parameters C_f^*, C_F and β^* represent measures of the skin-friction coefficient from the OFI measurements and are discussed in section 5.2. The parameters Γ^* and ξ represent the secondary flow circulation and the surface parameter respectively and are discussed in section 5.4.

to the strong viscous blockage induced by the interaction of two boundary layers, one on the either ridge's side walls. However, if we compare the spanwise-averaged skin-friction coefficient C_F (also tabulated in table 5.1), we notice that the overall drag is still higher than that of a smooth-wall at an equivalent Reynolds number Re_x. Even though the latter information is not available for the first three cases since OFI method cannot be applied above their ridges, the expected overall drag should also be higher than that of a smooth-wall. From the above results, it is clear that the mean wall shear stress depends on both the geometry of the surface heterogeneity and Reynolds number. This can be further explored by examining the mean flow using the SPIV data.

Figure 5.2 shows the normalised mean streamwise velocity maps and the spanwise distribution of the skin-friction coefficient, with figures 5.2(a,b,c) delineate the shape effect while figure 5.2(d,e,f) describe the width effect. Consistent with previous studies, strong spanwise heterogeneities in the mean flow can be distinguished. These are represented in the form of alternating high- and low-momentum pathways between valleys and peaks respectively. The degree of spanwise heterogeneity in the mean flow has also impacted the spatial distribution of the skin-friction coefficient, due to the spanwise variation in the mean velocity gradient at the wall. This is in line with our previous experimental study from chapter 4 and the direct numerical simulation reported by Hwang and Lee (2018), which showed that the spanwise distribution of the skin friction to strongly vary across the span, especially near the spanwise step-change with sharp changes occurring due to the discontinuity (see figure 11 of Hwang and Lee 2018).

Figure 5.2 also shows relative similarities between the mean velocity maps and the spanwise distribution of C_f for X2HS1 to X2HS4. In fact, despite the inability of measuring the local skin friction at the peak symmetry plane ($z/S = \pm 0.5$), the shape of $C_f(z)$ remains reasonably similar except for the changes in magnitude. It appears that the maximum skin friction in the valley occurs at $z/S = 0$, which then decreases near the vicinity of the ridge. This observation is also consistent with the DNS results of Hwang and Lee (2018) for the ridges of smaller widths with large spanwise spacings. The mean flow topology and the corresponding skin-friction distribution presented in figure 5.2 show a good correlation, especially for the cases X2HS1 to X2HS4. In fact, regions of constant skin friction are accompanied with a locally homogeneous mean flow (HMP), while regions of high gradient in the skin friction are associated with strong mean flow heterogeneity (LMP and HMP boundaries).

The topology of the mean flow starts to exhibit differences for the case of X2HS5 and changes drastically for X2HS6. The LMPs appear to widen for X2HS5 above the ridge, while the HMPs are narrower in the valley. This is accompanied by an increase in skin friction above the ridge when compared to X2HS4, while the average skin friction in the valley decreases compared to X2HS4. In the case of X2HS6, the increase of the ridge width has led to a reorganization of the flow topology, clearly showing a swap in the locations of the HMPs and the LMPs. This rearrangement in the mean flow has also

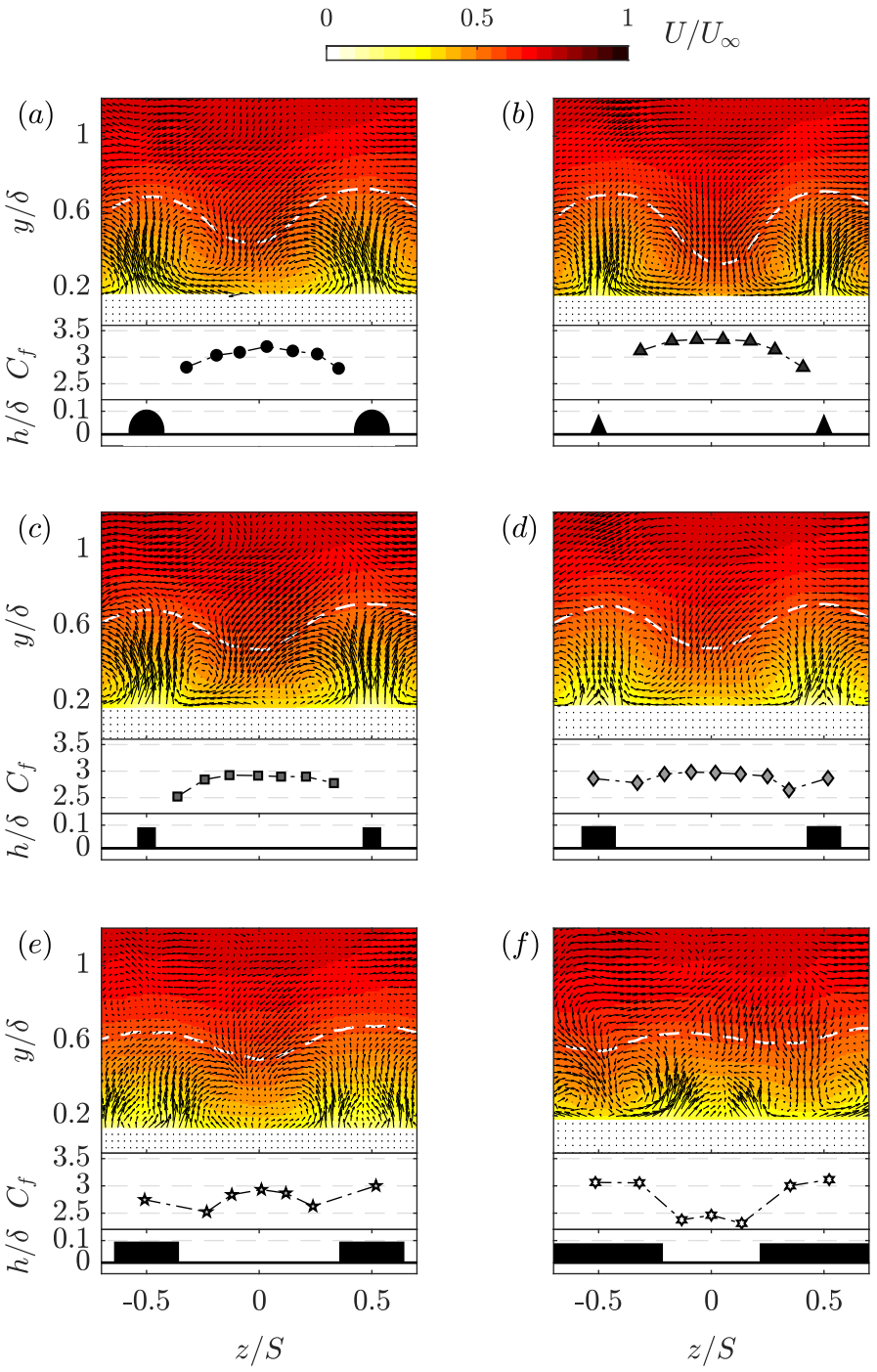

Figure 5.2: Contour maps of the normalised mean streamwise velocity and the spanwise distribution of the skin-friction coefficient at $Re_x = 4 \times 10^6$. (*a*): X2HS1, (*b*): X2HS2, (*c*): X2HS3, (*d*): X2HS4, (*e*): X2HS5, (*f*): X2HS6. The cross-sections of the roughness geometries are included at the bottom of the figures to scale for reference. The white dashed line represents the velocity contour level $U = 0.9U_\infty$. The mean in-plane velocity vector plot V and W are superimposed to highlight the vortical structures.

impacted the spanwise distribution of the skin-friction coefficient, as higher skin friction is now recorded above the ridge and a reduction in skin friction is observed in the valley, causing the local drag reduction. This can be explained by an increase in the viscous blockage caused by the ridge side wall boundary layers interacting with one another. This seems to specifically occur when the ridges are made wide enough such that they start influencing the neighbouring ones. It is also of interest to point out that for X2HS5 and X2HS6 that the degree of spanwise mean flow heterogeneity is lower than that of the other cases. As it can be seen from figures 5.2(e) and (f), the spanwise variation in the mean velocity contour level $0.9U_\infty$ (or the levels seen beyond 0.6δ) is relatively weaker when compared with the rest of the cases.

The results shown in the figures 5.2(a–e) are all in agreement with the previous studies that showed the HMPs and LMPs to occur over recessed and elevated regions respectively (Nezu and Nakagawa 1984; Colombini 1993; Wang and Cheng 2006; Vanderwel and Ganapathisubramani 2015; Medjnoun et al. 2018; Hwang and Lee 2018). However, the result shown in figure 5.2(f) seems more to line up with the results of Barros and Christensen (2014), Yang and Anderson (2017) and Awasthi and Anderson (2018). These findings indicate that for ridge-type heterogeneous surfaces with $S/\delta \sim \mathcal{O}(1)$, both scenarios can occur. Nonetheless, these differences in observations are likely to stem from an additional length scale at play besides S/δ. This leads us to further question how are these observed differences related to the characteristics of the large-scale secondary flows.

5.3 Effect on the upwash and downwash of the secondary flows

The effect of surface conditions on the upwash/downwash motions is shown in the mean wall-normal velocity component in figure 5.3. This component is of relevance since it directly assess quantitatively and qualitatively the effect of ridge geometry on the upwash and downwash motions, besides being a constitutive component of the streamwise vorticity. Figure 5.3 shows the mean wall-normal velocity maps for five cases out of six (X2HS5 is omitted for brevity) in the left panel, while contour levels of the ridge zoomed-in are presented to the right. These maps clearly illustrate both the effect of shape and width on the magnitude and distribution of the upwash/downwash motions. The top three maps (left and right) indicate the presence of three different ways of upwash motions that depend on shape. For X2HS1, the strongest upwash point seems to occur at about $2h$, whereas for X2HS2 and X2HS3 the strongest upwash points seem to be fixed very close the ridge corner(s), with similar attributes to that of an external flow over a smooth corner chine (Moinuddin et al., 2004).

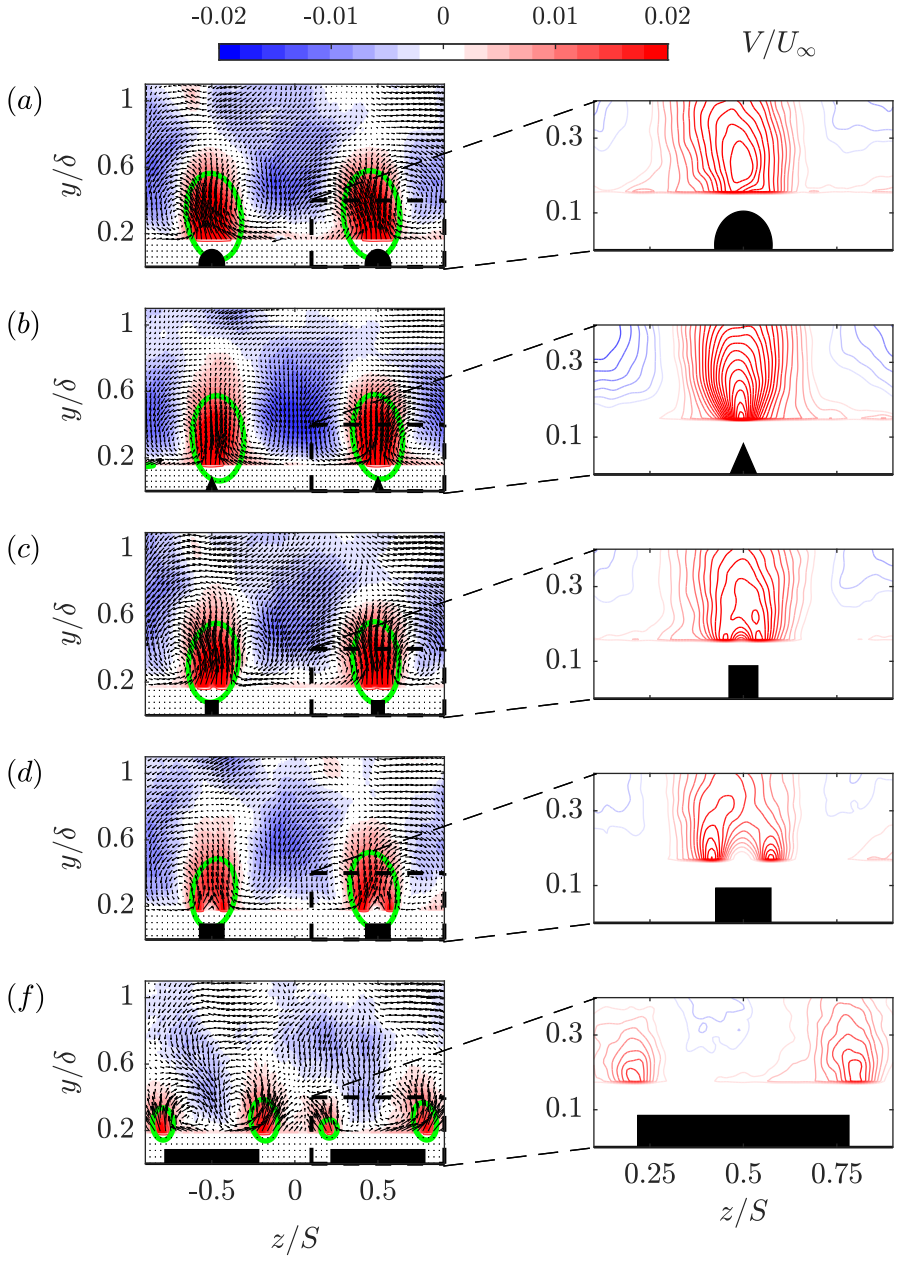

Figure 5.3: Effect of the roughness geometry on the topology of the mean vertical velocity component (left panel) with a zoom-in of the upwash region (right panel). (a): X2HS1, (b): X2HS2, (c): X2HS3, (d): X2HS4, (e): X2HS6. The mean in-plane velocity vector plot V and W are superimposed to highlight the vortical structures. The green contour level represents $V = 1\%$ of U_∞).

Figure 5.3 indicates both the magnitude and distribution of upwash can be related to the cross-section (curvature) of the ridge. X2HS2, which shows the most noticeable upwash, has its side walls in a configuration that promotes merging of the flow being deflected to make up a strong single upwash region. Whereas the convex nature of the cross-section in HS1 and the presence of a finite width between the two vertical side walls of HS3 can create more resistance to the flow which is moving radially towards the centre of the ridge, resulting in a reduction in the strength of the upwash motion. Other studies have also shown that the deflection of the spanwise motions due to the resistance created by the surface elevations is detrimental in the process of the secondary flow generation (Goldstein and Tuan 1998; Wang and Cheng 2006; Hwang and Lee 2018).

For the width effect cases, we observe that the upwash regions for X2HS4 and X2HS6 become more distinct, however tend to decrease in strength. This is further emphasized by looking at the ellipsoid at a matched contour level across cases (V = 1% U_∞). The contour level seems to encapsulate a relatively larger area for X2HS1 to X2HS3, then starts decreasing for wider ridges. This eventually ends up in a formation of two distinct lumps of upwash regions over a single ridge. It follows that these distinct upwash regions start interacting with the neighbouring ones to eventually end up forming a new coherent upwash region, leading to the swap in the LMP and HMP locations observed in figure 5.2(f). It is also important to point out that if wider ridges were to be used ($W_v \ll h$), these upwash/downwash motions would essentially die out, as the surface will recover homogeneity. Given the changes observed in the mean wall-normal velocity component due to the different types of ridges, it is essential to also look at how the secondary motions are distributed in these flows.

Following the aforementioned changes observed in the mean flow topology, proportional changes in the generated streamwise vorticity are to be expected. The identification of these streamwise time-averaged vortices was achieved through the determination of the vorticity-signed swirling strength λ_{ci}. The results are shown in figure 5.4 and indicate large-scale secondary flows associated with the different heterogeneous surfaces. Consistent with previous studies, these secondary flows consist of a pair of counter-rotating vortices formed on the top of either sides of the surface elevations. However, distinctive characteristics are shown across cases, both related to magnitude and distribution of these large-scale vortices. Globally, the spatial extent of λ_{ci} for the X2HS1–X2HS3 cases are qualitatively similar, although their magnitude seems to be affected by the ridge geometry. However, remarkable differences are highlighted for the cases X2HS4–X2HS6. In fact, changes in the streamwise vorticity start to occur; as the ridges become wider for a fixed S/δ, a pair of new small counter-rotating vortices of opposite sign is visible above the ridge. Similar additional vortices were also observed by Vanderwel and Ganapathisubramani (2015) but it was speculated that these could have been caused by the presence of small pins on the top of their LEGO brick roughness.

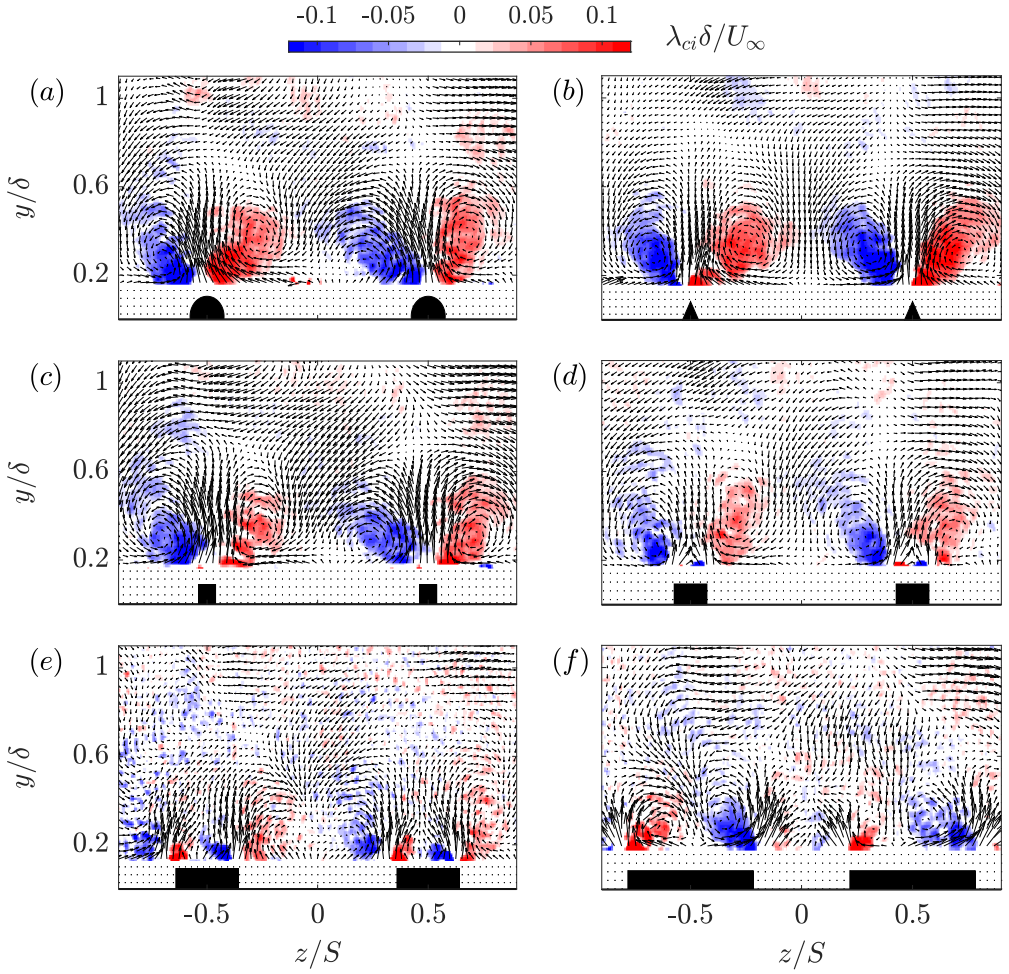

Figure 5.4: Effect of the heterogeneous surfaces on the normalised vorticity-signed swirling strength. (*a*): X2HS1, (*b*): X2HS2, (*c*): X2HS3, (*d*): X2HS4, (*e*): X2HS5, (*f*): X2HS6. The mean in-plane velocity vector plot V and W are superimposed to highlight the vortical structures on top of the swirling motions.

In a more recent study by Vanderwel et al. (2019) along with the DNS of Hwang and Lee (2018), these were reported to exist even for a smooth flat ridge, identical to the X2HS4–X2HS6 cases. The results are similar from both the present experiment and the DNS, and these "tertiary" flows are shown to grow stronger for wider ridges, while a weakening of the secondary vortices is observed. This feature is believed to also be present for X2HS3 despite not evident from the map, as these tertiary flows are too small to be captured with the current measurement. As highlighted in figure 5.4, these secondary and tertiary motions appear to compete (especially for X2HS5) above the ridge, and are controlled by the valley width $(S-W)/\delta$ (also see the figures 8 and 9 of Hwang and Lee 2018).

It appears that in the vertical direction, the secondary flow propels the low-speed fluid above the ridge away from the wall, and brings the high-speed fluid from the free stream towards the valley. The tertiary flows on the other hand, attempt to bring the high-speed fluid from the free stream down to the ridge. This is accompanied with a radial motion

from the tertiary flow that pushes the low-speed fluid above ridge towards the valley. Similarly in the spanwise direction, the secondary flow drives the high-speed fluid from the valley towards to ridges, opposing the tertiary motions. Beyond a given width, the extent of the streamwise vorticity changes due to an imbalance in favour of the tertiary flow which overcomes the secondary motion. The secondary motion continues to weaken leading to the observed swap of the LMPs and the HMPs locations. At this stage, the tertiary motion becomes the dominant feature in the cross-plane and therefore can be considered as a "new" secondary motion. This phenomenon can only take place for heterogeneous surfaces whose ridges allow the generation of two distinct upwash regions (for example rectangular shapes). In fact, it is difficult to imagine this phenomenon occurring for X2HS1 and X2HS2 regardless of their widths.

5.4 Relation between the wall shear stress, secondary flows and surface geometry

It is reasonable following the above observations to investigate a potential correlation between the surface heterogeneity, the magnitude of the secondary motions as well as the amount of drag caused by these surfaces. While it can be straightforward to find a metric to quantify the strength of the secondary motions (cross-flow kinetic energy or streamwise circulation), it is less clear which parameters should be used to characterise the surface geometry. For homogeneous rough surfaces, there are abundant surface parameters in the literature that are used to correlate the surface and aerodynamic properties of the flow (see the review by Flack and Schultz 2010). Whether it is randomly arranged, highly ordered or irregularly distributed rough surface, it can have strong dependence on the amplitude, spacing, density, slope or directionality among other parameters. There is clearly no consensus for a generic formula that will eventually represent all the surfaces.

It has been suggested that for secondary motion producing surfaces, the spanwise wavelength scaled with the dominant length scale of the flow (S/δ) is a good parameter (Vanderwel and Ganapathisubramani 2015; Yang and Anderson 2017; Chung et al. 2018; Chan et al. 2018). It was also argued that for the ridge-type heterogeneous surfaces, the valley width $(S-W)/\delta$ is important as it can substantially increase or reduce the strength of the secondary motions (Hwang and Lee, 2018). Similarly, for the strip-type heterogeneity, Willingham et al. (2014) have shown that the high-roughness width can either increase or decrease the intensity of the upwash/downwash motions by influencing the strength of the transverse mixing. In the present study, most of these scaling parameters would fail to capture the trends exhibited by the secondary flow. In fact, with S/δ being constant throughout all the cases, $(S-W)/\delta$ constant for the X2HS2–X2HS4 cases and the effective slope argument being constant for the X2HS3–X2HS6 cases, we

need to adopt a different parametrisation since the previous ones cannot adequately represent all these flow changes simultaneously.

The relations between the strength of these secondary flows and both the surface condition and the spanwise-averaged wall shear stress are presented in figure 5.5. Figures 5.5(a) and (b) quantify the variation in the streamwise circulation Γ^* and the skin friction C_f^* produced by these surfaces at the valley (since this estimate is available for the different test cases) with respect to the surface heterogeneity parameter ξ. Lastly, figure 5.5(c) shows the variation of C_f^* with respect to Γ^*. The quantities Γ^* and ξ which are tabulated in the table 5.1 are defined as

$$\Gamma = \int_{0.2\delta}^{\delta} \int_{-S/2}^{S/2} |\Omega_x| dz dy, \tag{5.2}$$

$$\xi = \frac{A_v}{A_p}, \qquad \text{where} \begin{cases} A_v = \int_{-S/2}^{S/2} \sqrt{\left(1 + (\frac{\partial h}{\partial z})^2\right)} dz, \text{for } h \leq \overline{h}, \\ A_p = \int_{-S/2}^{S/2} \sqrt{\left(1 + (\frac{\partial h}{\partial z})^2\right)} dz, \text{for } h > \overline{h}, \end{cases} \tag{5.3}$$

with $\Gamma^* = \Gamma/(\delta U_\infty)$ representing the normalised circulation of the streamwise vorticity Ω_x. In this study, Γ^* essentially quantifies the amount of streamwise vorticity produced in the outer layer of the turbulent boundary layer (above 0.2δ). On the other hand, ξ represents an attempt to parametrise the surface using a ratio of the recessed (valleys) and elevated (peaks) wetted areas. Since the surfaces are streamwise homogeneous, only the perimeters are considered in this study, and are defined as recessed (A_v) and elevated (A_p) areas whenever below or above the mean roughness height $\overline{h}$, respectively. As shown in figures 5.5(a) and (b), both the amount of streamwise vorticity and frictional drag are affected by these heterogeneous surfaces, despite them having the same S/δ. This result provides a justification for this surface parametrisation since both width as well as shape of the ridges are captured by ξ.

In figure 5.5(a), the streamwise circulation is shown to vary almost linearly within the range of ξ tested herein. If we consider the asymptotic limits of ξ, two behaviours are expected to take place: (i) for $\xi \to 0$ the secondary flows are expected to be small enough such that they are confined in the roughness sublayer and the flow will essentially recover homogeneity in the mean and turbulent sense ($\Gamma^* \to 0$). This is the limit where the surface is homogeneous. (ii) for $\xi \to \infty$, this can be thought of as a transitional surface that will result in localised but large secondary flows over/near the ridges, while further away from them, the flow is expected to remain homogeneous. In this case, the integrated circulation $\Gamma^* \to \Gamma^*_\infty$. Between these two limits, a third region can be identified as $a < \xi < b$, where a and b representing the lower and upper limits which translates to strong secondary flows with possible bifurcations to tertiary or even quaternary flows depending on the ridge geometry (Hwang and Lee, 2018). This results

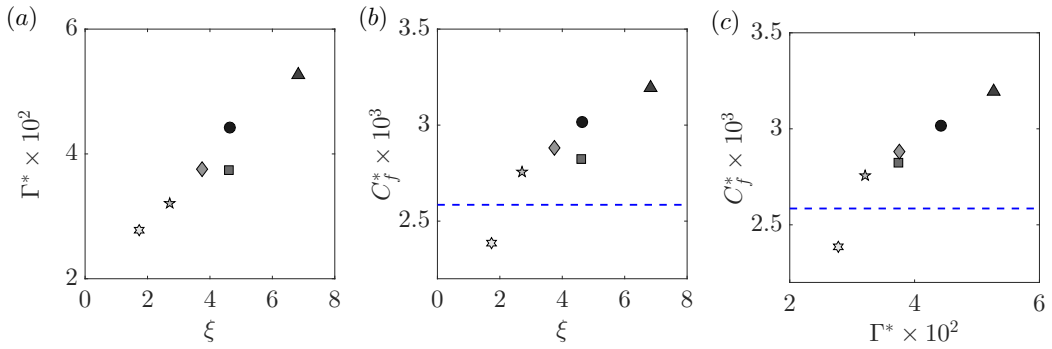

Figure 5.5: (*a*) Variation of the normalised compensated circulation Γ^* and (*b*) the valley spanwise-averaged skin-friction coefficient with respect to the surface parameter ξ. (*c*) The effect of the secondary flow circulation on the drag experienced at the valley. The blue dashed-line represents the smooth-wall skin-friction coefficient at an equivalent Re_x. See table 5.1 for the symbol legend.

in a highly three-dimensional flow which leads to the observed increased circulation Γ^* and drag. These observations are also in line with the study carried out by Yang and Anderson (2017), which provided similar evidence using a comprehensive range of values of the ridge spanwise spacing normalised with the channel half-height. Their LES results revealed that the spanwise spacing scaling indicates when the flow is expected to become homogeneous, heterogeneous or transitional supporting the idea of existence of three distinct regimes. In their study, these bands were termed roughness, intermediate and topography for homogeneous, heterogeneous and transitional respectively. Similar observations have also been made clear for the alternating high and low shear stress heterogeneity with the recent direct numerical simulations of Chung et al. (2018).

Furthermore, figure 5.5(b) shows that the local (valley spanwise-averaged) drag increases with increasing ξ. While a drag reduction is observed for X2HS6, C_f^* increases albeit with a lower rate when increasing ξ. For $\xi \to 0$, the valley skin friction C_f^* is naturally expected to tend to 0. However, if we considered the total drag C_F, it might be similar to the homogeneous case (or higher), which in this case is highlighted by the blue dashed-line. It is interesting to note that it might be possible to find a surface geometry that leads to an optimal secondary flow condition that would reduce the spanwise-averaged wall shear stress. Further studies are necessary to examine the feasibility of such surfaces and is beyond the scope of the present work. If $\xi \to \infty$, the skin friction is also expected to return to the homogeneous case at some point since the secondary motions will be significantly localised. However, how/when this would happen is also open for further exploration. Overall, it is possible to imply that changes in streamwise circulation induce proportional changes in the wall shear stress as demonstrated in figure 5.5(c). It essentially reveals that a possible linearity can exist for strong/large secondary flow cases, with an increase in the streamwise circulation leading to a proportional increase in the wall shear stress.

5.5 Effect of surface heterogeneity on the turbulence properties

The impact of the surface heterogeneity on the turbulence organisation is further analysed using a triple decomposition performed on the three component velocity vector in the cross-plane. This concept has been well documented and widely used to assess flows presenting spatial inhomogeneities (Reynolds and Hussain 1972; Raupach and Shaw 1982; Nikora et al. 2007). In this framework, the velocity field can be expressed as

$$u_i(y,z,t) = U(y) + \tilde{u}(y,z) + u(y,z,t), \tag{5.4}$$

where u_i is the instantaneous velocity field measured at a fixed streamwise location, $U(y)$ is the spatial- and temporal-averaged velocity profile, $\tilde{u}(y,z)$ is the spatial deviation field independent of time and $u(y,z,t)$ is the time fluctuating part from the Reynolds double decomposition. This decomposition allows us to quantify the amount of stresses arising from the mean flow heterogeneity, which contribute to the total stresses as form-induced (dispersive) stresses. In the case of strong spatial heterogeneities, these dispersive stresses can play a major role in the transport of momentum flux, which can impact the organisation of the turbulent boundary layer structure (Türk et al. 2014; Meyers et al. 2019).

Comparative maps of the turbulent, dispersive and total shear stresses denoted $\overline{uv}$, $\overline{\tilde{u}\tilde{v}}$ and $\overline{\tau_{xy}}$ respectively are presented in figure 5.6 (in columns), for different cases (in rows). As expected, the dispersive stresses are not negligible with respect to the turbulent ones. In fact, they appear to be non-zero for nearly two thirds of the extent of the boundary layer thickness with varying intensity along the spanwise direction (shown in the second column from the left of figure 5.6). The patterns of the turbulent and dispersive shear stresses do not show particular resemblance. In fact, while the overall distribution of $\overline{uv}$ seems to follow a similar wavy character as the mean flow, $\overline{\tilde{u}\tilde{v}}$ on the other hand appears to be more localised. The dispersive shear stress is shown to have high intensity above the surface elevation (especially near the ridge edges) as opposed to a weaker magnitude recorded at the valley. Away from the ridges, $\overline{\tilde{u}\tilde{v}}$ is shown to span nearly half of the valley extent with highest intensities being recorded at nearly 0.3δ from the wall. Nevertheless, the dispersive shear stress is shown to vanish between the peaks and valleys, whose regions are characterised by enhanced spanwise and weak wall-normal motions. These observations appear to mainly apply for the cases X2HS1–X2HS4. This is in contrast with X2HS5 and X2HS6, which were shown previously to be the least heterogeneous cases. As illustrated in middle figures 5.6(e) and (f), $\overline{\tilde{u}\tilde{v}}$ is observed to reduce in spatial extent and strength, where only a smaller dispersive shear stress remains above the ridges especially for X2HS6.

For $\overline{uv}$, a relatively weaker magnitude of the stress is observed at the valley in comparison to the ridge, with an overall distribution being similarly modulated as the mean flow. We can also observe from figure 5.6 that despite the different ridge geometries for the cases X2HS1–X2HS4, the turbulent shear stress remains globally similar between cases. This observation can perhaps be explained by the fact that once these large-scale secondary motions are formed, changes in surface heterogeneities result only in variations of their strength, without necessarily affecting their spatial extent. This mostly leads to an increased dispersive component, while the turbulent shear stresses remain relatively unchanged. However this is believed to be only valid when a strong degree of heterogeneity exists. This is further substantiated from the total shear stress maps $\overline{\tau_{xy}}$ shown in the third column from the left of figure 5.6. They mainly show that for large-scale secondary flows, their resulting total stresses remain relatively unchanged and their increase in strength will only result in the rise of magnitude of $\overline{\tau_{xy}}$, without necessarily affecting its spatial distribution. These results are also true for the streamwise stress component which was left out for brevity.

The global behaviour of the dispersive shear stress is further examined using spanwise-averaging over a wavelength. This represents a quantification of the overall effect of the flow heterogeneity on the turbulent boundary layer. In figure 5.7, the contributions of the dispersive shear stresses to total stress are emphasized in figure 5.7(a), plotted in the diagnostic form ($\langle U/U_\infty \rangle$). Figure 5.7(b) highlights the variation of the peak of $\langle \widetilde{\overline{u}}\widetilde{\overline{v}} \rangle / \langle \overline{\tau_{xy}} \rangle$ with respect to the streamwise circulation Γ^*. Figure 5.7(c) on the other hand illustrates the wall-normal distribution of the spanwise-averaged total shear stress defined as

$$\underbrace{\langle \overline{\tau_{xy}} \rangle}_{\substack{\text{total}\\ \text{shear}\\ \text{stress}}} = \underbrace{\nu \frac{\partial \langle U \rangle}{\partial y}}_{\substack{\text{viscous}\\ \text{shear}\\ \text{stress}}} - \underbrace{\langle \overline{uv} \rangle}_{\substack{\text{turbulent}\\ \text{shear}\\ \text{stress}}} - \underbrace{\langle \tilde{u}\tilde{v} \rangle}_{\substack{\text{dispersive}\\ \text{shear}\\ \text{stress}}} , \tag{5.5}$$

which typically accounts for viscous, turbulent and dispersive shear stress contributions. However, it should be noted that the viscous contribution in the outer flow are negligibly small in comparison with the turbulent and dispersive contributions. As observed from figure 5.7(a), the dispersive stresses are shown to be significant in magnitude for a large extent of the boundary layer thickness. As opposed to classical homogeneous roughness where it is expected to see their contribution to be only important below the canopy, their effect is presently shown to be substantial even in the outer layer. In fact, these form-induced stresses contribute from 15% up to 55% of the total shear stress for the most heterogeneous case. It is additionally shown that at a given distance from the wall ($\langle U/U_\infty \rangle = 0.9$ or $y = 0.6\delta$), the dispersive stresses are shown to have nearly similar decay rates (specifically the cases X2HS1–X2HS4). This can be interpreted as a result of saturation in size of these large-scale secondary motions for a range of $a < \xi < b$, whereby small changes in ξ only enhance or weaken the strength of these secondary

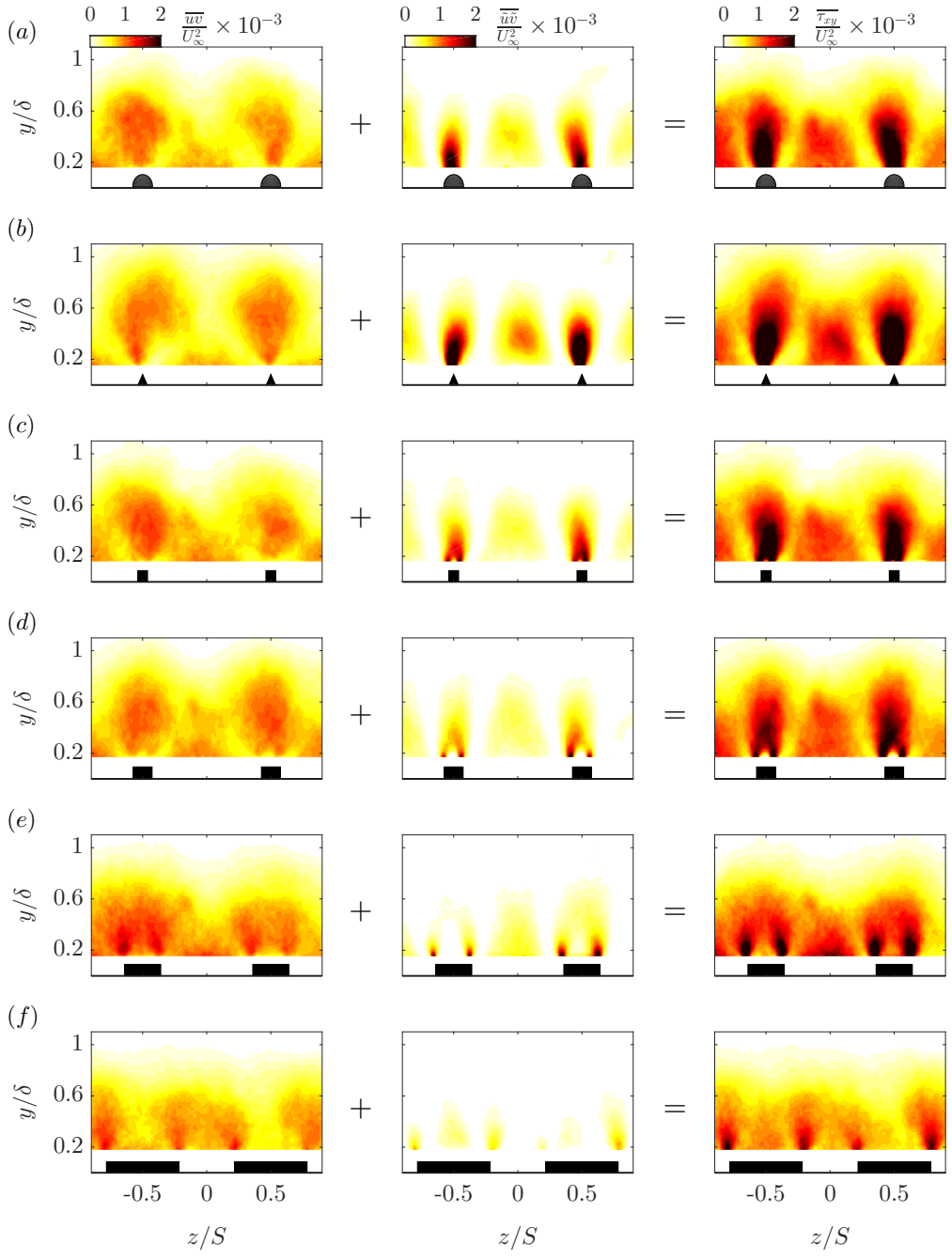

Figure 5.6: Effect of the different heterogeneous surfaces on the normalised (left panel) turbulent ($-\overline{uv}/U_\infty^2$), (middle panel) dispersive ($-\tilde{u}\tilde{v}/U_\infty^2$) and (right panel) total shear stress ($-\tau_{xy}/U_\infty^2$). (*a*): X2HS1, (*b*): X2HS2, (*c*): X2HS3, (*d*): X2HS4, (*e*): X2HS5 and (*f*): X2HS6.

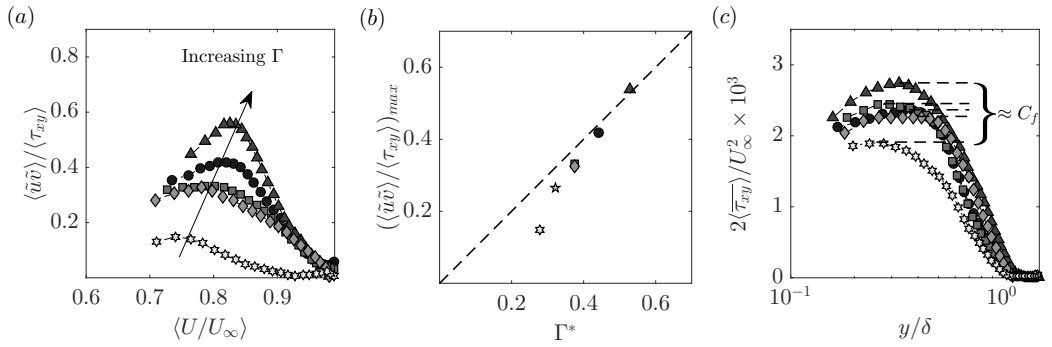

Figure 5.7: (*a*) Variation of the dispersive contribution to the total shear stress in the diagnostic form. (*b*) Variation of the peak of the dispersive contribution normalised with the total shear-stress with respect to the secondary flow circulation, with the dashed line representing a 45° slope. (*c*) Wall-normal distribution of the normalised total shear-stress profiles. See table 5.1 for the symbol legend.

motions without necessarily affecting their spatial extent. This further supports the results shown in the figures 5.4 and 5.5 for X2HS1–X2HS4, which can be considered to be in a "fully" grown heterogeneous regime. As opposed to X2HS5 and X2HS6, they were shown to have both weaker and smaller secondary flows, hence their small impact on the primary flow.

Figure 5.7(a) also underlines that the maximum peak in $\langle \widetilde{\overline{u}}\widetilde{\overline{v}} \rangle / \langle \overline{\tau_{xy}} \rangle$ increases both in magnitude and relative height (expressed by $\langle U/U_\infty \rangle$) when increasing the streamwise circulation, however the peak remains constant when plotted in y/δ. This means that the location of the secondary flows remains unaffected, and the increase in circulation only results in a larger mixing causing a fuller turbulent boundary layer flow. In figure 5.7(b), the variation of $\langle \widetilde{\overline{u}}\widetilde{\overline{v}} \rangle / \langle \overline{\tau_{xy}} \rangle_{max}$ with respect to Γ^* is emphasized, and is shown to rapidly increase for X2HS5 and X2HS6 while almost linearly varies for X2HS1 to X2HS4. This result provides further support to the previous interpretation, that the secondary flow formation can undergo different regimes.

Moreover, figure 5.7(c) illustrates the variation of the total shear stress computed using equation 5.5. The results indicate that overall, the plateau extent and magnitude have been affected by the presence of these large-scale secondary flows. As expected, the magnitude of the plateau increases with increasing Γ^*, which translates to higher wall drag experienced by the surface. Surprisingly, the plateau extent shortens for large Γ^* and lengthens for smaller Γ^*. This behaviour is caused by the dispersive stress contributions which are amplified by these large-scale secondary flows. In fact, this is more evident when comparing the turbulent shear stress maps to the dispersive ones as shown in figure 5.6. The dispersive stress contributions seem to be accentuated near the core of the secondary flows ($y \approx 0.3\delta$), while diminish closer to the wall, leading to the presence of the observed peak in figure 5.7(a). The turbulent stresses on the other hand seem to have a nearly constant contribution up to 50% of the boundary layer thickness

when spanwise-averaged (not shown for brevity). Therefore, the presence of a peak instead of a classical plateau in $\langle\overline{\tau_{xy}}\rangle$ is considered to be a consequence of the increased lateral motions due to secondary flows which lead to higher momentum transport. These results are also in agreement with the recent studies that assessed the contributions of the dispersive stresses (Chan et al. 2018; Vanderwel et al. 2019; Meyers et al. 2019). They found that these form-induced stresses are prominent within the canopy but can remarkably increase spatially depending of the surface heterogeneity length scale. For a certain range of spanwise wavelengths, the turbulent stresses are shown to exhibit strong spanwise gradients which lead to the added dispersive stresses that can extend up two thirds of the flow.

The impact of the secondary flows on the outer-layer similarity is examined in figure 5.8. Figure 5.8(a) shows the spanwise-averaged mean velocity profiles in defect form scaled with the friction velocity taken from the total shear stress plateau. On the other hand, figure 5.8(b) highlights the spanwise-averaged streamwise turbulence intensity profiles plotted in the diagnostic form introduced by Alfredsson et al. (2011). There is a marginal lack of collapse in the velocity deficit for all the different surfaces when compared to the smooth-wall data. The absence of collapse extends up to $y = 0.6\delta$, whose recovery seems to occur when the dispersive stresses decay faster as shown in figure 5.6. The turbulence intensity profiles are even more affected by the presence of these large secondary motions, with a recovery only occurring at the edge of the boundary layer (not shown here for brevity). The above observations are consistent with previous results both from the ridge-type and the roughness-type studies by Chan et al. (2018) and Chung et al. (2018) respectively. They essentially showed for spanwise wavelengths comparable to the dominant length scale of the flow, the secondary flows occupy a large portion of the primary flow, leading to strong dispersive stresses (extended roughness sublayer) which results in the breakdown of both global and local outer-layer similarity.

A good collapse is observed for the variance profiles as shown in figure 5.8(b), not only between the cases, but also with the smooth-wall profile. This suggest that regardless of the changes in the secondary flow circulation, the streamwise turbulence intensity along with the mean flow change proportionally in the outer region. Moreover, the collapse of the profiles with the smooth-wall irrespective of a non-zero roughness function ΔU^+ (representative of the drag changes shown in figure 5.1) does not seem to be captured in the diagnostic plot. This is inconsistent with the conclusions of Castro et al. (2013) who demonstrated that increasing ΔU^+ leads to a higher slope in u/U till reaching the fully-rough trend (represented by the red-dashed line in figure 5.8(b)). One possible reason for the current behaviour is that the value of the roughness function is small ($\Delta U^+ \leq 4$). Additionally as discussed in section 5.2, the absence of form drag contributions to ΔU^+ due to lack of rough protrusions can inhibit the increase of streamwise turbulence levels relative to the mean flow. Similar results are also reported in our previous study (chapter 4)regarding local profiles across the spanwise direction.

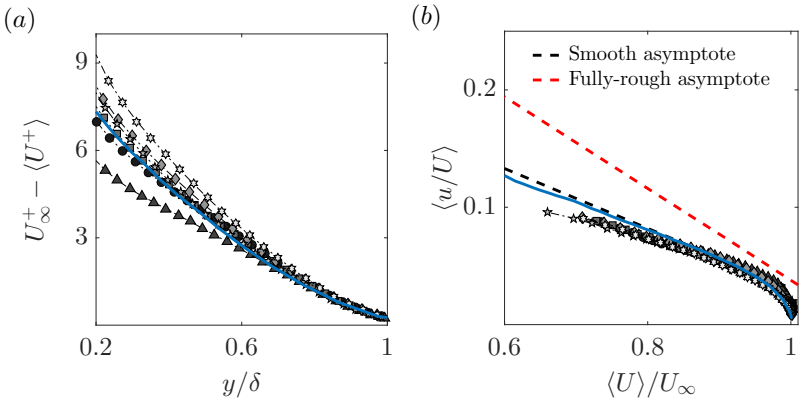

Figure 5.8: Effect of the different heterogeneous surfaces on (a) spanwise-averaged mean velocity profiles in the defect form normalised with the friction velocity determined from the total shear stress. (b) Outer scaling of spanwise-averaged streamwise turbulence intensity in the diagnostic-plot form. The blue solid-line represents the smooth-wall data from Medjnoun et al. (2018). See table 5.1 for the symbol legend.

5.6 Effect on the coherent structures in the outer region

To further investigate the influence of the surface heterogeneity on the characteristics of the turbulence structures, the two-point correlation function of the velocity fluctuations is examined. This allows qualitative and quantitative characterisation of the spatial structures at different critical locations such as the high- and low- momentum pathways that characterise this flow (Wu and Christensen, 2010; Yang and Anderson, 2017; Bai et al., 2018; Kevin et al., 2019). The two-point correlation coefficient tensor $R_{u_i u_j}$ in the (y, z)-plane is defined as,

$$R_{u_i u_j}(y_{ref}, z_{ref}) = \frac{\overline{u_i(y_{ref}, z_{ref}) u_j(y, z)}}{\sigma_{u_i}(y_{ref}, z_{ref}) \sigma_{u_j}(y, z)}, \tag{5.6}$$

where y_{ref} and z_{ref} are the reference wall-normal and spanwise locations at which the correlation is examined. $\sigma_{u_i}(y_{ref}, z_{ref})$ is the standard deviation of u_i at y_{ref} and z_{ref} and $\sigma_{u_j}(y, z)$ is the standard deviation of u_j in the (y, z)-plane. Figure 5.9 illustrates the two-dimensional autocorrelation maps of the streamwise velocity fluctuations R_{uu} at $y/\delta = 0.4$ determined at three different spanwise reference locations (z/S = -0.5, -0.25 and 0 from left to right panels) for four different heterogeneous surfaces (X2HS1, X2HS2, X2HS4 and X2HS6). The wall-normal location was chosen to show representative existence or lack of structural similarity in the outer layer while the spanwise locations are chosen to investigate structural changes in the spanwise direction.

Significant changes in the spatial coherence in both the wall-normal and spanwise directions are observed for the different locations. The correlations maps indicate that at the LMPs (left panel of figure 5.9), the structures are skewed in the wall-normal

direction, but symmetric in the spanwise direction. They also highlight the emergence of negatively correlated regions shown as the black dashed contour flanking the either sides of the ridges. Their spanwise extents appear to extend away from the wall while they shrink when closer to the ridge. In contrast, the structures observed at the HMPs show an opposite behaviour with a much larger spatial coherence near the wall (right panel of figure 5.9) as opposed to a narrower correlation away from the wall. Two negatively correlated regions exist in the spanwise direction with a larger distance away from their main lobe compared to the LMP structures. The asymmetric nature in the horizontal plane of these structures seems to link with the presence of the large-scale secondary motions. In fact, if we pick a point near the wall ($y = 0.2\delta$), strong inward radial motions are expected above the ridge whereas outward radial motions occur at the valley. Likewise, at a location away from the wall ($y = 0.6\delta$), the opposite behaviour is expected to occur. Hence the non-symmetrical aspect of the coherent structures above the peaks and valleys.

The correlation maps in the mid-plane between HMPs and LMPs (middle panel in 5.9) indicates that both their spatial extent as well as their orientations are affected. A significant increase in the coherence of the structures accompanied with a substantial tilt is shown through the black contour levels, along with the rise of two non-symmetrical negative correlation regions. This inclination is believed to be caused by the strong radial motions induced by the presence of these large-scale secondary flows, which result in the spanwise mean shear flow. In fact, their inclination angles seem to line up reasonably well with the normal of the streamwise velocity maps (as shown in the figure 5.2). This is more evident with the observation made for the X2HS6 case which showed a reversal in the direction of the tilt similar to the swap in the LMP and HMP locations reported for the same surface. Qualitative similarities across cases are observed when comparing the extent of the coherent structure at the peaks and valleys as shown in figure 5.9(m) and (o). The exception remains the X2HS6 case, where the turbulence structure seems to have been altered due to the swap of the LMP and HMP locations.

Quantitative changes in the turbulence structures (coherence inclination angles and length scales) are computed from the R_{uu} map in the (y, z)-plane. This is done by fitting an ellipsoid to a given contour level (shown with a black solid-curve in figure 5.9 at $R_{uu} = 0.3$). The parameters of this fitted ellipse (red dashed-curve) include the two orthogonal axes with a major axis (shown in blue) and a minor axis (shown in green) representing the characteristic length scales in the wall-normal and spanwise directions. An overall length l_{xx} shown in figure 5.10(a) is estimated by taking the square root of the sum of the squares of the minor and major axes of the ellipse, while the inclination angle Φ is just the major axis clockwise rotation from the wall-normal direction as shown in figure 5.10(b). Both these values seems to have been affected by the surface heterogeneities. The length scale l_{xx} seems to grow between the high- and low-momentum pathways especially where the spanwise mean shear flow is the highest. This is accompanied by a

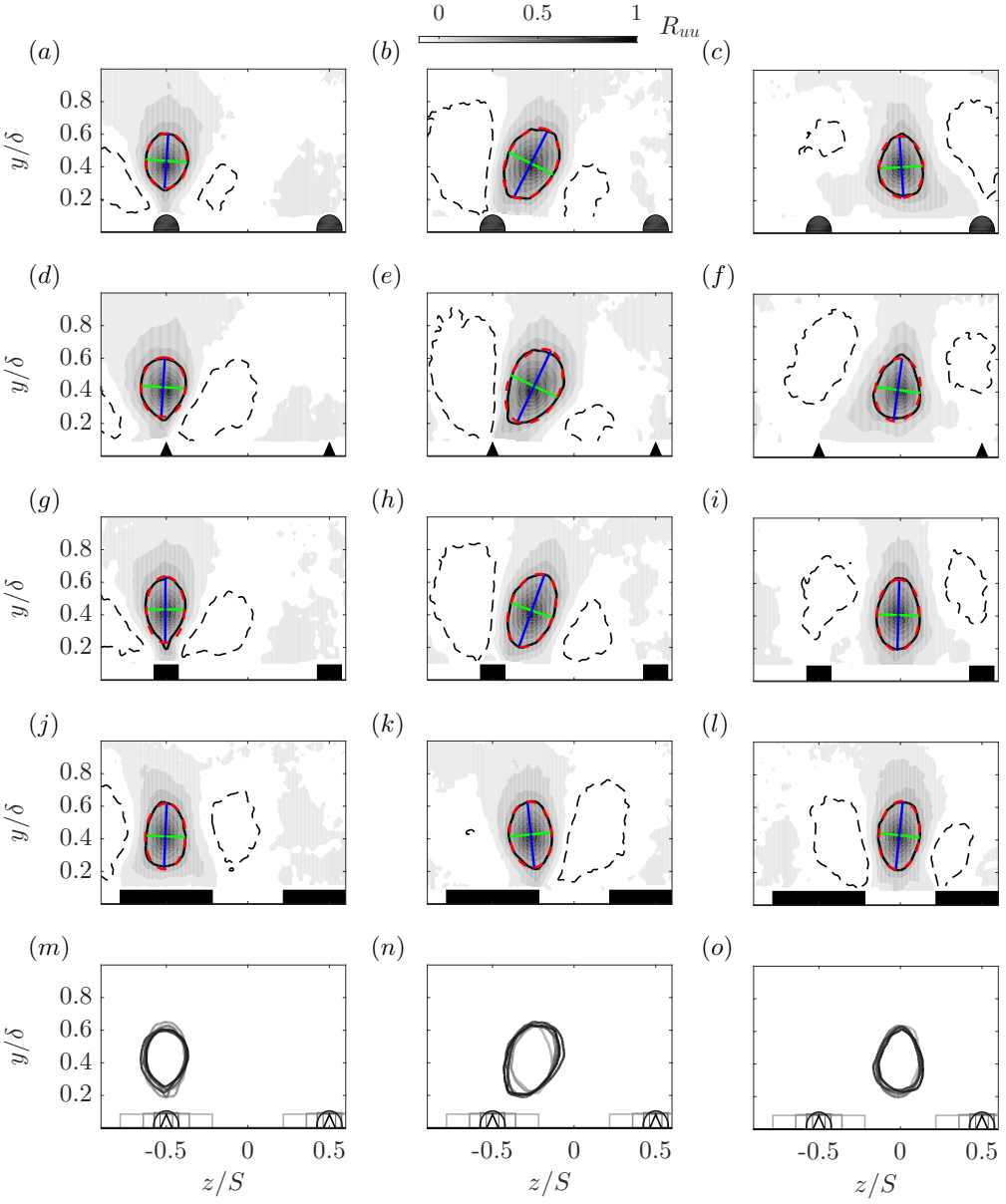

Figure 5.9: Spatial autocorrelation maps of the fluctuating streamwise velocity R_{uu} in the cross-plane at $y_{ref} = 0.4\delta$ over three spanwise locations: (left panel) peak, (middle panel) mid-peak-valley distance and (right panel) valley. (*a–c*): X2HS1, (*d–f*): X2HS2, (*g–h*): X2HS4, (*j–l*): X2HS6 and (*m–o*): a selected contour level of all the cases superimposed. The black contour level represent $R_{uu} = 0.3$. The corresponding ellipsoid fit is represented in red dashed contour with its major and minor axes in blue and green lines respectively. The dashed black contour level represents $R_{uu} = -0.1$.

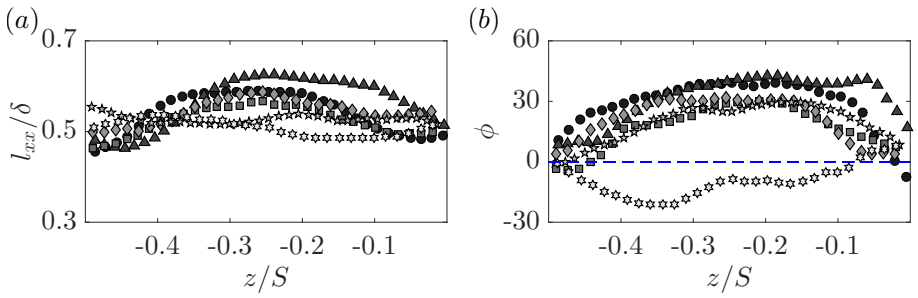

Figure 5.10: Spanwise variation of the (a) normalised autocorrelation length scale determined at $R_{uu} = 0.3$ and (b) the corresponding structure inclination subjected to different surface heterogeneities. Positive and negative angles above and below the blue dashed line referred to clockwise and anti-clockwise inclination of the structure. See table 5.1 for the symbol legend.

modification in the turbulence structure shapes which show elongated oblique coherence characterised by their inclination.

These observations are also in agreement with other recent studies over the strip-type surfaces from Bai et al. (2018) and Kevin et al. (2019). The results from the wall-parallel stereo-PIV performed in the log-region by Bai et al. (2018) revealed that near the surface discontinuity, the coherent structures presented a yawed coherence due to the lateral inflow. This region which is home to strong wall-normal vortices induces the high and low speed streaks to be arranged above the high roughness (HMPs) and low roughness (LMPs) respectively. This is furthermore supported by the study of Kevin et al. (2019) who investigated the characteristics of these coherent structures in multiple streamwise, spanwise as well as wall-parallel planes in the converging-diverging riblet roughness. They found that between the HMPs and LMPs, the region is home to an appearing "detached" coherent structure which is characterised by a tilt in the wall-normal and streamwise direction that enhances lateral momentum transfer. This is a further evidence that structural similarity has been altered by the secondary flows.

5.7 Effect on the wake intermittency

The turbulent/non-turbulent interface (TNTI) has been widely explored in many flows, such as in wakes, jets and turbulent boundary layers (Bisset et al. 2002; Westerweel et al. 2005; Laskari et al. 2018). The TNTI represents an instantaneous thin layer that isolates regions of turbulent motions from regions of the non-turbulent flow (Corrsin and Kistler, 1955). The interface is characterised by a simultaneous occurrence of small and large-scale processes termed as "nibbling" and "engulfment", representative of viscous and inertial mechanisms, inducing turbulence-free fluid entrainment towards the turbulent flow (Chauhan et al., 2014). In the presence of surface spanwise heterogeneity, both the inner and outer regions were shown to be affected by the large-scale

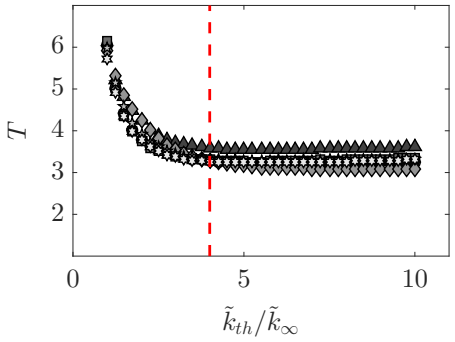

Figure 5.11: Effect of different threshold levels on the tortuosity parameter for the different heterogeneous surfaces. The vertical red dashed-line represents the selected threshold $\tilde{k}_{th}/\tilde{k}_{\infty} = 4$ for the TNTI analysis. See table 5.1 for the symbol legend.

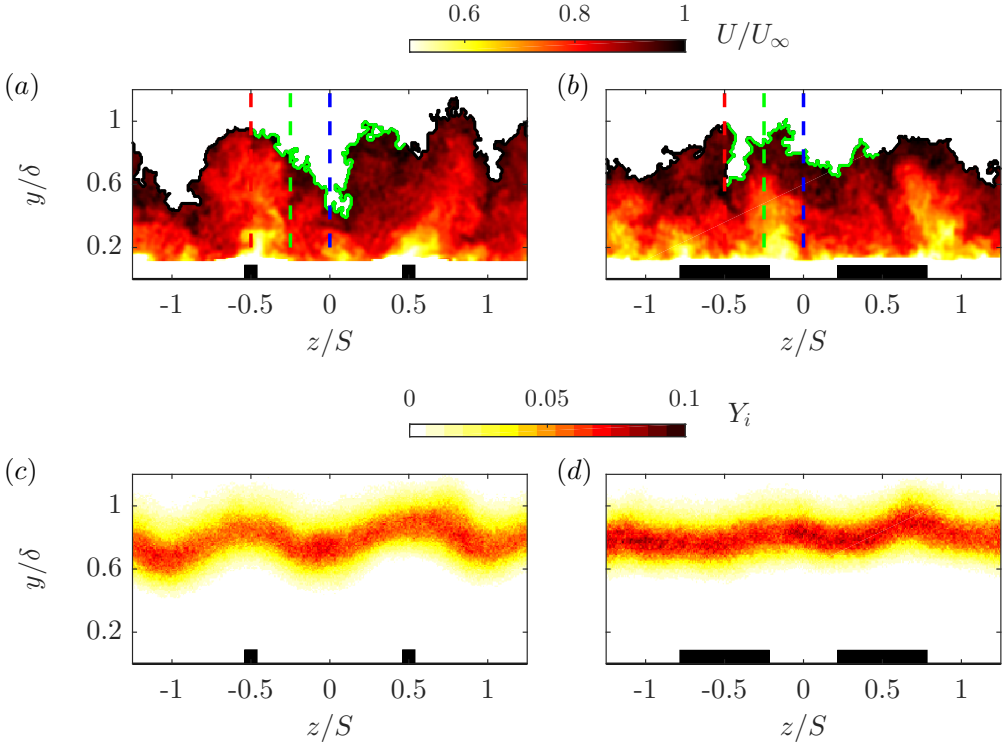

Figure 5.12: Example of the application of the turbulent kinetic energy deficit criterion to an instantaneous streamwise velocity map for (a) X2HS3 and (b) X2HS6. The turbulent/non-turbulent interface outline is highlighted with a black line. The arc-length used to determined the tortuosity in figure 5.11 is shown inside one wavelength in green. The colour-coded vertical dashed lines are the spanwise locations over which the local intermittency profiles are evaluated as shown in figure 5.13(a) and (b). (c) and (d) represent the ensemble averages of the spatial occurrence on the TNTI in the $(y-z)$-plane for X2HS3 and X2HS6 respectively.

secondary motions, which rearrange the structural organisation of the turbulence (Yang and Anderson 2017; Kevin et al. 2017; Bai et al. 2018; Kevin et al. 2019). Therefore, this rises the interrogation on how does the wake intermittency re-adapt to the structural changes observed before.

The interface detection method employed in this study is similar to that defined by Chauhan et al. (2014). The approach is based on a local turbulent kinetic energy deficit detector $\tilde{k}_{th}$, using a given threshold that separates the instantaneous flow into a turbulent and a non-turbulent flow. However, the threshold selection is shown to be specific to each experiment and can be influenced by the turbulence level in the free stream, the measurement systematic and statistical uncertainties. Consequently, in order to have a consistent way of defining suitable thresholds for the different cases, a variable T defined as the "tortuosity" is determined for different levels of thresholds. The tortuosity essentially represents the arc-length of the interface l_i within a given unit distance, herein defined as $T = l_i/S$. Figure 5.11 illustrates the variation of the tortuosity as a function of the threshold level $\tilde{k}_{th}$ normalised by the turbulent kinetic energy deficit in the free stream $\tilde{k}_{\infty}$. The results indicate that beyond a certain level, the tortuosity becomes constant irrespective of changes in the threshold level $\tilde{k}_{th}/\tilde{k}_{\infty}$. The value $\tilde{k}_{th}/\tilde{k}_{\infty} = 4$ was found to correspond to a reasonable threshold level that yields a consistent comparison between cases. In this case, $4\tilde{k}_{\infty}$ ranges between 0.12–0.25, which are between a factor one and two of the value used by Chauhan et al. (2014). However, as mentioned above, these values are not expected to remain constant from one experiment to another.

To demonstrate the effect of the surface heterogeneity on the interface, two examples for X2HS3 and X2HS6 are highlighted in figures 5.12(a) and (b) respectively. The TNTI is shown in figures 5.12(a) and (b) as the black contour delineating two distinct regions in the instantaneous streamwise velocity map; turbulence-free stream above and turbulent regions below the interface outline. The arc-length of the TNTI within a spanwise unit distance used to determine the tortuosity is highlighted in green. Figure 5.12(a) clearly indicates that substantial distortions are present at the interface outline, with alternating large-scale bulges and valleys above the elevated and recessed surfaces, respectively. This observation remains consistent for all the cases except X2HS6 as shown in figure 5.12(b), which showed the occurrence of the opposite behaviour.

In order to get a quantitative assessment of these differences, the TNTIs of all the snapshots are superimposed to obtain an ensemble average as illustrated in figures 5.12(c) and (d). As expected, the wall-normal location of the TNTI appears to undergo a similar periodicity as the mean flow in the spanwise direction, with alternating high and low TNTI locations above the elevated and recessed surface respectively. Furthermore, the changes observed in the mean and the turbulent characteristics for X2HS6 are also reflected in figure 5.12(d), which is characterised by a swapping of the high and low TNTI locations. The spanwise variation of the interface seems to have also a subtle

dependence on the strength of secondary flows. In fact, the maps of the TNTI height Y_i indicate that the peak-to-peak for X2HS3 is higher than that of X2HS6. However, this is not completely clear when the tortuosity of the interface is examined as shown in figure 5.11. It appears that the most tortuous interface is X2HS2, which was shown to be the most heterogeneous flow. Nevertheless, the rest of the cases seem to have relatively similar values of T which range between 3.2 and 3.6 for the different cases.

It is perhaps also interesting to point out that the values of T are in a reasonable agreement with the predicted value by Chauhan et al. (2014) for a smooth-wall turbulent boundary layer. They hypothesised that based on the fractal nature of the TNTI, its length in the spanwise direction is expected to be three times the distance where it sits on, similar to that in streamwise direction. In the present study, the induced cross-plane secondary motions caused by the surface heterogeneity have effectively altered the interface, hence the slightly larger values of the tortuosity. Similar findings have also been recently reported by Kevin et al. (2017), who observed strong spanwise waviness of the TNTI. Their analysis was based on the identification of "pockets" of turbulence-free fluid within the turbulent flow below the interface outline. They looked at both the spatial distribution of these non-turbulent pockets as well as their frequency of occurrence. They observed that their manifestation is two times more probable over the downwash regions due to large-scale free stream engulfment occurring close to the wall, in contrast to less recurrent pockets over the upwash regions which appeared far from the wall.

The intermittency γ indicates the proportion of time a flow is turbulent at a given point in the (y, z)-plane. Consequently, γ tends to 1 near the wall whereas tends to zero near the free stream. The local intermittency profiles are shown for three different spanwise locations for X2HS3 and X2HS6 in figures 5.13(a) and (b) respectively. The different colours highlight the three spanwise locations illustrated with vertical coloured dashed-lines in figures 5.12(a) and (b). The profiles indicate the intermittency to have a constant upper bound beyond which the flow remains statistically laminar, when the wall-normal distance is scaled with the local boundary layer thickness. On the other hand, the insets of figures 5.13(a) and (b) reveal that the lower bound changes according to the spanwise location. For example, figure 5.13(a) indicates that the intermittency extent is wider at the valley ($z/S = 0$ and -0.25) than over the ridge ($z/S =$ -0.5) which correspond to the downwash and upwash regions respectively. This result is in fact not surprising since the ridges give rise to high-turbulent fluxes, which are then advected vertically, causing the reduction in the wake intermittent activity at the upwash region. Conversely, the recessed regions are dominated by downwash motions transporting low-turbulent fluxes towards the near wall rendering the intermittent region larger. These results are shown to be valid for all the cases with the exception of X2HS6. This is demonstrated in figure 5.13(b) which highlights the occurrence of an opposite behaviour, where the profiles above the ridge appear to have an extended intermittent region,

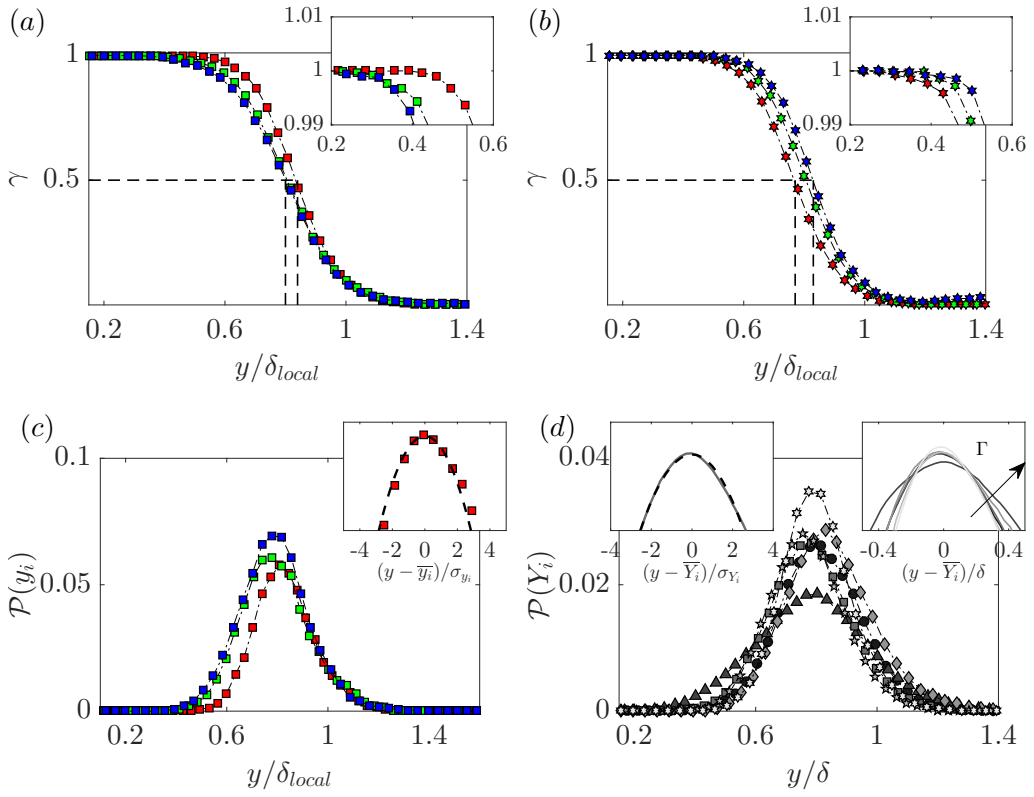

Figure 5.13: Wall-normal distribution of the local intermittency profiles γ for (a) X2HS3 and (b) X2HS6 at $z/S = -0.5, -0.25$ and 0 for the red, green and blue markers respectively. (c) The corresponding probability density function $\mathcal{P}(y_i)$ for X2HS3 with the inset comparing the profile at $z/S = -0.5$ (red squares) to a Gaussian distribution (dashed line) normalised with their variance. (d) The global probability density function of the TNTI $\mathcal{P}(Y_i)$ locations for the different cases. The left and right insets of (d) highlight the profile of X2HS3 (solid line) compared with a Gaussian distribution (dashed line) normalised by their variance, and the profiles of all the cases colour-coded as shown in table 5.1's symbol legend.

although the differences being weaker. These changes are also expected to take place since we previously observed the HMPs and LMPs to have swapped locations.

Finally, the probability density function of the local TNTIs, $\mathcal{P}(y_i)$ (estimated at selected spanwise locations), is examined in figure 5.13(c) for X2HS3. The profiles reveal that the local mean heights of the TNTI $\overline{y_i}$ vary marginally in the spanwise direction. This is also highlighted by the vertical and horizontal black dashed-lines which correspond to $\gamma = 0.5$ in figures 5.12(a) and (b). The structural modifications in the outer region also appear to have affected the Gaussian nature of the TNTIs, specifically at the LMP. This is illustrated in the inset of figure 5.13(c) which compares the local profile at the upwash region (red squares) against a Gaussian distribution (black dashed-line), which showed a degree of skewness towards to free stream. This observation, however, is only true in the local sense. In a global sense (for a full wavelength), the profiles are shown to remain Gaussian regardless of the surface heterogeneity. This is

depicted in figure 5.13(d) which inspects the global probability density function $\mathcal{P}(Y_i)$ across cases. Despite the differences in the mean TNTI height $\overline{Y_i}$ which ranges between $0.77 \leq \overline{Y_i}/\delta \leq 0.86$, the distributions appear to have good degree of symmetry. As a matter of fact, $\mathcal{P}(Y_i)$ for X2HS3 is presented in the left inset of figure 5.13(d), and shows an excellent degree of collapse with the Gaussian distribution (black dashed-line). This indicates, in spite of the presence of large-scale secondary flows, the Gaussian nature of the TNTI globally remains unaffected. The secondary flows are shown to mainly induce changes in the extent of the intermittent regions. The right inset of figure 5.13(d) displays that the TNTI extent becomes larger for cases that exhibit stronger secondary motions. This is shown by the changes in standard deviation of the interface which ranges between $0.11 \leq \sigma_{Y_i}/\delta \leq 0.19$ from the least to most heterogeneous case.

The results of the TNTI analysis is consistent with the observations of the wake strength parameter reported in chapter 4. They showed that the wake strength was affected by the spanwise heterogeneity of the surface, with high and low values above the valleys and ridges respectively. As indicated by Krug et al. (2017), the wake strength parameter stems from a combined effect of the velocity jumps in the uniform momentum zones and the jump across the TNTI. Therefore, the previously observed changes in the wake parameter are probably due to the changes in the intermittent activity across the span.

5.8 Summary

A turbulent boundary layer flow over smooth heterogeneous surfaces has been experimentally studied. We specifically looked at the influence of the different surface heterogeneities on the secondary flows that developed under these conditions. Oil-film interferometry along with stereo-PIV measurements allowed us to evaluate the impact of these heterogeneous surfaces on the skin friction, the mean and turbulent flow properties.

In the presence of ridge-type surface heterogeneity, the spanwise distribution of the skin friction varies as a consequence of the mean flow heterogeneity. As a result, strong spanwise skin friction gradients are observed, and are located near the regions of high spanwise mean shear. The average frictional drag was directly assessed and was shown to be both a function of Reynolds number as well as the surface heterogeneity. It is speculated that these surfaces do not allow the flow to transition to a 'fully" rough regime, as the roughness function is entirely driven by the viscous drag and has no form-drag due to lack of roughness protrusion.

The mean vertical velocity component emphasized the importance of both the ridge shape and width. It is shown that beyond a given value of width, a swap between the HMPs and LMPs can occur. For $(S - W)/\delta > 0.5$, the HMPs and LMPs were consistently shown to occur above the recessed and elevated regions of the surface. The

modifications were also evident in the streamwise vorticity highlighted by the swirling strength, revealing remarkable changes in the secondary flow structures. Strong secondary flows occurred above thin ridges when $(S - W)/\delta \approx \mathcal{O}(1)$, whose extent are shown to scale with the valley width, while their strength scale with the ridge curvature. For the rectangular ridges, a pair of new small counter-rotating vortices of opposed sign take place above the ridges forming a tertiary flow. For $(S - W)/\delta \leq 0.5$, an imbalance in favour of the tertiary flows occurs which take over the secondary motions, leading to the swap of the LMPs and the HMPs locations. The results also indicated that the spanwise spacing alone is insufficient to characterise the surface heterogeneity. An additional parameter based on the ratio of perimeters of recessed and elevated regions, ξ, was adopted. It adequately captured the changes in shapes and widths of the ridges highlighting the effects of the heterogeneity on drag and the streamwise circulation in the outer layer.

Triple decomposition of the velocity components allowed the examination of the surface heterogeneity through the dispersive stresses. We determine qualitatively and quantitatively the contributions of the dispersive stresses to the total shear stress, which varied from 15% to 55%, proportional to the strength of the secondary motions. The total shear stress estimates were subsequently used to examine outer-layer similarity in the mean and turbulence statistics. The results still indicated lack of similarity in the mean flow, however a collapse with the smooth-wall is observed in the diagnostic form. This observation indicates that the secondary flows affect proportionally the mean flow and the turbulent structure in the outer region.

The two-point correlation maps of the streamwise velocity fluctuations R_{uu} allowed the examination of the turbulence structures in the outer region. The structures exhibit spanwise symmetry above the LMPs and HMPs, while, they are asymmetric in the wall-normal direction due to the intense inward/outward radial motions. In the mid-distance between the LMPs and HMPs, the turbulent structures exhibited a relatively higher coherence accompanied with a substantial inclination towards the HMPs, which is consistent with previous studies. The analysis of the TNTI revealed the impact of the secondary flows on the wake intermittency. Instantaneous snapshot showed the existence of strong bulges and valleys in the interface outline, which is translated in TNTI undergoing a spanwise modulation. The extent of the intermittency is shown to vary across the spanwise direction with a shorter and larger intermittency extents at the upwash and downwash regions, respectively. The global probability density function of the TNTI indicated that the main impact of the secondary flows is the change in the intermittency extent, with stronger secondary flows inducing a larger extent.

6. Development of turbulent boundary layer secondary flows past a heterogeneous to homogeneous step-change

6.1 Introduction

In this chapter, a turbulent boundary layer flow developing over a streamwise step-change from heterogeneous to homogeneous smooth-wall is investigated. The upstream surface condition was modelled such that large-scale secondary motions are produced prior to the streamwise discontinuity. Similar with the previous studies, the heterogeneity consists of smooth streamwise-aligned ridges with $S/\delta \approx \mathcal{O}(1)$, with exact details as the X2HS4 case in chapter 5). This study examines the flow changes with stereoscopic-PIV and oil-film interferometry data perspectives to asses the impact on the development of these secondary flows and drag respectively. The experimental arrangement for this study is described in the section 3.2.3.

6.2 Skin friction past the step-change

Figure 6.1 illustrates the response of the oil-film interferograms to the surface shear stress caused by both spanwise and streamwise topographical heterogeneities. While the magnitude of the changes are less evident to be observed visually, clear directional modifications are depicted as well as the presence of a recirculating motion past the step. This region herein labelled $R1$, is believed to be home to a highly unsteady flow caused by the separation of the flow above and on the side ridges leading to the modifications observed in these oil-film streaks especially near the ridges. Upstream the step-change and to the vicinity of the ridges, both streamwise and spanwise shear stresses can be observed, as these interference patterns seem to align with a certain angle to the

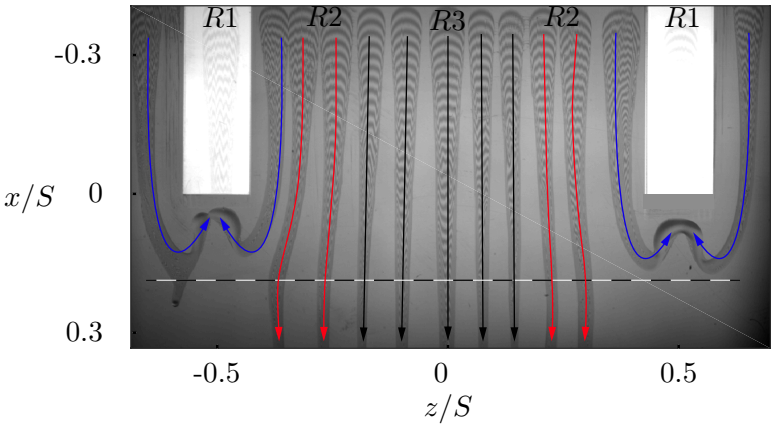

Figure 6.1: Example of oil droplets deposited upstream the step-change at $U_\infty = 20m/s$ with streamlines drawn to highlight the pattern displayed by the OFI streaks.

streamwise direction (marked in blue). As soon as the flow reaches the step-change, these streaks deviate from the streamwise alignment and end up recirculating past the ridge step. The streamwise extent of this separated flow can roughly be estimated to be between 1–1.5W, which is equivalent to 2–3h. At a certain spanwise distance from the ridges, a buffer region named $R2$ highlights the streaks to also be affected by the presence of the step-change but with a lesser extent. The streaks in this region (marked in red) start following a closer path as those in $R1$ right upstream and downstream the step-change, towards the recirculation region. However an inflexion point is observed illustrating their deviation from the previous path, which seems to coincide with the reattachment point (shown with a dashed line). Further away from the ridges, these streaks labelled $R3$ remain parallel to each other, although a slight expansion can still be observed when getting close to $R2$. However at the valley symmetry plane, the streaks remain insensitive to the presence of a step-change at a half-wavelength distance from them. Beyond a certain distance from the step (marked by the dashed line), the directions of these streaks at $R1$ and $R2$ seem to expand (diverge) towards the valley, however at a very small rate.

The above observations are more evident when presenting the spatial distribution of the friction velocity and its spanwise-averaged quantity. Figure 6.2(a) shows the spanwise distribution of the friction velocity across the different streamwise locations, which were determined from the OFI technique. The colours vary from the darkest to lightest grey indicating the increase in the fetch past the step-change, from $x/\delta = 0.2$ till $x/\delta = 8$, with δ being the boundary layer thickness upstream the step. Following the previous remarks from figure 6.1, a negative friction velocity is indeed captured at the nearest station obtained from the OFI measurements, highlighting the presence of a recirculation region right downstream the ridge step. The streamwise position of this measurement was right before the reattachment point at $x = 2h$. The further station downstream was obtained at $x/\delta = 0.35$ however indicated a positive friction velocity

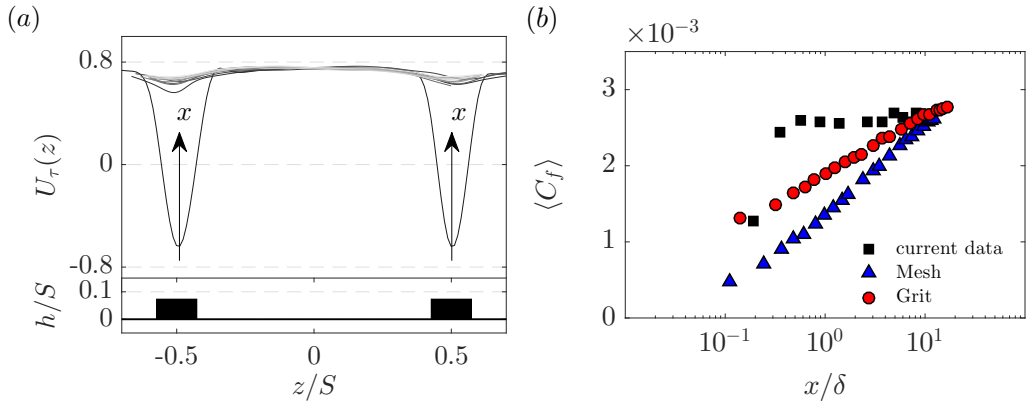

Figure 6.2: (*a*) Spanwise variation of the friction velocity across different streamwise stations highlighted by dark (near the step) to light grey and (*b*) the spanwise-averaged skin-friction coefficient with respect to the normalised streamwise distance, with δ being the boundary layer thickness upstream the step. Two datasets are included from Hanson and Ganapathisubramani (2016) for a comparison between a heterogeneous surface and two homogeneous rough-to-smooth surfaces.

synonym of the flow reattachment. Past the third station and at $z/S = \pm 0.5$, a slower recovery of the friction velocity is observed highlighting the persistence of the outer flow condition affecting the velocity gradient at the wall. At the valley symmetry plane, the overall magnitude of the friction velocity remains relatively unchanged past the step, confirming the previous observations from figure 6.1. This indicates that this part of the flow, stays resilient despite the presence of a streamwise step-change.

In order to get a better picture of the overall effect of the step-change on the wall drag, the spanwise-averaged skin-friction coefficient at each streamwise station is presented in figure 6.2(b). The figure also includes two datasets from a previous experiment in the same facility by Hanson and Ganapathisubramani (2016) who investigated the effect of a homogeneous rough-to-smooth transition of a mesh- and grit-type rough surfaces. Our results which are presented in black squares indicate that the overall streamwise extent which is affected by the step-change is $x < 0.5\delta$, in contrast with the homogeneous cases which at least require 20δ past the step in order to recover a new equilibrium. In spite of the upstream flow being heterogeneous in the spanwise direction, the near-wall flow shows a faster recovery towards a new "streamwise-equilibrium" state than a homogeneous flow. However, this pseudo-equilibrium state (shown by the invariance of the drag) is different to the classical homogeneous rough-to-smooth cases. Given that large-scale secondary motions have been previously observed in the outer region, the way the outer flow interacts with the near-wall region is likely to be affected.

6.3 Mean flow topology and secondary flows past the step-change

Combining the OFI and stereoscopic-PIV measurements, wall-drag as well as flow field information are presented together in figure 6.3. The skin friction map was obtained by interpolating nearly three hundred independent points from the OFI measurements that covered a surface of $8\delta \times 1.2\delta$ in the (x, z)-plane. On the other hand, the flow field cross-planes were obtained at $x/\delta = -0.65$, $x/\delta = 0.2$, $x/\delta = 4$ and $x/\delta = 8$ respectively. Similarly to our previous study, strong spanwise heterogeneities in the mean flow can be distinguished as shown in figure 6.3. These are represented in the form of alternating HMPs and LMPs between valleys and peaks respectively upstream the step-change. Moreover, these HMPs and LMPs seem to be associated with high and low shear stress respectively. The apparent difference between these results and the ones presented in section 4.2 stem from the effect of the ridge width explored and explained in chapter 5. Figure 6.3 also shows, despite the presence of a step-change, the outer region remains relatively unaffected whilst developing downstream. The aforementioned behaviour in the mean flow topology is further substantiated by the identification of secondary motions through the computation of the vorticity-signed swirling strength λ_{ci}. In agreement with our previous study, secondary motions consisting of a pair of counter-rotating vortices are formed on the top of either sides of the ridge, and just like in the mean flow, these are shown to persist further downstream.

A closer look at these maps is provided with the left and right panels in figure 6.3 showing the mean velocity and swirling strength maps respectively. Two contour of the normalised velocity levels at $U = 0.6U_\infty$ and $0.9U_\infty$ are highlighted in the figure to allow comparison in both the near-wall and outer regions respectively. Upstream the step-change, the contour level in the outer region presents the expected waviness caused by the secondary flows, while in the near-wall region, the contour level was unavailable due to lack of measurements in the canopy. Right after the step, the contour level seems to have increased, which is indicative of a relaxation of the overall boundary layer thickness caused by the adverse pressure gradient at the step. At the same time, a large impact is observed near the wall with a more heterogeneous mean flow. Further downstream, only small changes can be observed from the stations $x/\delta = 4$ and 8 for the outer region, as opposed to the near-wall which seems to recover faster than the outer flow. Although this near-wall region adapts faster than the outer layer, it remains that the corresponding wall shear stress is impacted by the outer flow heterogeneity.

Besides the large-scale secondary flows observed on the right panel of figure 6.3, a similar smaller pair of counter-rotating vortices emerged above the ridge, as reported in the previous study. This tertiary flow seems not to feature downstream the step, as opposed to the outer region secondary motion which persists further downstream. This

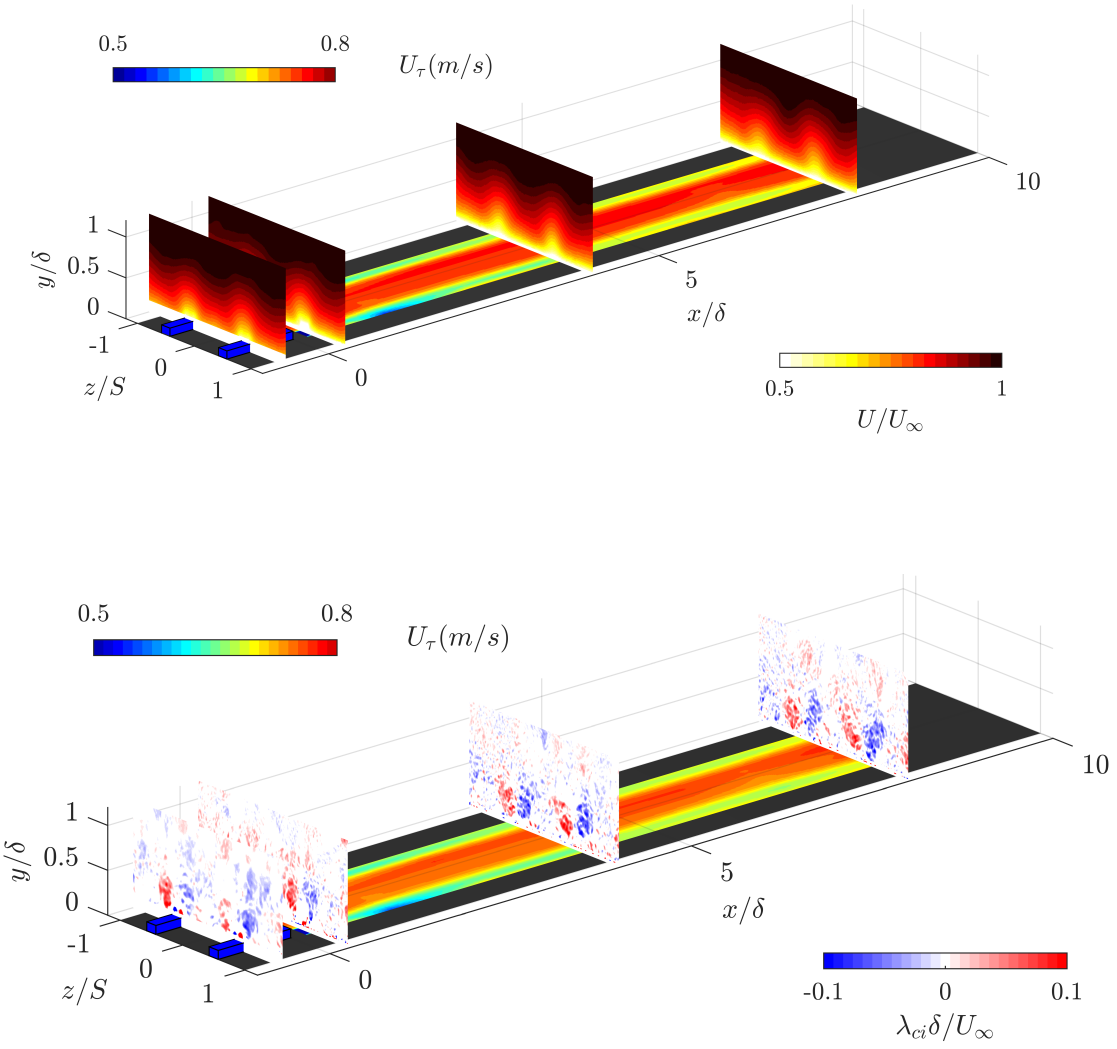

Figure 6.3: Cross-plane normalised mean (top) streamwise velocity and (bottom) vorticity-signed swirling strength maps at x/δ = -0.65, 0.25, 4 and 8 from left to right respectively. The mean friction velocity map is also included highlighting regions of high shear stress coinciding with regions of high-momentum pathways.

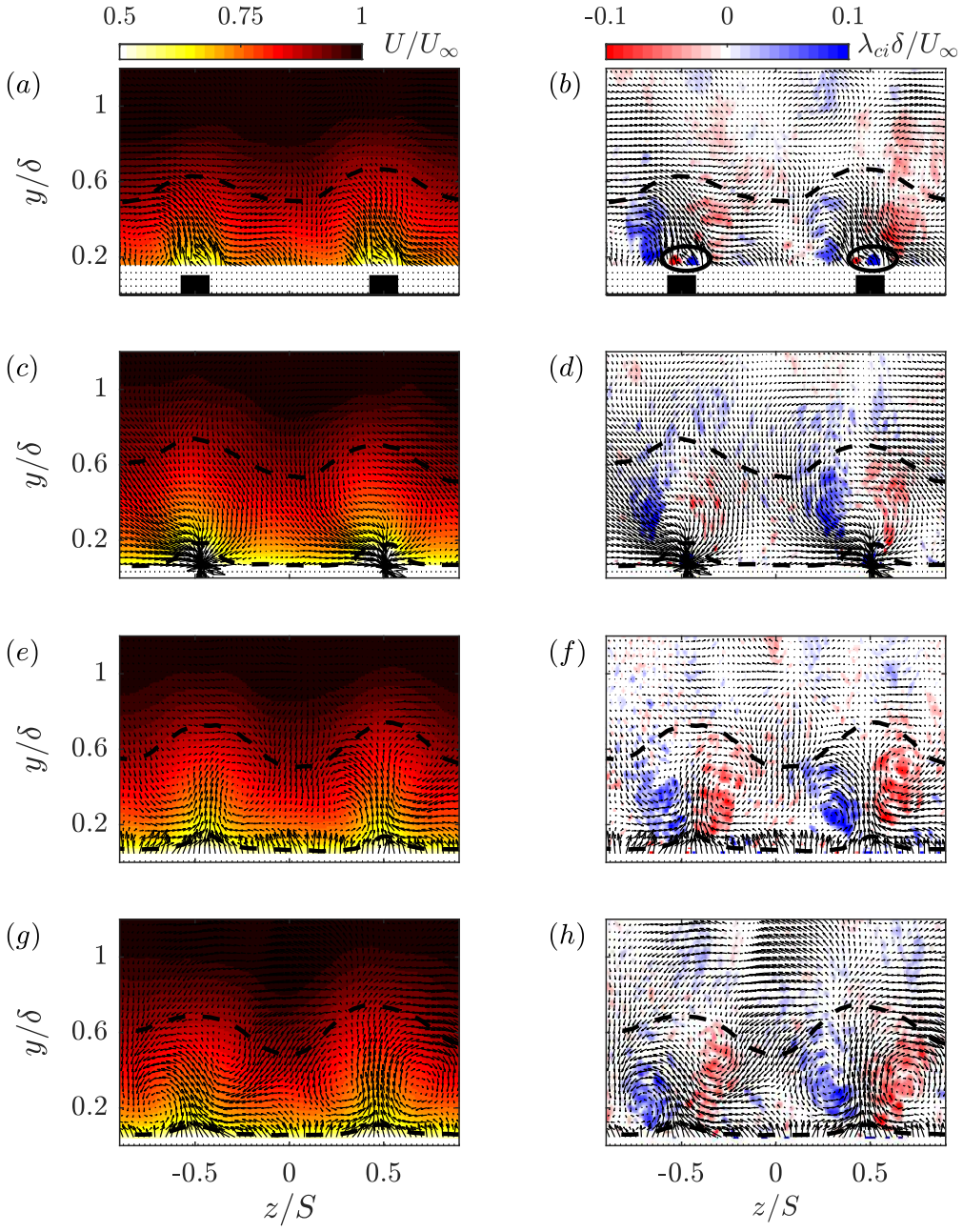

Figure 6.4: Contour maps of the normalised mean (left) streamwise velocity and (right) vorticity-signed swirling strength at (a, b) : $x/\delta = -0.65$, (c, d) : $x/\delta = 0.25$, (e, f) : $x/\delta = 4$ and (g, h) : $x/\delta = 8$. The upper and lower black dashed lines represent velocity levels of $U = 0.9U_\infty$ and $U = 0.6U_\infty$ respectively, while the ellipsoids in (b) highlight the presence of tertiary motions above the ridges. The mean in-plane velocity vector plot V and W are superimposed to show the vortical structures.

observation shows that these large-scale secondary motions are inherently capable of sustaining themselves for longer distances downstream of the step-change, and maintaining a good degree of self-similarity whilst flowing over the homogeneous surface. this is in contrast with the tertiary flows which seem incapable to self-sustain without a viscous boundary condition such as the presence of a ridge, leading to the observed changes in the near-wall region.

6.4 Near-wall and outer-layer scaling

In order to investigate the recovery of the mean flow, spanwise-averaged velocity profiles at the four streamwise stations are plotted in figure 6.5. Figure 6.5(a) presents the profiles scaled in terms of the classical outer variables U_∞ and δ. The profiles indicate the presence of a weak deficit essentially located in the inner region, while the outer region seems to nearly be unaffected. The overall recovery in the mean flow seems to almost be full at least for $y/\delta > 0.2$ for the last station.

Using the corresponding skin-friction measurements at each of the SPIV planes, the velocity profiles are also considered from the inner scaling perspective as shown in figure 6.5(b). The most salient remark in this figure is the presence of an upper shift in this scaling, with a higher slope than the classical smooth wall for the profile at $x/\delta = 0.25$. This behaviour essentially stems from the substantial reduction in the corresponding skin-friction magnitude. For the profiles further downstream, a small downward shift is still observed confirming that the previous surface condition still persists causing an overall momentum loss due to the presence of the secondary flows. Although their differences with the smooth wall seems small, their recovery seems gradually slow, hence might necessitate a much longer distance for the roughness function to nullify. A common feature which is observed for flows that undergo surface streamwise step-changes are the so-called internal boundary layers. This layer essentially represents the average extent at which the current surface condition has affected the upstream flow (Antonia, 1972; Garratt, 1990; Hanson and Ganapathisubramani, 2016). Many identification methods exists and usually consider a streamwise differentiation scheme, the detection of an inflexion point in successive mean velocity profiles or the turbulent stresses among others (see e.g. the work of Garratt (1990) on a review of the different methods). Given the results presented in figure 6.5, there is no clear sign of an internal boundary layer growth as there is no apparent inflexion point at this stage, at least with this global perspective. Perhaps this is caused by the fact that a large portion of the flow (in the spanwise direction) remained attached to the wall, hence the existence of such feature is not clearly visible in this configuration. This will further need to be examined in detail through the planar-PIV information as local identification can still be possible due to the locally separated flow past the step-change.

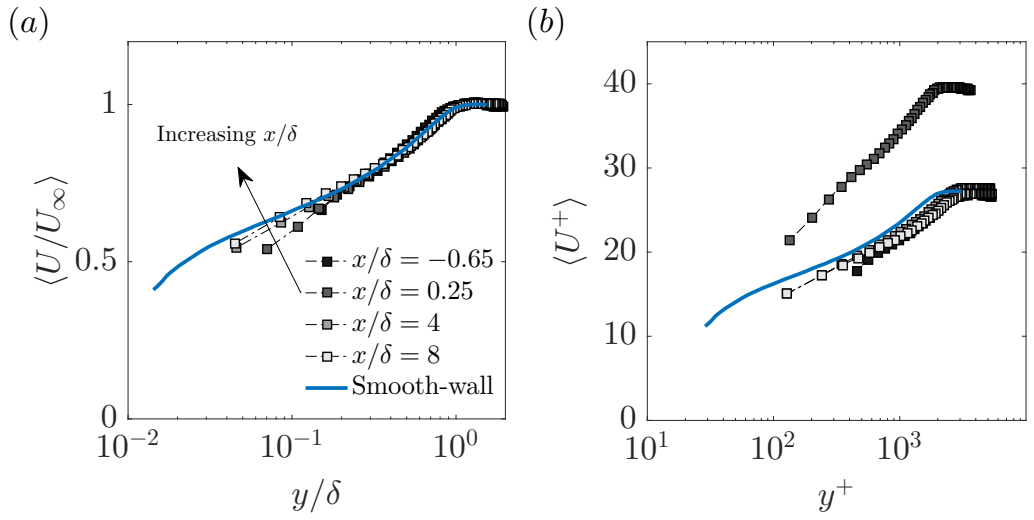

Figure 6.5: Spanwise-averaged of the mean streamwise velocity profiles in (a) outer and (b) inner-viscous scaling at the different streamwise locations with a comparison to a smooth-wall velocity profile presented in blue.

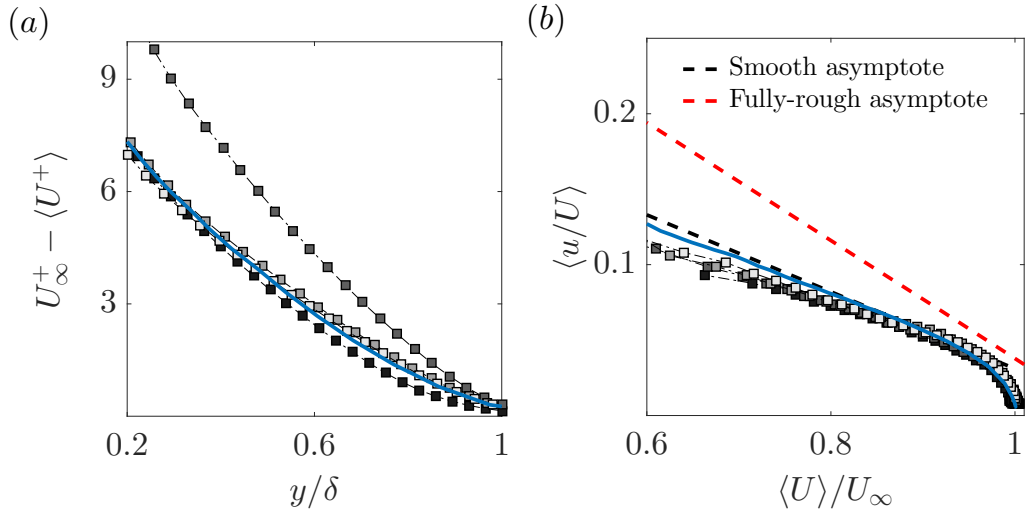

Figure 6.6: Effect of the step-change on the (a) spanwise-averaged mean velocity profiles in the defect form normalised with the friction velocity determined from the OFI. (b) Outer scaling of spanwise-averaged streamwise turbulence intensity in the diagnostic form. The blue solid-line represents the smooth-wall data from Medjnoun et al. (2018). See figure 6.5 for the symbol legend.

The response of the turbulent boundary layer flow to the step-change in terms of outer-layer similarity is examined in figure 6.6. Figure 6.6(a) presents the spanwise-averaged mean velocity profiles in defect form scaled with the friction velocity determined from the OFI measurements, while figure 6.6(b) illustrates the scaling in the diagnostic form (Alfredsson et al., 2011). A slight difference is shown for the profile right upstream the step-change, with a deviation appearing mostly from $y/\delta > 0.5$ onwards. However, for the profile right after the step, a substantial deficit is observed caused by the deceleration of the flow past the step-change. However, after a certain distance downstream, a good degree of self-similarity is shown consistently for the stations $x/\delta = 4$ and 8 respectively. This result is in agreement with the streamwise development of the skin friction presented in figure 6.2, showing beyond a certain distance from the streamwise discontinuity, a self-preserved form in the wall drag is achieved.

Furthermore, a good collapse is noticed for the variance profiles as shown in figure 6.6(b), not only between the different streamwise stations, but also with the smooth-wall profile. This result indicates that on one hand, despite the presence of a step-change, proportional changes in the streamwise turbulence intensity and the mean flow occur simultaneously in the outer region. On the other hand, the collapse of the profiles with the smooth wall irrespective of a non-zero roughness function ΔU^+ (representative of the downward and upward shifts shown in figure 6.5) is not reflected in the diagnostic plot. These results are also similar to our previous observations presented in figure 5.8(b), but inconsistent with the conclusions of Castro et al. (2013) who demonstrated that changes in ΔU^+ must be reflected in different slopes in u/U. However, as discussed in the previous study (section 5.5), one possible reason for the current behaviour is that the values of the roughness function are way to small to have a substantial impact. The second reason can be attributed to lack of rough protrusions which can inhibit high levels of streamwise turbulence intensity with respect to the mean flow.

The effect of the streamwise step-change on the turbulence organisation is also investigated through a triple decomposition performed on the three component velocity vector in the cross-plane using equation 5.4. This method enables the quantification of the stresses caused by the spanwise inhomogeneity of the mean flow, hence their contributions to the overall stress. In a similar approach to that presented in the previous study, comparative contour maps of the turbulent, dispersive and total shear stresses denoted $\overline{uv}$, $\overline{\tilde{u}\tilde{v}}$ and $\overline{\tau_{xy}}$ respectively are presented in figure 6.7 (in columns), at different streamwise stations (in rows). Equivalently, the dispersive shear stress upstream the step-change is not negligible with respect to the turbulent one, extending for nearly two thirds of the boundary layer thickness with varying intensity along the spanwise direction (shown in the second column from the left of figure 6.7(a)). The magnitude and distribution of the turbulent and dispersive shear stresses differ, with an overall distribution of $\overline{uv}$ following the modulation character of the mean flow. On the other hand, $\overline{\tilde{u}\tilde{v}}$ is shown to be more localised.

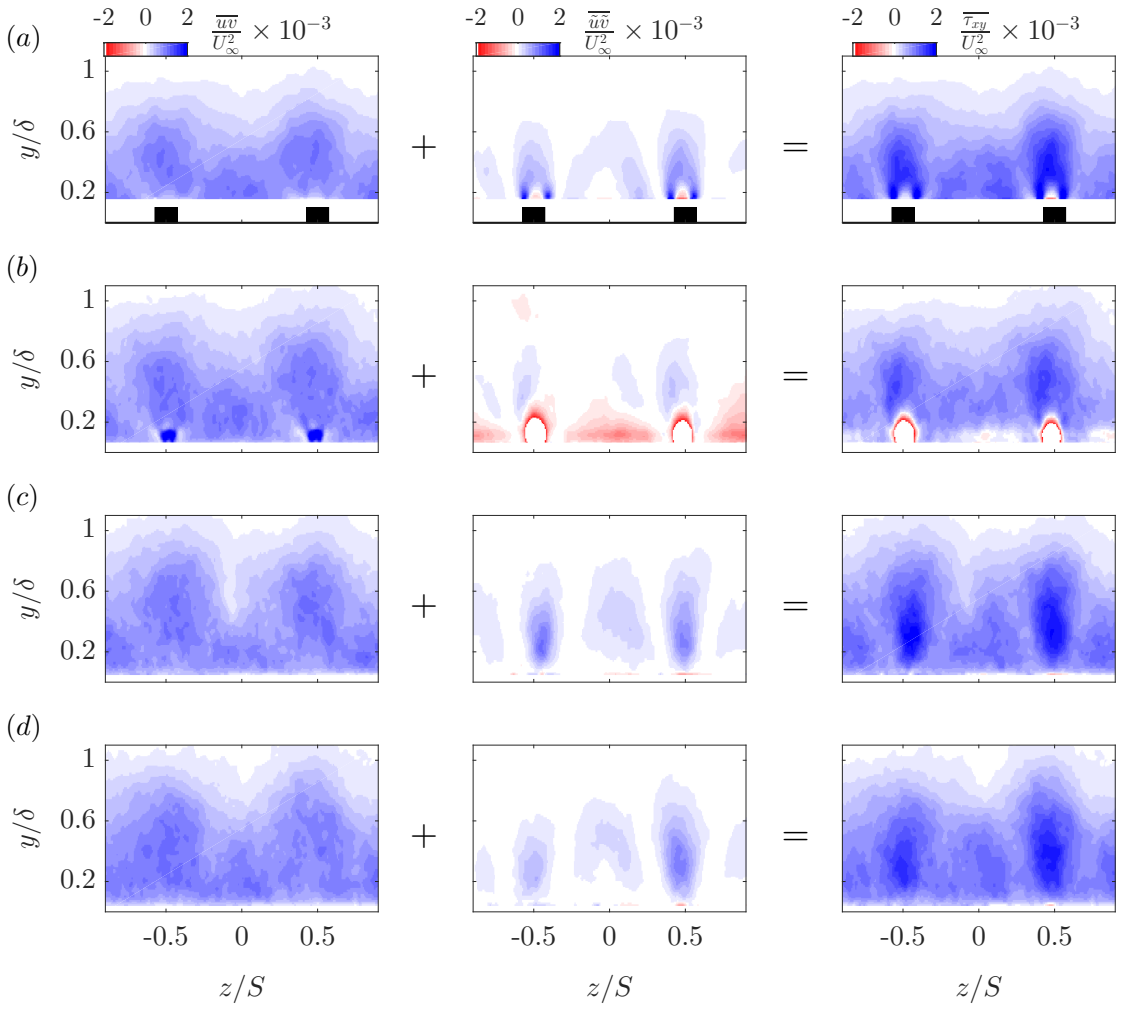

Figure 6.7: Effect of the step-change on the normalised (left) turbulent, (middle) dispersive and (right) total shear-stress for $(a) : x/\delta = -0.65$, $(b) : x/\delta = 0.25$, $(c) : x/\delta = 4$ and $(d) : x/\delta = 8$.

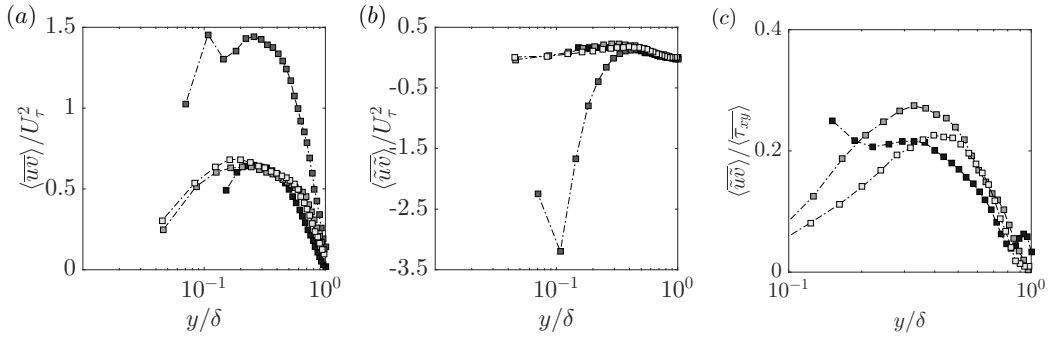

Figure 6.8: (a) Spanwise variation of the friction velocity across different streamwise stations highlighted by dark (near the step) to light grey and (b) the spanwise-averaged skin-friction coefficient with respect to the normalised streamwise distance from the step. Two datasets are included for comparison between heterogeneous surface and two homogeneous rough-to-smooth cases from Hanson and Ganapathisubramani (2016).

Right after the step-change, substantial modifications appear for both the turbulent and dispersive maps as shown in figure 6.7(b). Strong turbulent shear stress events are shown to occur past the ridge, while the turbulence activity in the outer region seems to diffuse vertically and radially, which can be caused by the flow deceleration. This observation hints to a reduction in the overall outer-layer heterogeneity. This is in fact substantiated by the changes that occurred in the dispersive shear stress component, which highlights a reduction in the degree of heterogeneity in the outer region, however with a negative turbulence activity near the wall. This result seems to have also impacted the overall shear stress which shows intense negative turbulence activity past the ridges. This behaviour is due to strong negative dispersive component of V past the discontinuity caused by the adjustment of the upstream flow to the new surface condition. Therefore, the diminution of the spanwise heterogeneity comes from a dual effect of the turbulence diffusion due to deceleration as well as the negation between the upstream upwash flow occurring above the ridges and the downwash of the recirculation region imposed by the streamwise step-change. At farther distances downstream the step-change, both turbulent and dispersive shear stresses shown in figure 6.7(c) and (d) seem to adopt similar patterns to those observed in figure 6.7(a). Moreover, the previous observation –negative dispersive shear stress activity near the wall– does not seem to hold for such distances, confirming that it is a consequence of the step-change. The downstream persistence of the dispersive component is in line with the mean flow and swirling strength maps presented before, confirming the resilience of such large-scale features to pertain at this long fetch.

In order to quantify the overall effect of the flow heterogeneity on the turbulent boundary layer, the global behaviour of the turbulent and dispersive stresses is examined using spanwise-averaging over a wavelength as shown in figure 6.8. Figure 6.8(a) and (b) show the wall-normal distribution of the spanwise-averaged turbulent and dispersive shear stresses respectively, normalised by their corresponding friction velocity determined from the OFI. Figure 6.8(c) on the other hand presents the contribution of the dispersive shear stress to the total shear stress. Qualitative similarity between the profiles upstream the step as well as the ones at $x/\delta = 4$ and 8 is observed for both the turbulent and dispersive components, with a plateau between $0.15 > y/\delta > 0.25$ for $\overline{uv}$. For the dispersive component, a shorter plateau is observed slight further away from the wall between $0.25 > y/\delta > 0.35$. At $x/\delta = 0.25$, the profiles are substantially altered due to the friction velocity which is considerably small at that location, making the magnitude of the $\overline{uv}$ much larger. On the other hand, $\overline{\tilde{u}\tilde{v}}$ is shown to be massively intense and negative for $y/\delta < 0.3$, and marginal compared with the other profiles for $y/\delta > 0.3$. The overall contribution of the dispersive component towards the total shear stress is shown in figure 6.8(c) for three profiles, with the exclusion of the profiles at $x/\delta = 0.25$ as it is out of scale. Upstream the step-change, $\langle\overline{\tilde{u}\tilde{v}}\rangle/\langle\overline{\tau_{xy}}\rangle$ is shown to contribute for up to 20% of the total stress, which then increases to nearly 27% at $x/\delta = 4$, then reduces back to 20% at $x/\delta = 8$. These results alongside the mean swirling strength

maps indicate that these large-scale secondary motions may require very long distances in order to diffuse and reduce their impact of the mean and turbulent flow.

6.5 Summary

Unprecedented measurements of turbulent boundary layer secondary flows past a heterogeneous to homogeneous step-change are presented. We particularly examined the impact of the streamwise step-change on the mean flow, drag and the turbulence quantities using oil-film interferometry along with stereo-PIV measurements.

Near the step-change, oil-film streaks were visualized and showed that in the vicinity of the ridges, the interference patterns change direction due to the strong radial motions towards the ridges. This is in contrast with the ones observed at the valley centre, which were shown to be perpendicular to the incoming flow. Right past the step, three different regions have been identified through their patterns. The closest streaks to the step deviated from their original path an showed a backflow, highlighting the presence of a recirculation region. Slightly further away in the spanwise direction, the oil-film streaks also showed a deviation but weaker, which first diverted towards the recirculation region, then changed the direction towards the valley past the reattachment fetch. In the centre of the valley, the oil-film streaks hardly felt any changes in the wall condition at half wavelength from them, and only a subtle divergence of the streaks was observed.

The above observations were further confirmed through the estimates of the friction velocity distributions both across the span and the streamwise directions. Negative friction velocities were reported right past the step of the ridge, while in the valley the drag was shown to be unaffected. The spanwise inhomogeneity remained till the last measurement station in the current study at $x/\delta = 8$ indicating the persistence of the velocity gradient at the wall being spanwise heterogeneous. The spanwise-averaged skin-friction coefficient revealed that a new pseudo-state of equilibrium in terms of drag is reached quite close to the step ($x/\delta \approx 0.5$), which is substantially different in comparison with other homogeneous rough-to-smooth boundary layer flows.

Upstream the step-change, high- and low-momentum pathways have been shown from the streamwise velocity maps above valleys and ridges respectively. These persisted further downstream the step with only minor changes occurring in the near-wall region, while the outer layer was shown to be merely affected by the change in surface condition. These observations were corroborated by the examination of the swirling strength maps which also highlighted large-scale secondary flows to persist across all this investigated fetch. The main difference being the small pair of counter-rotating vortices above the ridges (tertiary flows) which were observed upstream the step, vanished due to the local adverse pressure gradient imposed by the step-change.

Outer-scaled spanwise-averaged velocity profiles showed that the overall shape of the flow $y/\delta > 0.2$ has not been affected, irrespective of the streamwise location, and only a marginal deficit is observed in the near-wall region when compared with the smooth-wall profile. However, when it is scaled in inner units, both a downward and upward shits in the logarithmic regions were observed, due to the actual changes in their corresponding wall drag. Nonetheless, both scaling could not provide the presence of an internal boundary layer growing past the step-change. This is partly due to the unresolved near-wall region (data only available beyond $y^+ \approx 100$). More importantly, the other reason comes from the nature of the flow, which itself does not see the presence of a step, except in the vicinity of the ridges, while the flow in the valley remains completely attached. Therefore, only a local internal boundary layer past the low-momentum pathways is meaningful in the present scenario.

Outer-layer similarity is examined in both defect and diagnostic forms. The former highlighted the presence of a large deficit right past the step due to the flow decelerating, causing the local skin friction to considerably reduce. Further downstream, the profiles were shown to have a good degree of self-similarity despite the presence of the secondary motions. In fact, these large-scale secondary motions are perhaps the reason why the current flow showed a pseudo-state of equilibrium since both the outer flow as well as the corresponding spanwise-averaged skin friction were shown to not change past $x = 0.5\delta$. These results were also shown to hold for the local turbulence profiles in the diagnostic form as all the profiles collapse between themselves and the smooth wall.

The degree of flow heterogeneity was also examined through the triple decomposition of the velocity fields and assessment of the dispersive stresses. Upstream the step-change, the dispersive shear stress map highlighted a considerable degree of heterogeneity, with stresses extending for at least two thirds of the boundary layer thickness, which contribute to about 20% of the total shear stress. Past the step-change, substantial changes occurred due to the deceleration of the flow above the ridges, inducing a strong negative dispersive stress. Meanwhile, the turbulent shear stress diffusion increased throughout the outer layer, causing a reduction in the overall heterogeneity. As soon as the flow reached a certain distance past the step-change, the flow recovered its initial heterogeneous state, with contributions reaching 27% of the overall shear stress. This result supports the idea that these large-scale secondary flows posses enough inertia to sustain themselves for long distances, while maintaining a good degree of self-similarity over a homogeneous surface condition. This indicates that in order for these types of turbulent boundary layers to recover spanwise homogeneity, very long distances are required to allow for the secondary motions to diffuse.

7. Conclusion

7.1 General discussion

Many questions have attracted the attention of researchers with respect to wall-bounded flows that exhibit large-scale secondary motions. Further to the previous literature, this study focused on three main questions , and tried to provide additional insight to the current understanding of secondary flows in turbulent boundary layers.

Can inner- and outer-layer similarity be possible in the presence of secondary flows?

Despite its applicability to a small portion of the flow, the utility of the law-of-the-wall is of great importance in modelling of wall turbulence. In this study, we examined the viability of this paramount concept for a turbulent boundary layer flow harbouring large-scale secondary motions. Our results revealed the existence of a logarithmic region despite the three-dimensionality of the flow, just as in homogeneous smooth- and rough-wall flows. Its extent across the spanwise directions depends on the local condition (local friction velocity together with the wake intermittency). By assuming the logarithmic slope constant (i.e. Von Karman constant), zero-plane displacement together with roughness functions have been examined, and are found to be most enhanced in regions of low-momentum pathways. The utility of outer-layer similarity in flows with secondary motions has also been questioned and examined. Based on the experimental work of Wu and Christensen (2007, 2010) and Pathikonda and Christensen (2017), both mean flow and structural similarity were shown to exist despite the emergence of secondary flows. Their assessment was achieved locally, while the local drag was inferred from the Reynolds shear stress profiles. This is in contrast to our current results that showed outer-layer similarity to be affected.

From the overall results of chapter 4, it has been shown that the surface heterogeneity leads to a breakdown of outer-layer similarity in mean flow, turbulence statistics as well as spectra. Here we used an idealised heterogeneous surface with streamwise-oriented smooth ridges. This was done in order to directly measure the local skin friction, which

was then used to assess the similarity. However, we believe that our findings should also be applicable to any heterogeneous rough/smooth surface where the characteristic spanwise length scale of the surface is comparable to the boundary layer thickness resulting in secondary flows, regardless of the roughness height (e.g. Kevin et al. 2017) or the roughness geometry (e.g. Vanderwel and Ganapathisubramani 2015; Yang and Anderson 2017). The reason for lack of similarity is attributed to the amplified radial motions due to local imbalances between the turbulence production and dissipation as postulated by Hinze (1967, 1973) and Anderson et al. (2015), when $S/\delta_{av} \approx \mathcal{O}(1)$. This significantly changes the mean and the turbulent flow characteristics when compared to turbulent boundary layers over homogeneous smooth- or rough-wall surfaces, hence making the local skin friction inadequate to sufficiently satisfy outer-layer similarity.

Other recent studies also agree with our statement (Yang and Anderson 2017; Chung et al. 2018; Chan et al. 2018). Chan et al. (2018) provided useful insight onto the conditions of validity of the similarity hypothesis, based on the quantification of the dispersive stresses. They showed that as long as these stresses remained only prominent near the canopy layer, the turbulent structures in the outer region remain unaffected by the secondary flows. However this only occurs for very small spanwise wavelengths. As soon as the wavelength is comparable to the dominant length scale of the flow, the secondary flows occupy a large portion of the primary flow, which induce dispersive stresses that extend farther into the outer region. Our current findings from chapter 5 also corroborate these observations such that the cases presenting strong secondary motions, showed lack of outer-layer similarity.

It is also important to recall that the primary condition for outer-layer similarity is large scale separation (Jiménez 2004; Castro 2007; Flack and Schultz 2014; Squire et al. 2016). In the case of the study by Barros and Christensen (2014), their surface roughness exhibited a wide range of multiscale features as opposed to the other studies. These roughness features are likely to enhance near-wall mixing, increase the overall drag and the scale separation. This combined with perhaps relatively mild dispersive stresses can result in the validity of outer-layer similarity.

Are there other relevant length scales that carry the heterogeneity information, and how to predict the location of the upwash and downwash motions for the topographical heterogeneous surfaces?

Based on existing literature, there exists two main classes or categories of surfaces that seemingly exhibited similar flow attributes, yet have different triggering mechanisms of secondary flows.

For the skin-friction based heterogeneity whose surface alternates between high and low wall shear stress (due to surface roughness or superhydrophobic surfaces etc), both

the width of the high/low skin friction and the characteristic spanwise wavelength were shown to be relevant. Willingham et al. (2014) showed that by keeping the spanwise wavelength constant, increasing the high drag width produced stronger mean flow heterogeneity. They showed that the HMPs and LMPs systematically occurred above the high and low wall shear stress, respectively. On the other hand, Stroh et al. (2016) varied both the spanwise wavelength and the low shear stress width and reported their important influence on the flow topology. They showed that for a relatively thin strip of the high shear stress, HMPs and LMPs occurred above the low and high wall shear stress, respectively. For increased strip widths, the opposite behaviour occurred. Chung et al. (2018) have also showed by keeping the high-to-low roughness widths constant and just increasing the spanwise wavelength, the HMPs and LMPs are always observed above the high and low wall shear stress, respectively. The exception being that for very large wavelengths (both large high/low skin-friction widths), the HMPs and LMPs appeared above the low and high skin friction, respectively. This is a confirmation that local homogeneity of the flow can be recovered (away from the discontinuity), with high and low roughness producing thicker and thinner boundary layer thickness. Hence, the different studies indicate that perhaps more than one length scale should be considered for surface heterogeneity.

Most of the previous studies for the ridge-type heterogeneous surfaces showed that the spanwise wavelength is relevant for the presence of the secondary flows (Nezu and Nakagawa 1984; Vanderwel and Ganapathisubramani 2015; Yang and Anderson 2017; Hwang and Lee 2018). Based on the existing observations, a hypothetical evolution of "significance" of the secondary motions can be sketched in order to illustrate the effect of the heterogeneity on boundary layer flows based on this length scale. In figure 7.1, the flow is separated into three different regimes. In regime A, the secondary flows are small enough such that they are confined in the roughness sublayer. In this case, the outer flow would still remain "homogeneous" along the span. In this case, we expect outer-layer similarity to hold for the mean flow and turbulence quantities. In regime B, secondary flows are expected to occupy a big portion of the primary flow and their effect is expected to extend through the entire boundary layer. Here, the flow is highly three-dimensional and it was shown to violate the outer-layer similarity hypothesis. Finally, regime C is topographically sparse and can be considered a combination of the two first regimes with a homogeneous region far from the hills (or the wall-drag discontinuities) and a heterogeneous region when close enough to the hills (or the wall-drag discontinuities). The extent of these regimes is rather difficult to assess as this would require extensive and detailed investigations of several parameters that can affect the secondary flows. This figure has recently been confirmed numerically with the LES performed by Yang and Anderson (2017), who showed for a wide range of spanwise wavelength, the flow undergoes different regimes.

Analogously to the study of Willingham et al. (2014), the current results highlighted

the importance of an additional surface feature depicted by the ratio of recessed and elevated regions in addition to the spanwise wavelength. This analogy between the two wall conditions is sketched in figure 7.2 (a) and (b) for the ridge- and roughness-type heterogeneity, respectively, for a fixed wavelength (S). By drawing on the results from the current and previous studies, we can identify notable differences in the two types. Considering a generic shape such as a rectangle of a given height at varying widths to represent the ridge-type heterogeneity, we can observe secondary as well as tertiary flows as shown in this chapter 5. For very thin ridges, strong secondary flows are expected (similar to X2HS2) with upwash and downwash occurring above and in between the ridges. Increasing the width results in the bifurcation to tertiary flows competing with the secondary flows above the ridge, thereby weakening the mean flow heterogeneity. Increasing the width beyond a certain limit results in the swap of HMPs and LMPs, with an overall decrease in the flow heterogeneity, till the flow becomes homogeneous again. In the case of roughness-type heterogeneity, the secondary flows are expected to remain confined in the vicinity of stress discontinuity for the limits of very wide/narrow strips. This results in a weak Reynolds shear stress heterogeneity causing the base flow to remain homogeneous. Between these two limits, the secondary flows reach their full potential over a range of widths, then will decrease eventually when increasing/decreasing above/below a certain limit.

Following the above observations, it is clear that the spanwise wavelength is not sufficient on its own to describe the flow heterogeneity. A surface heterogeneity parameter $\mathcal{H}$ can be considered as a combination of S and an additional surface parameter (ξ):

$$\mathcal{H} = F\left(\frac{S}{\delta}, \xi\right) \tag{7.1}$$

In case of a ridge-type heterogeneity, we have shown in chapter 5 that ξ can be expressed as a ratio of the area/perimeter of the elevated and recessed regions. This was shown to capture both the shape and width variations of the ridges. In the case of a roughness-type, ξ can relate to a ratio of the high-to-low roughness (or high-to-low shear stress) weighted by their respective widths. Overall, S/δ parameter captures the "creation" or "existence" of secondary flows while ξ is a parameter that captures the "enhancement" or "enrichment" of the secondary motions. For the ridge-type surfaces considered here, the relationship between the secondary flow circulation and ξ appears to be linear for a fixed S/δ over the range of ξ examined here.

The second part of the question has also garnered attention, due to some controversies in the spanwise locations of the HMPs and LMPs for the ridge-type heterogeneity. Several studies reported similar findings to ours when $S/\delta \approx \mathcal{O}(1)$ (Nezu and Nakagawa 1984; Colombini 1993; Wang and Cheng 2006; Vanderwel and Ganapathisubramani 2015; Hwang and Lee 2018; Vanderwel et al. 2019). Contrastingly, other recent investigations showed that the opposite situation can occur (Mejia-Alvarez and Christensen

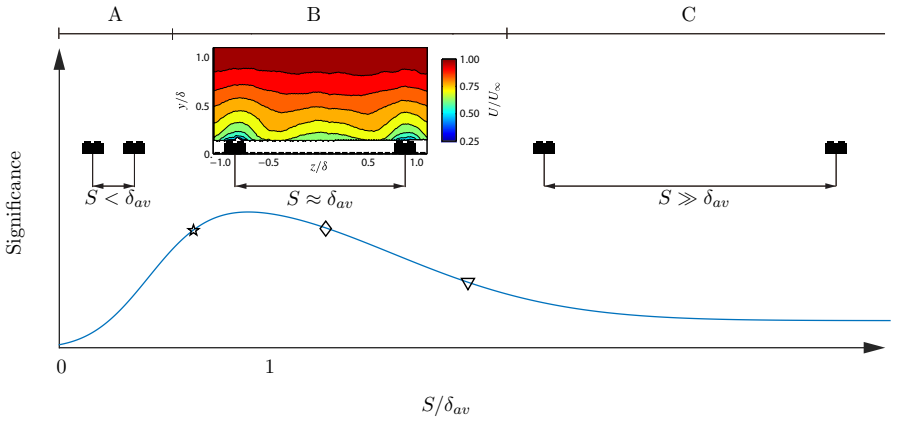

Figure 7.1: Hypothetical evolution curve of the secondary flow size/strength as a function of the spanwise spacing, inspired from Vanderwel and Ganapathisubramani (2015). Regimes A, B and C are representative of homogeneous, heterogeneous and transitional surfaces respectively. Symbols represent values of S/δ_{av} explored in the chapter 4.

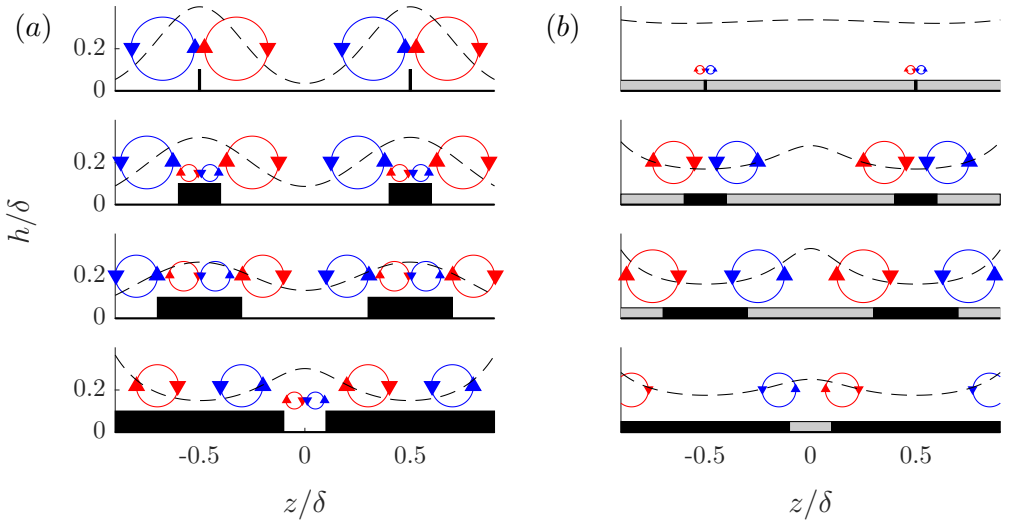

Figure 7.2: Sketch illustrating the effect of the ridge/roughness width for the (a) ridge-type and (b) strip-type heterogeneity. The secondary motions and mean flow curvature are highlighted in clockwise/anticlockwise red/blue circles and black dashed lines respectively.

2013; Barros and Christensen 2014; Yang and Anderson 2017; Awasthi and Anderson 2018). However, one of the key differences between these two sets of studies is the presence/absence of streamwise homogeneity of the surface. In fact, all the studies that reported the upwash above the surface elevations used streamwise continuous ridges, in contrast with the studies that reported downwash to occur above the elevated regions. The highly irregular roughness of Mejia-Alvarez and Christensen (2013); Barros and Christensen (2014) and the highly ordered roughness of Yang and Anderson (2017); Awasthi and Anderson (2018) clearly exhibit wake producing protrusions, which induce form-drag contributions. Therefore, despite these surfaces being topographically heterogeneous, they appear to act more like high/low wall shear stress producing surfaces, in

contrast with the previous ones which are predominantly viscous drag producing surfaces. The exception was the surface studied by Vanderwel and Ganapathisubramani (2015) which also contained form-drag producing pins. However these protrusions were homogeneously distributed over the surface, meaning that their overall contributions remained uniform as opposed to Yang and Anderson (2017) and Awasthi and Anderson (2018) which were localised only at the surface elevations. Although this explanation may seem plausible following the rule of "high" and "low" roughness generating downwash and upwash respectively, this is clearly not the case for the staggered sinusoidal roughness investigated by Chan et al. (2018). In fact, they reported the HMPs and LMPs to be located between the peaks and valleys of the topography, corresponding to regions of low and high wall shear stress. Consequently, it still remains unclear what are the driving mechanisms behind the direction of the secondary flows.

What are the effects of a heterogeneous to homogeneous step-change on turbulent boundary layer secondary flows?

Wall-bounded turbulent flows experiencing surface roughness discontinuities are ubiquitous in many environmental flows. They occur in nature such as in atmospheric boundary layers that undergo topographical variations such as streamwise heterogeneous terrains, changes from grasslands to forests or simply flows from land to sea (or vice versa). In well-controlled environments such as in experimental laboratories or numerical domains, these are generally idealised by changes in surface roughness (i.e. rough-to-smooth or smooth-to-rough), where the properties of the flow over the initial surface are a priori known. The step-change induces a state of non-equilibrium due to the change in shear stress which sees the emergence of an internal boundary layer caused by the new surface condition. This new layer retains the characteristics imposed by the surface underneath it, while above this layer, the flow preserves information from the flow upstream the step. Most of the existing literature examined the character of the internal boundary layer, from its identification methods and its growth to the characteristics of the mean flow and the turbulence properties (Antonia, 1972; Garratt, 1990; Hanson and Ganapathisubramani, 2016). However, the previous studies concern themselves with an upstream flow developing over a homogeneous surface, be it rough or smooth.

Considering an idealised heterogeneous to homogenous smooth surface step-change, previously unreported results were presented with key findings on the drag, and the properties of the flows in the outer region. Changes in the local wall shear stress were first highlighted by visualising oil-film streaks, that showed the presence of a highly three-dimensional flow near the spanwise heterogenity. Right downstream the step-change, three distinct regions have been identified; $R1$: a three-dimensional separated flow region, $R3$: a two-dimensional attached flow region. $R2$: a buffer region between

the two- and three-dimensional regions. This first assessment was further confirmed by determining the friction velocity distribution in both the streamwise and spanwise directions. The friction velocity varied symmetrically past the step-change, however with the friction velocity being negative right past the ridge induced by the separated flow. The spanwise variation is weaker when getting close to the valley region ($R2$). This spanwise variation lasted till our last measurement station, indicating persistent inhomogeneity at the wall. The streamwise variation of the spanwise-averaged skin friction revealed a new state of equilibrium is reached at $x/\delta \approx 0.5$, which is considerably shorter in comparison with other homogeneous rough-to-smooth cases.

The upstream large-scale secondary motions along with their resulting high- and low-momentum pathways were shown to persist downstream with minor changes in the near-wall region, whereas the outer layer showed a consistent form of self-preservation. These were corroborated by the examination of the spanwise-averaged velocity profiles in both inner and outer scaling. Even thought not observed, it is speculated that an internal boundary layer still does exist due to the surface step-change but not in the classical sense. In fact, a large portion of the flow remained completely attached, and only the flow in the vicinity of the ridges has separated, hence only a local internal boundary layer past the low-momentum pathways is meaningful in the present scenario. The velocity profiles in defect form and diagnostic plot showed that self-similarity is maintained even for such distances hinting that the flow has built a pseudo-state of equilibrium in the presence of these secondary motions. The evolution of the degree of heterogeneity was also assessed and revealed that the dispersive shear stress contributes to at least 20% of the overall shear stress in the farthest stations, just as much as was upstream the step-change. These observations indicate that these large-scale secondary flows posses a high degree of self-similarity, since they are capable to self-sustain for a such long fetch. Consequently, this means that both the growth rates of the internal boundary layer as well as the turbulent boundary layer will depend on the evolution process of these large-scale secondary motions.

7.2 Outlook

This study has provided both complementary and previously undocumented results for zero pressure gradient turbulent boundary layer flows exhibiting secondary motions, due to surface spanwise heterogeneities. In light of the outcomes of this experimental investigation, additional research is encouraged both with the actual and new datasets to investigated some of the outstanding questions.

Chapter 4 revealed that under spanwise heterogeneity, the turbulent boundary layer properties do not exhibit out-layer similarity. Hence, further studies are required to identify how to appropriately scale the boundary layer properties for flows over general

heterogeneous surfaces, and also identify the range of S/δ_{av} over which traditional scaling laws are satisfied.

The premultiplied streamwise energy spectra revealed the impact of the surface heterogeneity both in the near wall as well as in the outer region. It is seen that when the flow is probed at the peak spanwise location, the secondary flow signature is revealed in the streamwise velocity fluctuations, such that a new energetic length scale emerges between 3-5δ. This is currently believed to be a signature of the secondary motions as it appears to diminish when getting farther away from the peak, while its presence is observed regardless of the spanwise spacing imposed to the flow. However, no signature of the very-large-scale-motions (VLSMs) is detected in the spectrograms, and their absence can be explained by two reasons. First, as reported by Hutchins and Marusic (2007), their signature can only be detected when a large-scale separation is achieved (i.e. high Reynolds numbers $Re_\tau > 5000$). The second reason could be that the presence of secondary motions does not allow the growth of the VLSMs, or reduces their meandering to a large extent, whereby the secondary motions 'redistribute' the energy across smaller and intermediate scales. This is an excellent question which requires further attention, but will clearly require additional data at high Reynolds numbers. Hence, it would be useful to examine the exact nature of these VLSMs (through both HWA and PIV measurements) and their relation with the induced large-scale secondary motions. For instance, it would be interesting to investigate the character of these organised motions in terms of energy and Reynolds shear stress contributions, but also the outer layer large-scales with the near-wall small scales interactions (i.e. amplitude and frequency modulation).

Chapter 5 showed that the surface heterogeneity encompasses an additional scaling factor that carries the heterogeneity information alongside the spanwise wavelength. However, additional datasets are required in order to generalise this scaling for three-dimensional surfaces (e.g. including rough protrusions). In the same perspective, the prediction of HMPs and LMPs locations through the high and low roughness argument holds its own merits, since this is almost verified for all the available studies reported in this work with the exception of the staggered arrangement roughness (egg-carton like roughness) investigated by Chan et al. (2018). Therefore, more studies are required to investigated these types of staggered heterogeneous rough walls, along with more realistic ones that contain a large range of roughness scales. Additionally, if strip-type heterogeneity induced HMPs and LMPs over the high and low roughness patches, and ridge-type heterogeneity induced the HMPs and LMPs over the valleys and peaks respectively, is it perhaps possible to enhance or reduce the heterogeneity effect to control the strength of the secondary flows by combining these two type? In a different perspective, the current dataset itself could be used to further investigate the characteristics of the instantaneous structures in the outer region, and assess the uniform momentum zones under the influence of secondary flows.

Finally, chapter 6 explored an undocumented question which is the development of the turbulent boundary layer secondary flows past a heterogeneous to homogeneous step-change. Since the area remains unexplored, various aspects could be investigated through the above mentioned analysis. However, two main questions stand with higher importance. First, how does the secondary flow affect the growth of the internal boundary layer, and what is the mechanism through which the secondary flows self-sustain. By answering first these questions, intuitively the third question related to the distance required to reach a new state of equilibrium can be reached. But first, the current dataset could be used to identify closely the presence of an internal boundary layer through the planar-PIV measurements (which were not presented in this study) which covered an extent of approximately 10δ past the step-change.

References

Abdel-Rahman, A., Tropea, C., Slawson, P., and Strong, A. (1987). On temperature compensation in hot-wire anemometry. *J Phys E: Sci Instrum*, 20(3):315.

Acharya, M., Bornstein, J., and Escudier, M. (1986). Turbulent boundary layers on rough surfaces. *Exp Fluids*, 4(1):33–47.

Adrian, R. J. (2005). Twenty years of particle image velocimetry. *Exp Fluids*, 39(2):159–169.

Adrian, R. J. (2007). Hairpin vortex organization in wall turbulence. *Phys Fluids*, 19(4):041301.

Adrian, R. J. and Westerweel, J. (2011). *Particle Image Velocimetry*, volume Cambridge Aerospace Series. Cambridge University Press.

Akomah, A., Hangan, H., and Naughton, J. (2011). Very high reynolds number boundary layers over 3d sparse roughness and obstacles: the mean flow. *Exp Fluids*, 51(3):743.

Alfredsson, P. H., Segalini, A., and rl, R. (2011). A new scaling for the streamwise turbulence intensity in wall-bounded turbulent flows and what it tells us about the outer peak. *Phys Fluids*, 23(4):041702.

Amir, M. and Castro, I. P. (2011). Turbulence in rough-wall boundary layers: universality issues. *Exp Fluids*, 51(2):313–326.

Anderson, W., Barros, J. M., Christensen, K. T., and Awasthi, A. (2015). Numerical and experimental study of mechanisms responsible for turbulent secondary flows in boundary layer flows over spanwise heterogeneous roughness. *J. Fluid Mech*, 768:316–347.

Anderson, W., Yang, J., Shrestha, K., and Awasthi, A. (2018). Turbulent secondary flows in wall turbulence: vortex forcing, scaling arguments, and similarity solution. *Environ. Fluid Mech*, 18(6):1351–1378.

Andreopoulos, J. and Bradshaw, P. (1981). Measurements of turbulence structure in the boundary layer on a rough surface. *Boundary Layer Meteorol*, 20(2):201–213.

Antonia, R. A. (1972). Conditionally sampled measurements near the outer edge of a turbulent boundary layer. *J. Fluid Mech*, 56(1):118.

Awasthi, A. and Anderson, W. (2018). Numerical study of turbulent channel flow perturbed by spanwise topographic heterogeneity: Amplitude and frequency modulation within low- and high-momentum pathways. *Phys. Rev. Fluids*, 3:044602.

Bai, H. L., Kevin, K., Hutchins, N., and Monty, J. P. (2018). Turbulence modifications in a turbulent boundary layer over a rough wall with spanwise-alternating roughness strips. *Phys Fluids*, 30(5):055105.

Bai, T., Liu, J., Zhang, W., and Zou, Z. (2014). Effect of surface roughness on the aerodynamic performance of turbine blade cascade. *Propulsion and Power Research*, 3(2):82–89.

Barros, J. M. and Christensen, K. T. (2014). Observations of turbulent secondary flows in a rough-wall boundary layer. *J. Fluid Mech*, 748.

Barros, J. M. and Christensen, K. T. (2019). Characteristics of large-scale and superstructure motions in a turbulent boundary layer overlying complex roughness. *J Turbul*, 20(2):147–173.

Benedict, L. and Gould, R. (1996). Towards better uncertainty estimates for turbulence statistics. *Exp Fluids*, 22(2):129–136.

Benschop, H. and Breugem, W. (2017). Drag reduction by herringbone riblet texture in direct numerical simulations of turbulent channel flow. *J. Turbul*, 18(8):717–759.

Bisset, D. K., Hunt, J. C. R., and Rogers, M. M. (2002). The turbulent/non-turbulent interface bounding a far wake. *J. Fluid Mech*, 451:383–410.

Blay Esteban, L., Dogan, E., Rodríguez-Lopéz, E., and Ganapathisubramani, B. (2017). Skin-friction measurements in a turbulent boundary layer under the influence of free-stream turbulence. *Exp Fluids*, 58(9):115.

Bons, J. P. (2010). A review of surface roughness effects in gas turbines. *J Turbomach*, 132(2):021004.

Bons, J. P., Reimann, D., and Bloxham, M. (2008). Separated flow transition on an lp turbine blade with pulsed flow control. *J Turbomach*, 130(2):021014.

Bons, J. P., Taylor, R. P., McClain, S. T., and Rivir, R. B. (2001). The many faces of turbine surface roughness. In *ASME Turbo Expo 2001: Power for Land, Sea, and Air*, pages V003T01A042–V003T01A042. American Society of Mechanical Engineers.

Castro, I. P. (2007). Rough-wall boundary layers: mean flow universality. *J. Fluid Mech*, 585:469–485.

Castro, I. P., Segalini, A., and Alfredsson, P. H. (2013). Outer-layer turbulence intensities in smooth-and rough-wall boundary layers. *J. Fluid Mech*, 727:119–131.

Chan, L., MacDonald, M., Chung, D., Hutchins, N., and Ooi, A. (2018). Secondary motion in turbulent pipe flow with three-dimensional roughness. *J. Fluid Mech*, 854:5–33.

Chauhan, K., Philip, J., de Silva, C. M., Hutchins, N., and Marusic, I. (2014). The turbulent/non-turbulent interface and entrainment in a boundary layer. *J. Fluid Mech*, 742:119–151.

Cheng, H. and Castro, I. P. (2002). Near wall flow over urban-like roughness. *Boundary Layer Meteorol*, 104(2):229–259.

Chow, L. and Maheikey, E. (1992). Surface roughness and its effects on the heat transfer mechanism in spray cooling. *J Heat Transfer*, 114:211.

Chung, D., Monty, J. P., and Hutchins, N. (2018). Similarity and structure of wall turbulence with lateral wall shear stress variations. *J. Fluid Mech*, 847:591–613.

Clauser, F. H. (1956). The turbulent boundary layer. *Advances in applied mechanics*, 4:1–51.

Coceal, O., Dobre, A., Thomas, T. G., and Belcher, S. E. (2007). Structure of turbulent flow over regular arrays of cubical roughness. *J Fluid Mech*, 589:375409.

Colebrook, C. F., Blench, T., Chatley, H., Essex, E., Finniecome, J., Lacey, G., Williamson, J., and Macdonald, G. (1939). Correspondence. turbulent flows in pipes, with particular reference to the transition region between the smooth and rough pipe laws.(includes plates). *Journal of the Institution of Civil engineers*, 12(8):393–422.

Coles, D. (1956). The law of the wake in the turbulent boundary layer. *J. Fluid Mech*, 1:191–226.

Colombini, M. (1993). Turbulence-driven secondary flows and formation of sand ridges. *J. Fluid Mech*, 254:701–719.

Connelly, J., Schultz, M., and Flack, K. (2006). Velocity-defect scaling for turbulent boundary layers with a range of relative roughness. *Exp Fluids*, 40(2):188–195.

Corino, E. R. and Brodkey, R. S. (1969). A visual investigation of the wall region in turbulent flow. *J Fluid Mech*, 37(1):130.

Corrsin, T. and Kistler, A. L. (1955). Free-stream boundaries of turbulent flows. Naca technical report 1244, Washington, DC.

Darcy (1857). Recherches exprimentales relatives au mouvement de l'eau dans les tuyaux. In *Paris.Mallet-Bachelier*, page 268. pages and atlas.

Dean, B. and Bhushan, B. (2010). Shark-skin surfaces for fluid-drag reduction in turbulent flow: a review. *Philosophical Transactions of the Royal Society of London A: Mathematical, Physical and Engineering Sciences*, 368(1929):4775–4806.

DeGraaff, D. B. and Eaton, J. K. (2000). Reynolds-number scaling of the flat-plate turbulent boundary layer. *J Fluid Mech*, 422(1):319–346.

Djenidi, L., Talluru, K. M., and Antonia, R. A. (2018). Can a turbulent boundary layer become independent of the reynolds number? *J. Fluid Mech*, 851:1–22.

Fernholz, H. and Finleyt, P. (1996). The incompressible zero-pressure-gradient turbulent boundary layer: an assessment of the data. *Prog Aerosp Sci*, 32(4):245–311.

Ferreira, M. A., Rodriguez-Lopez, E., and Ganapathisubramani, B. (2018). An alternative floating element design for skin-friction measurement of turbulent wall flows. *Exp Fluids*, 59(10):155.

Finnigan, J. J., Shaw, R. H., and Patton, E. G. (2009). Turbulence structure above a vegetation canopy. *J Fluid Mech*, 637:387424.

Flack, K. A. and Schultz, M. P. (2010). Review of hydraulic roughness scales in the fully rough regime. *J. Fluids Engng*, 132(4):041203.

Flack, K. A. and Schultz, M. P. (2014). Roughness effects on wall-bounded turbulent flowsa). *Phys Fluids*, 26(10):101305.

Flack, K. A., Schultz, M. P., and Connelly, J. S. (2007). Examination of a critical roughness height for outer layer similarity. *Phys Fluids*, 19(9):095104.

Flack, K. A., Schultz, M. P., and Shapiro, T. A. (2005). Experimental support for townsends reynolds number similarity hypothesis on rough walls. *Phys Fluids*, 17(3):035102.

Ganapathisubramani, B., Hutchins, N., Monty, J. P., Chung, D., and Marusic, I. (2012). Amplitude and frequency modulation in wall turbulence. *J Fluid Mech*, 712:6191.

Ganapathisubramani, B., Longmire, E. K., and Marusic, I. (2003). Characteristics of vortex packets in turbulent boundary layers. *J Fluid Mech*, 478:35–46.

Garratt, J. R. (1990). The internal boundary layer — a review. *Boundary-Layer Met*, 50(1):171–203.

Garratt, J. R. (1994). Review: the atmospheric boundary layer. *Earth Sci Rev*, 37(1-2):89–134.

Goldstein, D. B. and Tuan, T.-C. (1998). Secondary flow induced by riblets. *J. Fluid Mech*, 363:115–151.

Guala, M., Tomkins, C. D., Christensen, K. T., and Adrian, R. J. (2012). Vortex organization in a turbulent boundary layer overlying sparse roughness elements. *Journal of Hydraulic Research*, 50(5):465–481.

Gyr, A. and Kinzelbach, W. (2004). Bed forms in turbulent channel flow. *Appl. Mech. Rev*, 57(1):77–93.

Hagen (1854). Uber den einfluss der temperatur auf die bewegung des wassers in rohren. *Abh. Kon. Akad. Wiss*, page 1798.

Haidari, A. H. and Smith, C. R. (1994). The generation and regeneration of single hairpin vortices. *J Fluid Mech*, 277:135162.

Hama, F. R. (1954). Boundary-layer characteristics for smooth and rough surfaces. *Trans. Soc. Naval Arch. Mar. Engirs*, 62(1):333–358.

Hanson, R. and Ganapathisubramani, B. (2016). Development of turbulent boundary layers past a step change in wall roughness. *J. Fluid Mech*, 795:494523.

Head, M. R. and Bandyopadhyay, P. (1981). New aspects of turbulent boundary-layer structure. *J Fluid Mech*, 107:297338.

Hinze, J. O. (1967). Secondary currents in wall turbulence. *Phys Fluids*, 10(9):122–S12.

Hinze, J. O. (1973). Experimental investigation on secondary currents in the turbulent flow through a straight conduit. *Appl. Sci. Res*, 28(1):453–465.

Hinze, J. O. (1975). *Turbulence*. 2 edition.

Hoerner, S. F. (1965). *Fluid-dynamic drag: practical information on aerodynamic drag and hydrodynamic resistance*. Hoerner Fluid Dynamics Midland Park, NJ.

Hong, J., Katz, J., Meneveau, C., and Schultz, M. P. (2012). Coherent structures and associated subgrid-scale energy transfer in a rough-wall turbulent channel flow. *J Fluid Mech*, 712:92128.

Hultmark, M. and Smits, A. J. (2010). Temperature corrections for constant temperature and constant current hot-wire anemometers. *Meas Sci Technol*, 21(10):105404–.

Hutchins, N. and Marusic, I. (2007). Evidence of very long meandering features in the logarithmic region of turbulent boundary layers. *J Fluid Mech*, 579:1–28.

Hutchins, N., Nickels, T. B., Marusic, I., and Chong, M. S. (2009). Hot-wire spatial resolution issues in wall-bounded turbulence. *J. Fluid Mech*, 635:103–136.

Hwang, H. G. and Lee, J. H. (2018). Secondary flows in turbulent boundary layers over longitudinal surface roughness. *Phys. Rev. Fluids*, 3:014608.

Inagaki, A. and Kanda, M. (2010). Organized structure of active turbulence over an array of cubes within the logarithmic layer of atmospheric flow. *Boundary Layer Meteorol*, 135(2):209–228.

Jackson, P. S. (1981). On the displacement height in the logarithmic velocity profile. *J. Fluid Mech*, 111:15–25.

Jacob, C. and Anderson, W. (2017). Conditionally averaged large-scale motions in the neutral atmospheric boundary layer: Insights for aeolian processes. *Boundary Layer Meteorol*, 162(1):21–41.

Jiménez, J. (2004). Turbulent flows over rough walls. *Annu Rev Fluid Mech*, 36:173–196.

Kahler, C. J., Scharnowski, S., and Cierpka, C. (2013). High resolution velocity profile measurements in turbulent boundary layers. In *TSFP DIGITAL LIBRARY ONLINE*. Begel House Inc.

Kevin, K., Monty, J., and Hutchins, N. (2019). Turbulent structures in a statistically three-dimensional boundary layer. *J. Fluid Mech*, 859:543–565.

Kevin, K., Monty, J. P., Bai, H. L., Pathikonda, G., Nugroho, B., Barros, J. M., Christensen, K. T., and Hutchins, N. (2017). Cross-stream stereoscopic particle image velocimetry of a modified turbulent boundary layer over directional surface pattern. *J. Fluid Mech*, 813:412–435.

Kim, K. C. and Adrian, R. J. (1999). Very large-scale motion in the outer layer. *Phys Fluids*, 11(2):417–422.

King, L. V. (1914). On the convection of heat from small cylinders in a stream of fluid: Determination of the convection constants of small platinum wires with applications to hot-wire anemometry. *Philosophical transactions of the royal society of London. series A, containing papers of a mathematical or physical character*, 214(509-522):373–432.

Kline, S. J., Reynolds, W. C., Schraub, F. A., and Runstadler, P. W. (1967). The structure of turbulent boundary layers. *J Fluid Mech*, 30(4):741773.

Krogstad, P.-. and Antonia, R. A. (1994). Structure of turbulent boundary layers on smooth and rough walls. *J Fluid Mech*, 277:121.

Krogstad, P.-Å., Antonia, R., and Browne, L. (1992). Comparison between rough-and smooth-wall turbulent boundary layers. *J Fluid Mech*, 245:599–617.

Krug, D., Philip, J., and Marusic, I. (2017). Revisiting the law of the wake in wall turbulence. *J. Fluid Mech*, 811:421–435.

Laskari, A., de Kat, R., Hearst, R. J., and Ganapathisubramani, B. (2018). Time evolution of uniform momentum zones in a turbulent boundary layer. *J. Fluid Mech*, 842:554–590.

Lentink, D. and de Kat, R. (2014). Gliding swifts attain laminar flow over rough wings. *PLoS One*, 9(6):e99901.

Marchis, M. D., Milici, B., and Napoli, E. (2015). Numerical observations of turbulence structure modification in channel flow over 2d and 3d rough walls. *Int J Heat Fluid Flow*, 56:108 – 123.

Marusic, I., McKeon, B., Monkewitz, P., Nagib, H., Smits, A., and Sreenivasan, K. (2010). Wall-bounded turbulent flows at high reynolds numbers: Recent advances and key issues. *Phys Fluids*, 22(6):065103.

Marusic, I., Monty, J. P., Hultmark, M., and Smits, A. J. (2013). On the logarithmic region in wall turbulence. *J. Fluid Mech*, 716:R3.

Mathis, R., Hutchins, N., and Marusic, I. (2009). Large-scale amplitude modulation of the small-scale structures in turbulent boundary layers. *J Fluid Mech*, 628:311337.

McLelland, S. J., Ashworth, P. J., Best, J. L., and Livesey, J. R. (1999). Turbulence and secondary flow over sediment stripes in weakly bimodal bed material. *J. Hydraul. Engng*, 125(5):463–473.

Medjnoun, T., Vanderwel, C., and Ganapathisubramani, B. (2018). Characteristics of turbulent boundary layers over smooth surfaces with spanwise heterogeneities. *J. Fluid Mech*, 838:516–543.

Medjnoun, T., Vanderwel, C., and Ganapathisubramani, B. (2020). Effects of heterogeneous surface geometry on secondary flows in turbulent boundary layers. *J Fluid Mech*, 886:A31.

Mejia-Alvarez, R. and Christensen, K. T. (2013). Wall-parallel stereo particle-image velocimetry measurements in the roughness sublayer of turbulent flow overlying highly irregular roughness. *Phys Fluids*, 25(11):115109.

Meyers, J., Ganapathisubramani, B., and Cal, R. B. (2019). On the decay of dispersive motions in the outer region of rough-wall boundary layers. *J. Fluid Mech*, 862:R5.

Millikan, C. B. (1938). A critical discussion of turbulent flows in channels and circular tubes. In *Proc. 5th Int. Cong. Appl. Mech*, pages 386–392. Wiley/Chapman and Hall, New York-London.

Moinuddin, K. A. M., Joubert, P. N., and Chong, M. S. (2004). Experimental investigation of turbulence-driven secondary motion over a streamwise external corner. *J. Fluid Mech*, 511:1–23.

Monty, J., Dogan, E., Hanson, R., Scardino, A., Ganapathisubramani, B., and Hutchins, N. (2016). An assessment of the ship drag penalty arising from light calcareous tubeworm fouling. *Biofouling*, 32(4):451–464.

Monty, J., Hutchins, N., Ng, H., Marusic, I., and Chong, M. (2009). A comparison of turbulent pipe, channel and boundary layer flows. *J Fluid Mech*, 632:431–442.

Moody, L. F. (1944). Friction factors for pipe flow. *Trans. Asme*, 66(8):671–684.

Nagib, H. M. and Chauhan, K. A. (2008). Variations of von krmn coefficient in canonical flows. *Phys Fluids*, 20(10):101518.

Nagib, H. M., Chauhan, K. A., and Monkewitz, P. A. (2007). Approach to an asymptotic state for zero pressure gradient turbulent boundary layers. *Phil. Trans. R. Soc. Lond. A*, 365(1852):755–770.

Napoli, E., Armenio, V., and De Marchis, M. (2008). The effect of the slope of irregularly distributed roughness elements on turbulent wall-bounded flows. *J. Fluid Mech*, 613:385–394.

Naughton, J. W. and Brown, J. L. (1996). Surface interferometric skin-friction measurement technique. In *AIAA, Advanced Measurement and Ground Testing Technology Conference, 19 th, New Orleans, LA*.

Naughton, J. W. and Sheplak, M. (2002). Modern developments in shear-stress measurement. *Prog. Aerosp. Sci*, 38(6-7):515–570.

Nezu, I. and Nakagawa, H. (1984). Cellular secondary currents in straight conduit. *J. Fluids Engng*, 110(2):173–193.

Nezu, I., Tominaga, A., and Nakagawa, H. (1993). Field measurements of secondary currents in straight rivers. *J. Fluids Engng*, 119(5):598–614.

Nikora, V. and Goring, D. (2000). Flow turbulence over fixed and weakly mobile gravel beds. *J Hydraul Eng*, 126(9):679–690.

Nikora, V., Koll, K., McEwan, I., McLean, S., and Dittrich, A. (2004). Velocity distribution in the roughness layer of rough-bed flows. *J Hydraul Eng*, 130(10):1036–1042.

Nikora, V., McEwan, I., McLean, S., Coleman, S., Pokrajac, D., and Walters, R. (2007). Double-averaging concept for rough-bed open-channel and overland flows: Theoretical background. *J. Hydraul. Engng*, 133(8):873–883.

Nikuradse, J. (1930). Untersuchungen über turbulente strömungen in nicht kreisförmigen rohren. *Ing-Arch*, 1(3):306–332.

Nikuradse, J. (1933). Str {ö} mungsgestze in rauhen rohren.

Nugroho, B., Hutchins, N., and Monty, J. P. (2013). Large-scale spanwise periodicity in a turbulent boundary layer induced by highly ordered and directional surface roughness. *Intl J. Heat Fluid Flow*, 41:90–102.

Orlu, R. and Vinuesa, R. (2017). *Experimental Aerodynamics (Ed. S. Discetti and A. Ianiro)*.

Österlund, J. M., Johansson, A. V., Nagib, H. M., and Hites, M. H. (2000). A note on the overlap region in turbulent boundary layers. *Phys Fluids*, 12(1):1–4.

Pailhas, G., Barricau, P., Touvet, Y., and Perret, L. (2009). Friction measurement in zero and adverse pressure gradient boundary layer using oil droplet interferometric method. *Exp Fluids*, 47(2):195–207.

Pathikonda, G. and Christensen, K. T. (2017). Inner˘outer interactions in a turbulent boundary layer overlying complex roughness. *Phys. Rev. Fluids*, 2:044603.

Perry, A. and Abell, C. (1977). Asymptotic similarity of turbulence structures in smooth- and rough-walled pipes. *J Fluid Mech*, 79(04):785–799.

Perry, A. and Li, J. D. (1990). Experimental support for the attached-eddy hypothesis in zero-pressure-gradient turbulent boundary layers. *J Fluid Mech*, 218:405–438.

Placidi, M. (2015). *On the effect of surface morphology on wall turbulence*. Phd thesis.

Pope, S. (2000). Turbulent flows, 771 pp.

Prandtl, L. (1904). Eine neue darstellung der torsionsspannungen bei prismatischen stäben von beliebigem querschnitt. *Jahresbericht der Deutschen Mathematiker-Vereinigung*, 13:31–36.

Prandtl, L. (1925). Bericht ber untersuchungen zur ausgebildeten turbulenz. *Z. Angew. Math. Mech*, 5(2):136–139.

Prandtl, L. (1952). *Essentials of fluid dynamics*. Blackie.

Raupach, M. (1992). Drag and drag partition on rough surfaces. *Boundary-Layer Met*, 60(4):375–395.

Raupach, M. R. and Shaw, R. H. (1982). Averaging procedures for flow within vegetation canopies. *Boundary-Layer Met*, 22(1):79–90.

Reynolds, O. (1895). On the dynamical theory of incompressible viscous fluids and the determination of the criterion. *Proc Roy Soc London*, 56(336-339):40–45.

Reynolds, R. T., Hayden, P., Castro, I. P., and Robins, A. G. (2007). Spanwise variations in nominally two-dimensional rough-wall boundary layers. *Exp Fluids*, 42(2):311–320.

Reynolds, W. C. and Hussain, A. K. M. F. (1972). The mechanics of an organized wave in turbulent shear flow. part 3. theoretical models and comparisons with experiments. *J. Fluid Mech*, 54(2):263–288.

Ruedi, J. D., Nagib, H., Österlund, J., and Monkewitz, P. A. (2003). Evaluation of three techniques for wall-shear measurements in three-dimensional flows. *Exp Fluids*, 35(5):389–396.

Schetz, J. A. (1993). Boundary layer analysis. *NASA STI/Recon Technical Report A*, 93.

Schlichting, H. (1979). *Boundary-layer theory*. McGraw-Hill, 7th edition.

Schultz, M. P. (2007). Effects of coating roughness and biofouling on ship resistance and powering. *Biofouling*, 23(5):331–341.

Schultz, M. P. and Flack, K. A. (2005). Outer layer similarity in fully rough turbulent boundary layers. *Exp Fluids*, 38(3):328–340.

Sciacchitano, A., Neal, D. R., Smith, B. L., Warner, S. O., Vlachos, P. P., Wieneke, B., and Scarano, F. (2015). Collaborative framework for piv uncertainty quantification: comparative assessment of methods. *Meas Sci Technol*, 26(7):074004.

Segalini, A., rl, R., and Alfredsson, P. H. (2013). Uncertainty analysis of the von krmn constant. *Exp Fluids*, 54(2):1–9.

Shockling, M. A., Allen, J. J., and Smits, A. J. (2006). Roughness effects in turbulent pipe flow. *J. Fluid Mech*, 564:267–285.

Sigal, A. and Danberg, J. E. (1990). New correlation of roughness density effect on the turbulent boundary layer. *AIAA Journal*, 28(3):554–556.

Smits, A. J., McKeon, B. J., and Marusic, I. (2011). Highreynolds number wall turbulence. *Annu Rev Fluid Mech*, 43:353–375.

Squire, D. T., Morrill-Winter, C., Hutchins, N., Marusic, I., Schultz, M. P., and Klewicki, J. C. (2016). Smooth- and rough-wall boundary layer structure from high spatial range particle image velocimetry. *Phys. Rev. Fluids*, 1:064402.

Squire, L. C. (1961). The motion of a thin oil sheet under the steady boundary layer on a body. *J. Fluid Mech*, 11:161–179.

Stroh, A., Hasegawa, Y., Kriegseis, J., and Frohnapfel, B. (2016). Secondary vortices over surfaces with spanwise varying drag. *J. Turbul*, 17(12):1142–1158.

Tanner, L. H. and Blows, L. G. (1976). A study of the motion of oil films on surfaces in air flow, with application to the measurement of skin friction. *J. Phys E*, 9(3):194.

Tennekes, H. and Lumley, J. L. (1972). *A first course in turbulence*. MIT press.

Theodorsen, T. (1952). Mechanism of turbulence. In *Mechanism of turbulence*. Columbus: Ohio State University.

Theurer, W., Baechlin, W., and Plate, E. (1992). Model study of the development of boundary layers above urban areas. *J Wind Eng Ind Aerodyn*, 41(1):437–448.

Thom, A. (1971). Momentum absorption by vegetation. *Quart J Roy Meteor Soc*, 97(414):414–428.

Townsend, A. A. (1976). *The structure of turbulent shear flow*. 2nd edition.

Tropea, C., Y. A. and Foss, J. (2007). *Springer Handbook of Experimental Fluid Mechanics*. Springer-Verlag Berlin Heidelberg, 1 edition.

Türk, S., Daschiel, G., Stroh, A., Hasegawa, Y., and Frohnapfel, B. (2014). Turbulent flow over superhydrophobic surfaces with streamwise grooves. *J. Fluid Mech*, 747:186–217.

Van Bokhorst, E., De Kat, R., Elsinga, G. E., and Lentink, D. (2015). Feather roughness reduces flow separation during low reynolds number glides of swifts. *J Exp Biol*, 218(20):3179–3191.

Van Rij, J. A., Belnap, B. J., and Ligrani, P. M. (2002). Analysis and experiments on three-dimensional, irregular surface roughness. *J Fluids Eng*, 124(3):671–677.

Vanderwel, C. and Ganapathisubramani, B. (2015). Effects of spanwise spacing on large-scale secondary flows in rough-wall turbulent boundary layers. *J. Fluid Mech*, 774:R2.

Vanderwel, C., Placidi, M., and Ganapathisubramani, B. (2017). Wind resource assessment in heterogeneous terrain. *Phil. Trans. R. Soc. Lond. A*, 375(2091):20160109.

Vanderwel, C., Stroh, A., Kriegseis, J., Frohnapfel, B., and Ganapathisubramani, B. (2019). The instantaneous structure of secondary flows in turbulent boundary layers. *J. Fluid Mech*, 862:845–870.

Volino, R. J., Schultz, M. P., and Flack, K. A. (2007). Turbulence structure in rough-and smooth-wall boundary layers. *J. Fluid Mech*, 592:263–293.

Volino, R. J., Schultz, M. P., and Flack, K. A. (2009). Turbulence structure in a boundary layer with two-dimensional roughness. *J Fluid Mech*, 635:75101.

Volino, R. J., Schultz, M. P., and Flack, K. A. (2011). Turbulence structure in boundary layers over periodic two-and three-dimensional roughness. *J. Fluid Mech*, 676:172–190.

Von Kármán, T. (1930). Mechanische änlichkeit und turbulenz. *Nachrichten von der Gesellschaft der Wissenschaften zu Göttingen, Mathematisch-Physikalische Klasse*, 1930:58–76.

Von Karman, T. (1934). Turbulence and skin friction. *J Aeronaut Sci*, 1(1):1–20.

Wallace, J. M., Eckelmann, H., and Brodkey, R. S. (1972). The wall region in turbulent shear flow. *J Fluid Mech*, 54(1):3948.

Wang, Z. Q. and Cheng, N. S. (2005). Secondary flows over artificial bed strips. *Adv. Water Resour*, 28(5):441–450.

Wang, Z. Q. and Cheng, N. S. (2006). Time-mean structure of secondary flows in open channel with longitudinal bedforms. *Adv. Water Resour*, 29(11):1634–1649.

Westerweel, J., Fukushima, C., Pedersen, J. M., and Hunt, J. C. R. (2005). Mechanics of the turbulent-nonturbulent interface of a jet. *Phys Rev Lett*, 95:174501.

Wieneke, B. (2005). Stereo-piv using self-calibration on particle images. *Exp Fluids*, 39(2):267–280.

Wieneke, B. (2017). *PIV uncertainty quantification and beyond*. PhD thesis, Delft University of Technology.

Willingham, D., Anderson, W., Christensen, K. T., and Barros, J. M. (2014). Turbulent boundary layer flow over transverse aerodynamic roughness transitions: induced mixing and flow characterization. *Phys Fluids*, 26(2):025111.

Wu, Y. and Christensen, K. T. (2007). Outer-layer similarity in the presence of a practical rough-wall topography. *Phys Fluids*, 19(8):085108.

Wu, Y. and Christensen, K. T. (2010). Spatial structure of a turbulent boundary layer with irregular surface roughness. *J. Fluid Mech*, 655:380–418.

Yang, J. and Anderson, W. (2017). Numerical study of turbulent channel flow over surfaces with variable spanwise heterogeneities: Topographically-driven secondary flows affect outer-layer similarity of turbulent length scales. *Flow Turbul. Combust.*

Yuan, J. and Piomelli, U. (2014). Roughness effects on the reynolds stress budgets in near-wall turbulence. *J. Fluid Mech*, 760:R1.